Exploring the influence of land use on the urban carbonyl sulfide budget: a case study of the Metropolitan Area of Barcelona

Carme Estruch[1], Sauveur Belviso[2], Alba Badia[3], Veronica Vidal[1], Roger Curcoll[4], Mireia Udina[5], Claudia Grossi[6], Josep-Anton Morguí[7], Ricard Segura[1], Sergi Ventura[1], Yolanda Sola[5], and Gara Villalba[1]

[1]Universitat Autònoma de Barcelona
[2]LSCE
[3]Institut de Ciència i Tecnologia Ambientals
[4]Universitat Politècnica de Catalunya
[5]University of Barcelona
[6]Instituto Catalàn de Ciencias del Clima
[7]Climate Research Laboratory, Science Park in Barcelona

July 8, 2023

Abstract

Carbonyl sulfide (OCS) is used to quantify the carbon capture potential of the biosphere because of its direct correlation with CO2 uptake during photosynthesis. However, to constrain the urban biosphere signal, it is necessary to evaluate potential anthropogenic sources. We conducted two sampling campaigns in the Metropolitan Area of Barcelona (AMB), Spain, during May (full COVID lockdown) and October 2020 to measure the spatial distribution and variability of OCS in four urban land uses as follows: built, urban forest, urban park, and peri-urban agriculture. The OCS background levels determined at Tibidabo (442 m asl) were approximately 484 ±20 ppt and 407 ±8 ppt for May and October 2020, respectively, and agreed with other seasonal surveys conducted in Europe during that same period. The urban values ranged from neutral to above background, suggesting nearby anthropogenic and marine emissions such as +D150 ppt in Montjuic, which is downwind of Barcelona's harbor. During the crop-growing season in May, the agricultural areas consistently showed values below the background (uptake) at 7:00 UTC when the land breezes were dominant, while later in the morning, when the sea breeze are developed, the plant sink is masked by the transport of marine emissions. Urban forests located north of Tibidabo showed OCS values up to -D70 ppt, suggesting significant uptake by urban forests. We conclude that determining the urban biosphere signal using OCS as a tracer is more complex than expected because the marine and anthropogenic emissions from the port strongly impact the spatial-temporal distribution of OCS.

Hosted file

966463_0_art_file_11119066_rwp664.docx available at https://authorea.com/users/633078/articles/651651-exploring-the-influence-of-land-use-on-the-urban-carbonyl-sulfide-budget-a-case-study-of-the-metropolitan-area-of-barcelona

AJE®

Editing Certificate

This document certifies that the manuscript

Exploring the influence of land use on the urban carbonyl sulfide budget: the case study of the Metropolitan Area of Barcelona

prepared by the authors

Carme Estruch, Sauveur Belviso, Alba Badia, Veronica Vidal, Roger Curcoll, Mireia Udina, Claudia Grossi, Josep-Anton Morguí, Ricard Segura, Sergi Ventura, Yolanda Sola, Gara Villalba

was edited for proper English language, grammar, punctuation, spelling, and overall style by one or more of the highly qualified native English speaking editors at AJE.

This certificate was issued on **June 12, 2023** and may be verified on the AJE website using the verification code **B4AE-F8A0-3AB2-0740-46C0** .

Neither the research content nor the authors' intentions were altered in any way during the editing process. Documents receiving this certification should be English-ready for publication; however, the author has the ability to accept or reject our suggestions and changes. To verify the final AJE edited version, please visit our verification page at aje.com/certificate. If you have any questions or concerns about this edited document, please contact AJE at support@aje.com.

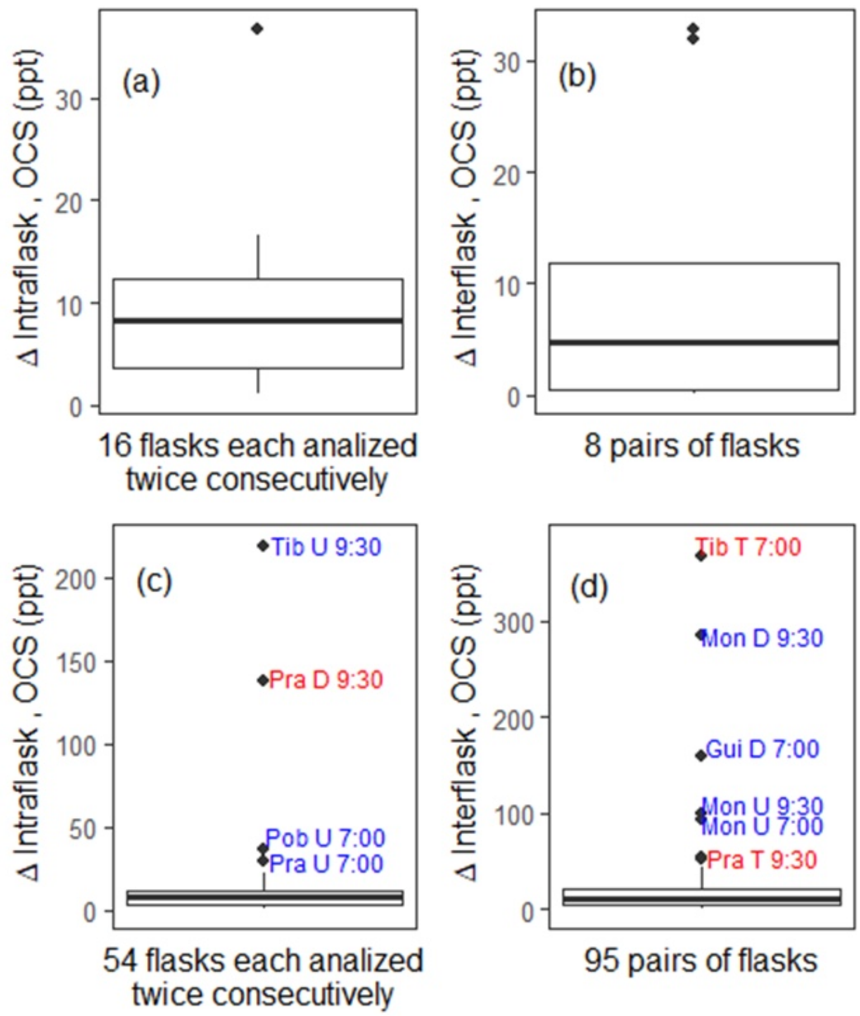
(a)
Δ Intraflask , OCS (ppt)
0
10
20
30
16 flasks each analized twice consecutively
(b)
Δ Interflask , OCS (ppt)
0
10
20
30
8 pairs of flasks
(c)
Δ Intraflask , OCS (ppt)
0
50
100
150
200
Tib U 9:30
Pra D 9:30
Pob U 7:00
Pra U 7:00
54 flasks each analized twice consecutively
(d)
Δ Interflask , OCS (ppt)
0
100
200
300
Tib T 7:00
Mon D 9:30
Gui D 7:00
Mon U 9:30
Mon U 7:00
Pra T 9:30
95 pairs of flasks

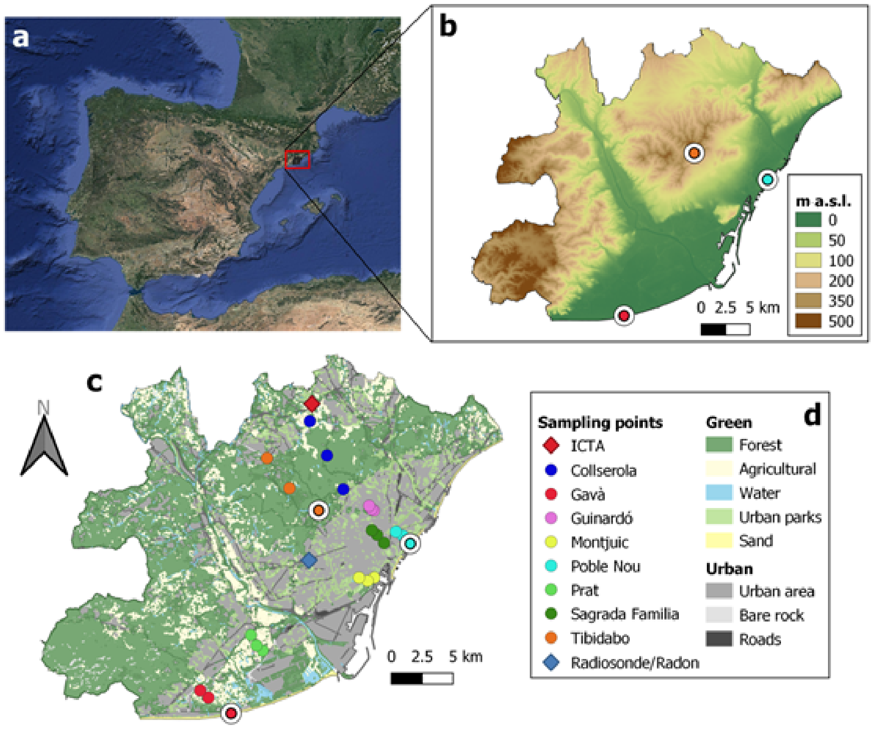
a
b
m a.s.l.
0
50
100
200
350
500
0 2.5 5 km
c
N
0 2.5 5 km
d
Sampling points
ICTA
Collserola
Gavà
Guinardó
Montjuic
Poble Nou
Prat
Sagrada Familia
Tibidabo
Radiosonde/Radon
Green
Forest
Agricultural
Water
Urban parks
Sand
Urban
Urban area
Bare rock
Roads

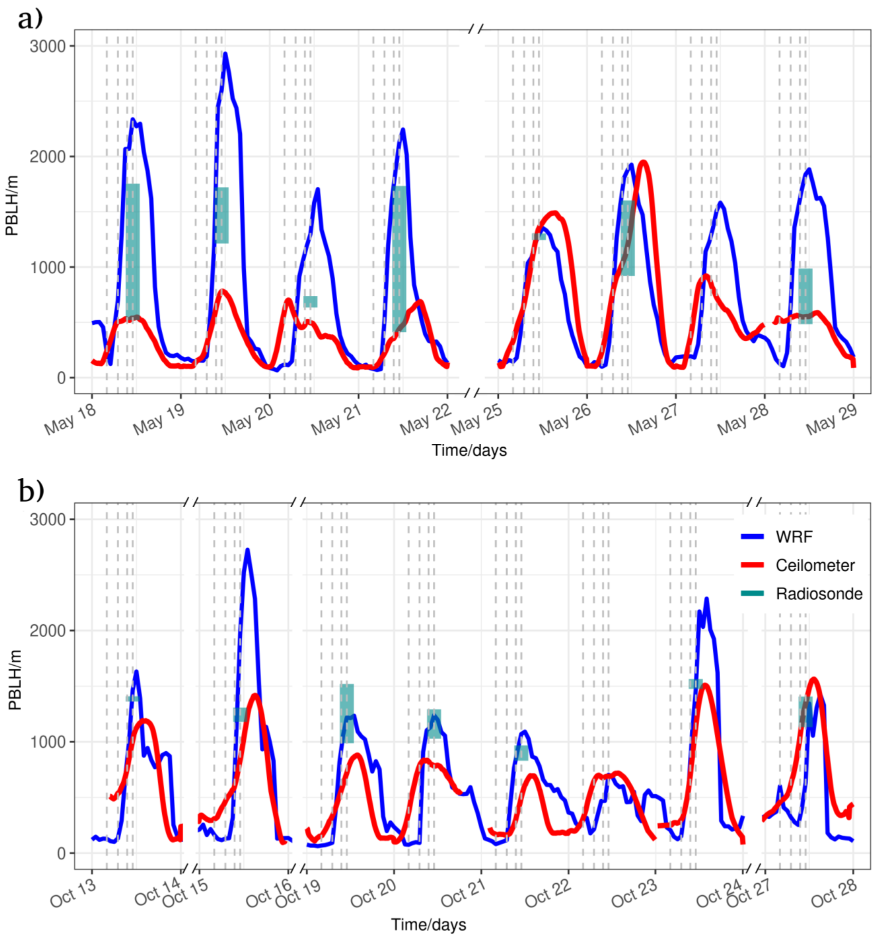

a)
b)
PBLH/m
Time/days
0
1000
2000
3000
May 18
May 19
May 20
May 21
May 22
May 25
May 26
May 27
May 28
May 29
Oct 13
Oct 14
Oct 15
Oct 16
Oct 19
Oct 20
Oct 21
Oct 22
Oct 23
Oct 24
Oct 27
Oct 28
WRF
Ceilometer
Radiosonde

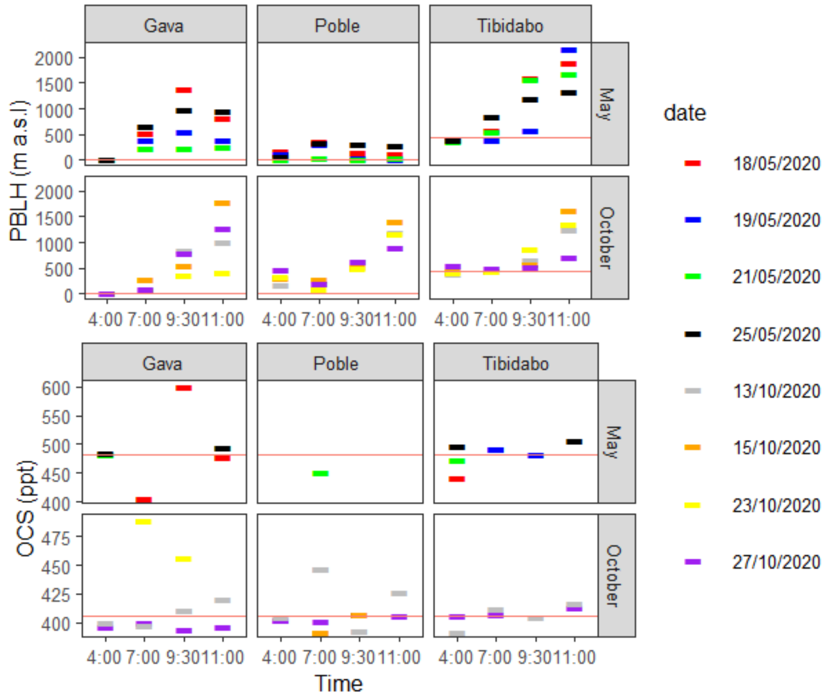
Gava
Poble
Tibidabo
May
October
PBLH (m a.s.l)
OCS (ppt)
Time
4:00 7:00 9:30 11:00
date
18/05/2020
19/05/2020
21/05/2020
25/05/2020
13/10/2020
15/10/2020
23/10/2020
27/10/2020

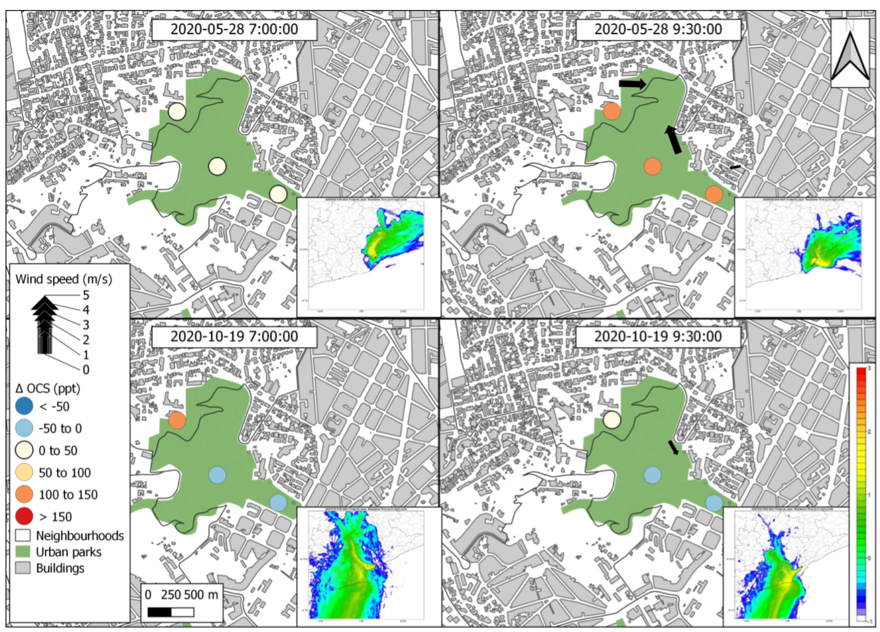
2020-05-28 7:00:00
2020-05-28 9:30:00
2020-10-19 7:00:00
2020-10-19 9:30:00
Wind speed (m/s)
Δ OCS (ppt)
< -50
-50 to 0
0 to 50
50 to 100
100 to 150
> 150
Neighbourhoods
Urban parks
Buildings
0 250 500 m

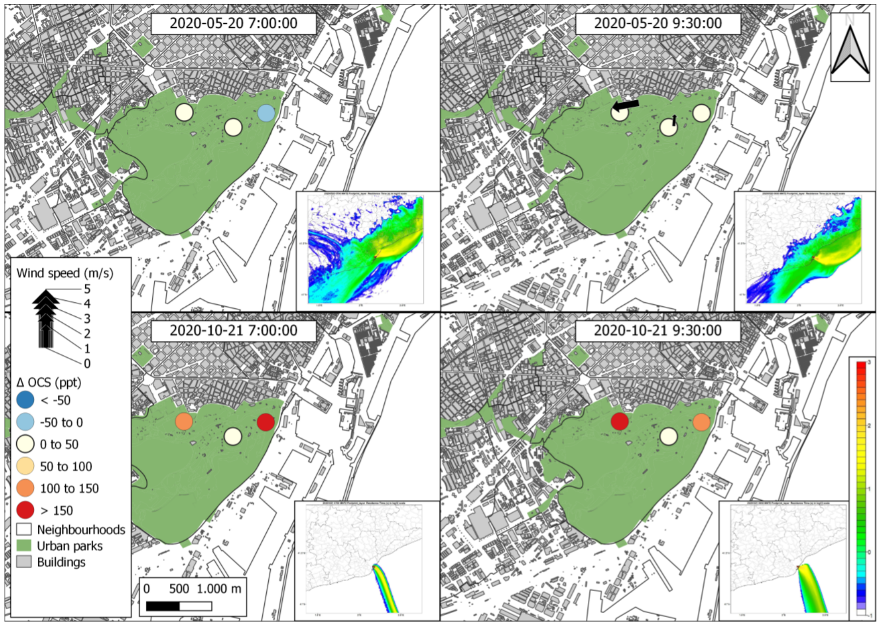
2020-05-20 7:00:00
2020-05-20 9:30:00
2020-10-21 7:00:00
2020-10-21 9:30:00
Wind speed (m/s)
5
4
3
2
1
0
Δ OCS (ppt)
< -50
-50 to 0
0 to 50
50 to 100
100 to 150
> 150
Neighbourhoods
Urban parks
Buildings
0 500 1.000 m

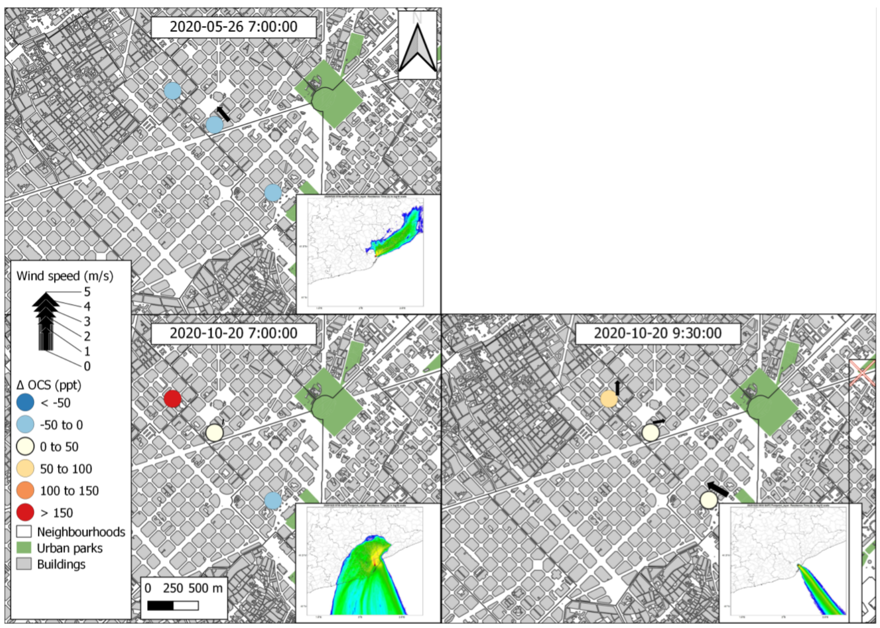
2020-05-26 7:00:00
2020-10-20 7:00:00
2020-10-20 9:30:00
Wind speed (m/s)
5
4
3
2
1
0
Δ OCS (ppt)
< -50
-50 to 0
0 to 50
50 to 100
100 to 150
> 150
Neighbourhoods
Urban parks
Buildings
0 250 500 m

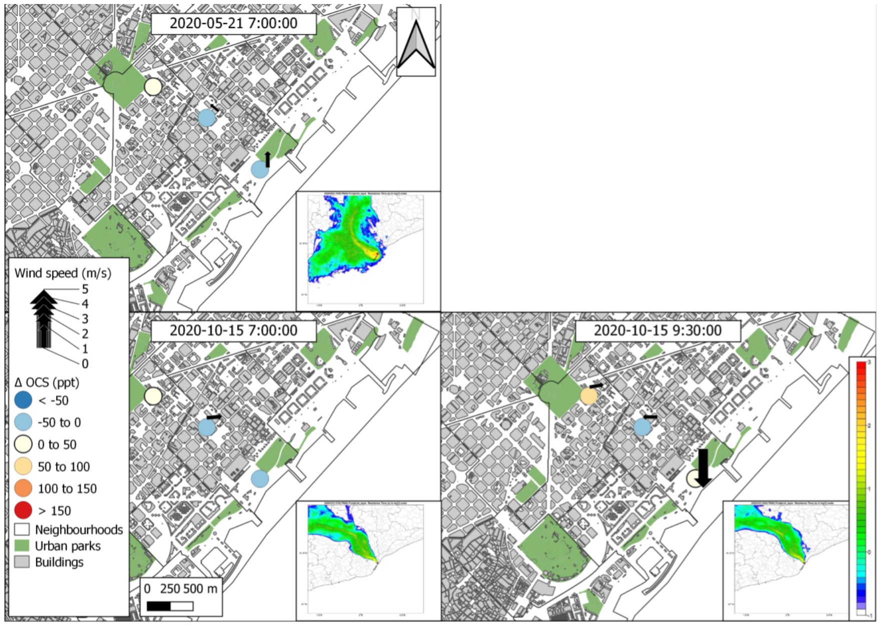
2020-05-21 7:00:00
2020-10-15 7:00:00
2020-10-15 9:30:00
Wind speed (m/s)
5
4
3
2
1
0
Δ OCS (ppt)
< -50
-50 to 0
0 to 50
50 to 100
100 to 150
> 150
Neighbourhoods
Urban parks
Buildings
0 250 500 m

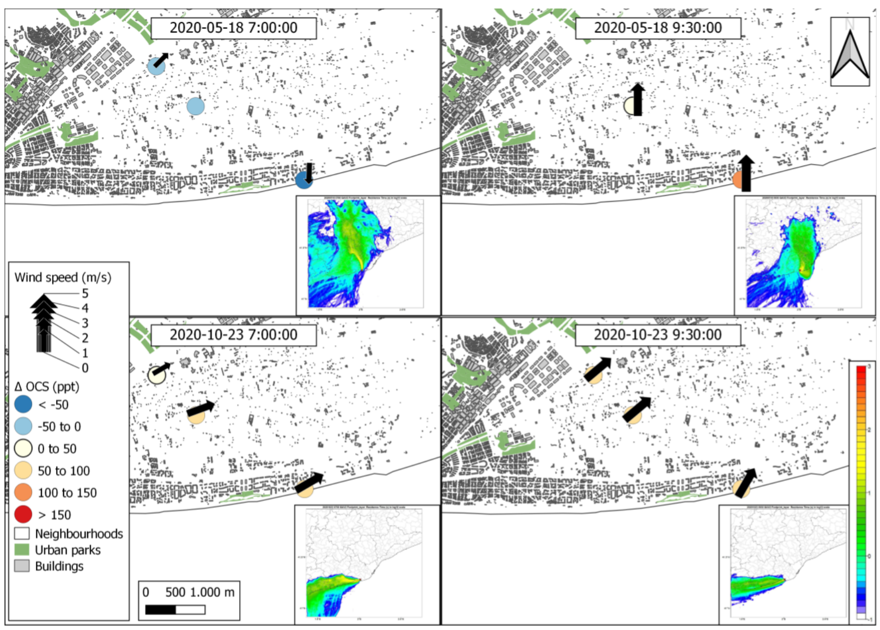
2020-05-18 7:00:00
2020-05-18 9:30:00
2020-10-23 7:00:00
2020-10-23 9:30:00
Wind speed (m/s)
5
4
3
2
1
0
Δ OCS (ppt)
< -50
-50 to 0
0 to 50
50 to 100
100 to 150
> 150
Neighbourhoods
Urban parks
Buildings
0 500 1.000 m

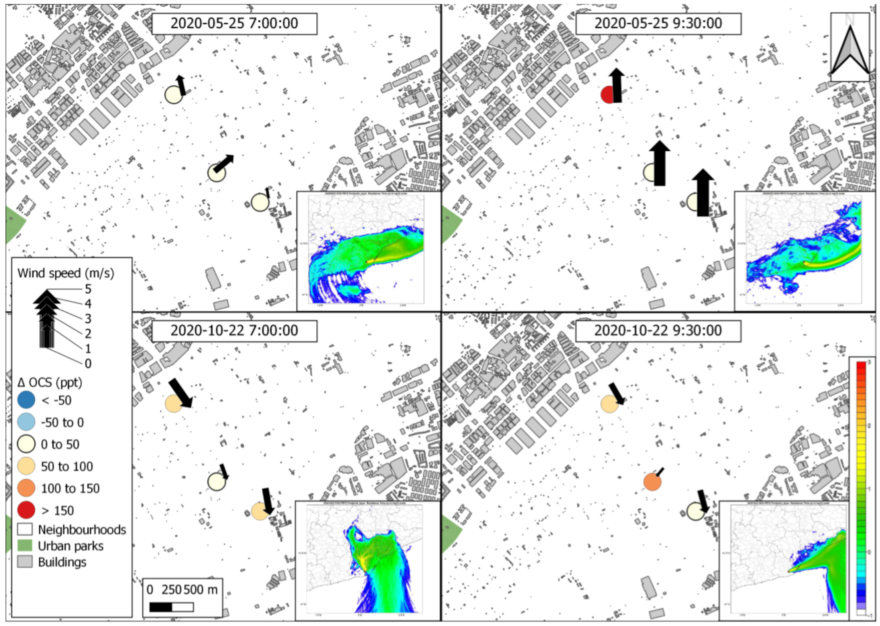

2020-05-25 7:00:00
2020-05-25 9:30:00
2020-10-22 7:00:00
2020-10-22 9:30:00
Wind speed (m/s)
5
4
3
2
1
0
Δ OCS (ppt)
< -50
-50 to 0
0 to 50
50 to 100
100 to 150
> 150
Neighbourhoods
Urban parks
Buildings
0 250 500 m

Exploring the influence of land use on the urban carbonyl sulfide budget: a case study of the Metropolitan Area of Barcelona

Carme Estruch[1,2], Sauveur Belviso[3], Alba Badia[1], Veronica Vidal[1,4], Roger Curcoll[1,5], Mireia Udina[6], Claudia Grossi[5], Josep-Anton Morguí[1,7], Ricard Segura[1], Sergi Ventura[1], Yolanda Sola[6], Gara Villalba[1,8]*.

[1]Institut de Ciència i Tecnologia Ambientals (ICTA), Universitat Autònoma de Barcelona, 08193 Cerdanyola del Vallès, Barcelona, Spain.

[2] Eurecat, Centre Tecnològic de Catalunya, Climate Change Research Department, Amposta, Spain.

[3]Laboratoire des Sciences du Climat et de l'Environnement, LSCE, Paris-Saclay, France.

[4]Department of Computer Architecture and Operative Systems, Universitat Autònoma de Barcelona (UAB), Spain.

[5]Institute of Energy Techniques, Universitat Politècnica de Catalunya, Av. Diagonal 647, 08028, Barcelona, Spain.

[6]Departament de Física Aplicada–Meteorologia, Universitat de Barcelona, Barcelona, Spain.

[7]Departament de Biologia Evolutiva, Ecologia i Ciències Ambientals, Universitat de Barcelona, Barcelona, Spain.

[8]Department of Chemical, Biological and Environmental Engineering, Universitat Autònoma de Barcelona (UAB), Spain.

Abstract

Carbonyl sulfide (OCS) is used to quantify the carbon capture potential of the biosphere because of its direct correlation with CO_2 uptake during photosynthesis. However, to constrain the urban biosphere signal, it is necessary to evaluate potential anthropogenic sources. We conducted two sampling campaigns in the Metropolitan Area of Barcelona (AMB), Spain, during May (full COVID lockdown) and October 2020 to measure the spatial distribution and variability of OCS in four urban land uses as follows: built, urban forest, urban park, and peri-urban agriculture. The OCS background levels determined at Tibidabo (442 m asl) were approximately 484 ±20 ppt and 407 ±8 ppt for May and October 2020, respectively, and agreed with other seasonal surveys conducted in Europe during that same period. The urban values ranged from neutral to above background, suggesting nearby anthropogenic and marine emissions such as $+\Delta 150$ ppt in Montjuic, which is downwind of Barcelona's harbor. During the crop-growing season in May, the agricultural areas consistently showed values below the background (uptake) at 7:00 UTC when the land breezes were dominant, while later in the morning, when the sea breeze are developed, the plant sink is masked by the transport of marine emissions. Urban forests located north of Tibidabo showed OCS values up to $-\Delta 70$ ppt, suggesting significant uptake by urban forests. We conclude that determining the urban biosphere signal using OCS as a tracer is more complex than expected because the marine and anthropogenic emissions from the port strongly impact the spatial-temporal distribution of OCS.

Introduction

Carbonyl sulfide (hereafter OCS) is an atmospheric trace gas used to study the CO_2 sequestration capacity of vegetation (Remaud et al., 2023 and references therein; Whelan et al., 2018 and references therein) because it is destroyed through photosynthesis in the same way as CO_2 without producing any emissions through respiration (Protoschill-Krebs and Kesselmeier, 1992). According to the latest estimations, terrestrial vegetation and soils takes up from 530 and 670 Gg S yr^{-1} (Remaud et al., 2023 and references therein) the largest natural sink of atmospheric OCS. Surface oceans are the most important natural source of OCS contributing directly and indirectly, i.e., from the atmospheric oxidation of carbon disulfide and dimethylsulfide, between 270 and 320 (Remaud et al., 2023 and references therein). The global budget of OCS is partially balanced by anthropogenic emissions, which are estimated to be 400 Gg S yr^{-1} (Remaud et al., 2023 and references therein). Terrestrial sinks and natural and anthropogenic sources are generally separated in space and time, and exhibit distinct seasonal and spatial variations (Remaud et al., 2023). Hence, land use changes are expected to have a significant influence on the global budget of atmospheric OCS.

Although many studies have evaluated OCS budgets at regional and global scales, little is known about OCS sources and sinks at the urban scale. Understanding land use influence on the budget of atmospheric OCS at the urban scale is much more difficult to establish because sources and sinks can coexist over small distances. For example, Commane et al. (2013) indirectly assessed OCS sources along the highly urbanized coastline of California where they detected biogenic OCS emissions from wetlands in Sacramento Bay, anthropogenic emissions near a storage facility and refinery in the port of Los Angeles, and OCS loss during the daytime due to photosynthetic uptake in vegetated areas. Besis et al. (2021) also conducted a study that identified potential sources of OCS at the city level and observed the spatial heterogeneity influencing OCS mixing ratios of Thessaloniki, Greece, and identified three locations where OCS concentrations in inner-city areas were three times higher than those at the seafront and where the waste management system was a source of OCS. According to Zumkehr et al. (2018), anthropogenic emissions of OCS due to aluminum, residential and industrial coal, TiO_2, solvents and tires in the Metropolitan Area of Barcelona contribute to 65% (178 Mg S yr^{-1}) of the total emissions in the Catalonia region (276 Mg S yr^{-1}, see Fig. S1 in supporting information). However, a study by Belviso et al. (2023) demonstrated that the Zumkehr et al. (2018) inventory for France largely overestimated OCS anthropogenic emissions by approximately an order of magnitude. A previous study by the same group used direct measurements from a sampling tower and computed back trajectories with the FLEXPART transport model to find that the Paris suburban area was acting mainly as an OCS sink (Belviso et al., 2022). Another urban study of Innsbruck, Austria, measured the hourly exchange rates of OCS with an eddy covariance tower and showed that urban OCS emissions are significantly higher at noon during weekdays than during weekends, which suggests that road traffic could be a net source of OCS emissions.

The use of OCS as a photosynthesis tracer has recently received attention as a potential method to determine the contribution of the urban biosphere toward reducing the carbon footprint (Mallik et al., 2016; Villalba et al., 2021). Mallik et al. (2016) reported the first records of annual OCS mixing ratios over an Indian city, which were substantially higher than tropospheric values, and those values changed seasonally with an observed 86% drop in OCS in November when air masses changed from oceanic to continental. Villalba et al. (2021) also observed changes in OCS related to air masses coming from marine and continental sources. This work highlighted the difficulty of characterizing the biosphere signal when the input masses are continental due to the heterogeneity they present in OCS content compared to stable marine conditions.

This study aims to contribute to the understanding of the dynamics of OCS budgets in urban areas by exploring to what extent different urban land uses can have an impact on atmospheric OCS mixing ratios in terms of the particular urban climate, geography, and topography affecting the transport and mixing of OCS sources and sinks. Motivated by the present lack of in situ OCS continuous measurements to properly infer surface OCS (Remaud et al., 2022), we conducted an OCS measurement campaign in the Metropolitan Area of Barcelona (AMB). We selected four different land uses as sampling sites as follows: forest, agricultural land, urban parks and impervious areas with the intention of understanding the role of urban land use on the OCS budget in a coastal city where we would expect a mixing ratio gradient between the sea (where OCS is produced) and the land (OCS capture in vegetated areas). The selection of sampling areas was based on their potential as a sink of OCS based on photosynthetic rates (Campbell et al., 2017; Villalba et al., 2021; Yang et al., 2018) or a local source based on anthropogenic inventories (Lee and Brimblecombe, 2016; Yan et al., 2019; Zumkehr et al., 2018). The OCS sampling campaigns were funded and conducted within the project *Integrated System Analysis of Urban Vegetation and Agriculture* (URBAG), which was financed by the European Research Council with the overall aim of understanding the influence of green infrastructures on the urban CO_2 budget. As a coastal city with intense sea breezes during the day, the AMB is an ideal case study to determine the contribution of the urban biosphere and other anthropogenic sources to the overall urban OCS budget. The campaigns were conducted during the spring and early autumn of 2020 and almost coincided with the OCS spring maximum and autumn minimum (Montzka et al., 2007). Furthermore, the May campaign took place during the full lockdown due to the COVID pandemic, which helped constrain the biosphere signal given the reduction in anthropogenic activities that are potential sources of OCS such as vehicle exhaust (Zumkehr et al., 2017). We analyzed the observed OCS concentrations in terms of land-use influence while understanding the role of local weather conditions, synoptic events, and the planetary boundary layer by using atmospheric transport models, climate observations and atmospheric tracers. More specifically, we attempted to answer the following specific questions: how significant is the variability of OCS mixing ratios in an urban ecosystem? What is the land-use influence on the urban OCS budget?

1. Methods

2.1. Study site

The two experimental campaigns took place in the Metropolitan Area of Barcelona (AMB), located in the NE corner of Spain, as shown in Fig. 1. The AMB, with a total surface area of approximately 640 km^2 and over 3.3 million inhabitants (16,160 people/km^2), is the 7th largest urban area and 8th most densely populated region in the European Union. It is also one of the most industrialized areas in the western EU (Querol et al., 2004), specializing in food production, chemicals, vehicle manufacturing, and gas production and distribution (Institut d'Estadística de Catalunya, 2023). The AMB is bounded by the Besós River in the northeast, the Llobregat River in the west, the Collserola mountain range to the north, and the Mediterranean Sea to the south, as shown in Fig. 1. The AMB has a Mediterranean dry subhumid climate with an annual precipitation of approximately 600 mm, which is mainly concentrated during spring and autumn, and a mean annual temperature of 16.5 °C. The orography of the city extends from sea level to 516 m above sea level (a.s.l.) at the mountain range located northwest of the main urban areas.

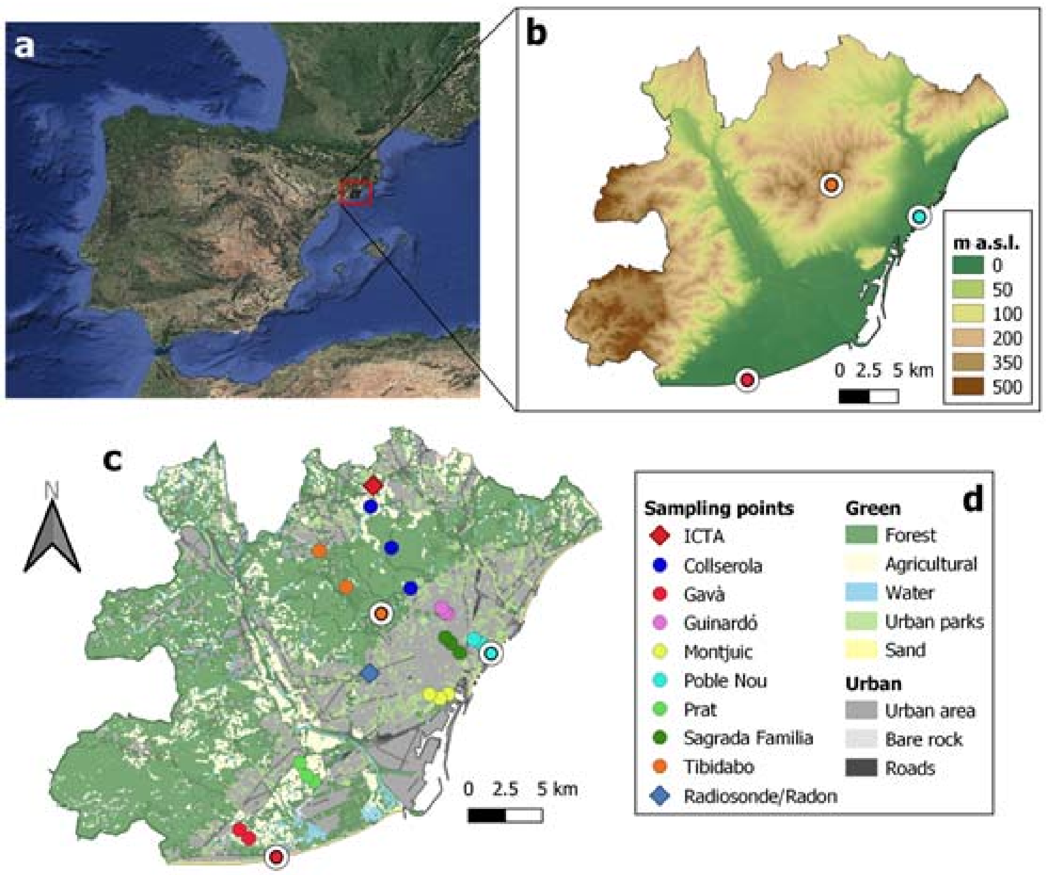

Fig. 1. (a) A map of Spain showing the Metropolitan Area of Barcelona (AMB, red rectangle). Orography of the AMB (b) and land use (c), where triplicates of colored dots represent the upwind, target, and downwind sampling locations (d). Background atmospheric OCS levels were investigated at the upwind sampling points at the sites of Tibidabo (highest altitude in the PBL), Gavà and Poble Nou (closest to the shore). These sites are depicted with colored dots with white circles in b and c. The red diamond represents the location of ICTA and the blue one where the radiosondes were launched and the radon measurements were performed (c).

More than half of the AMB's surface area is covered by vegetation in various forms, including urban forest (43%), agricultural fields (8%) and urban parks (4%), while 41% is covered by impervious and other infrastructures (4%). Land uses are shaped by the following physical constraints: crops are located in the coastal plains formed by the delta of the Llobregat River, while urban forests composed of pine and holm oaks are located in the Collserola mountain range (Fig. 1). Urban green spaces are scattered throughout the metropolis and populated with ornamental species ranging from acacias to plantain trees and ornamental shrubs and grasses.

2.2. Field campaigns

Air samples were taken at the eight sites shown with colored dots in Fig. 1c, which were selected to represent the heterogeneity of land use throughout the AMB and are summarized into four land-use categories (see table 1): agricultural area (located in the Gavà and Prat areas), urban forest (Tibidabo and Collserola), urban green (Montjuic and Guinardó) and urban (Sagrada Familia and Poble Nou). We took air samples at each site (hereafter referred to as the target site) and upwind and downwind of each target site in an attempt to follow the air mass flow during its trajectory over the target site. The upwind and downwind sampling sites were determined based on historical wind patterns and trajectories typical of each target location under similar atmospheric conditions expected during the campaign and are available from the Meteorological Service of Catalonia (www.meteo.cat) and shown in Appendix S1 of the supporting information. Note that in May and October 2020, observed wind patterns sometimes differed from historical data. The locations of the upwind, target, and downwind sites are shown for each point using the same color in Fig. 1c. The spatial distance among the three sampling points of each site ranges from 500 to 4,000 meters. Sampling times were chosen to capture inland winds during the early morning (i.e., 4:00 and 7:00 UTC am) and the typical sea breezes that develop during the morning and early afternoon (i.e., 9:30 and 11:00 UTC am).

The first campaign took place between May 18th and May 28^{th,} 2020, which was during a period of intense transport restrictions due to the COVID-19 pandemic, and resulted in highly significant air pollution reductions (Badia et al., 2021). Anthropogenic emissions drastically decreased, especially for the aviation (95%), road transport (up to 85%), and more moderately according to shipping (21%), public power %) and industry (11%) sectors (Guevara et al., 2021). The second campaign took place from the 13th to the 27th of October 2020, when the anthropogenic activity returned to normal.

The temperature ranged from 20 °C to 24 °C during May and 14 °C to 20 °C during October. Samples were collected at 7:00 UTC and 9:30 UTC, and for some specific days, we performed additional sampling at 4:00 UTC and 11:00 UTC for the Tibidabo, Gavà and Poble Nou upwind locations to determine the background concentration of OCS. The weather was stable during both campaigns with one day of slight precipitation during each sampling campaign, which accumulated 2.6 and 1.6 mm during May 29 and October 26, respectively. The air mass influence was mostly cyclonic and advective with some days characterized by anticyclonic circulation. Synoptic winds were mostly north and east during the May campaign and predominantly southwest during October as summarized in Table S2 of the supporting information.

We recorded temperature, air pressure, wind direction and wind speed at each sampling site using a portable anemometer (Skywatch Xplorer 4). The relative humidity was obtained from the Meteorological Service of Catalonia for the first campaign (Servei Meteorològic de Catalunya, 2023), and additionally, it was registered on site using a digital hygrometer (TFA Dostmann®, precision ±4%) during the October campaign.

1.3. OCS measurements and analysis

Samples were collected in cylindrical borosilicate glass flasks (1 L volume, Normag Labor und Prozesstechnik GmbH, Germany) with Kel-F PCTFE valves fitted at both ends. This flask material showed the lowest permeation of gases compared to other sealing materials (Sturm et al., 2004). To ensure the quality of the measurement technique and repeatability of the experiment, two flasks connected to each other in a portable device were simultaneously filled in series (see Appendix S2, Urban sites, for device pictures). The inlet was installed at 3.5 m above ground level (m a.g.l.) and air, after passing through a magnesium perchlorate desiccant tube to remove moisture and a filter to remove particles, was pumped to the flasks with the help of a diaphragm pump (KNF N84.4 ANDC). Before taking the sample, air was flushed through the flasks for at least 10 min. At that time, we checked that the flow was steady and between 2.0 L min^{-1} and 3.5 L min^{-1}. After flushing, the exit valve was closed, and the flasks were pressurized with sample air to approximately 1.5 bar. Samples from the target, upwind and downwind sites were taken at the exact same moment to simulate an Eulerian approximation in which the sampling point remains fixed (Leelőssy et al., 2016).

Flasks were sent to the Laboratoire des Sciences du Climat et de l'Environnement, LSCE, Paris-Saclay, France, for OCS analyses. Flasks were stored for a maximum of 2 months before analysis. OCS was analyzed following the analytical method described in Belviso et al. (2016) and Belviso et al. (2022). In this procedure, atmospheric OCS (500 ml) is trapped using an automated sampling system (Entech P7100 preconcentrator) and then analyzed by gas chromatography with pulsed flame photometry detection (PFPD, Varian Model 3800, Belviso et al., 2016). Calibration was performed every week using a calibration gas supplied by Air Products (Belviso et al., 2016). The difference between the assigned value of an NOAA long-term air standard (NOAA-2004 scale) and the average of multiple analyses of that same standard was smaller than 1.5%. The drift between calibrations was assessed on a daily basis using a short-term target gas (Belviso et al., 2016).

1.4. Determining the planetary boundary layer height

It is necessary to determine the planetary boundary layer height (PBLH) to understand its influence on the accumulation and dilution of OCS concentration at each site over the urban area. PBLH measurements were not possible at the eight target sites, but at least the PBLH was calculated from measurements taken on the campus of the University of Barcelona (Fig. 1, label: Radiosonde/Radon) using two different techniques as follows: (1) based on observed measurements from a radiosonde (RSD) station installed on the roof of the Physics Department of the University of Barcelona (41°23’03’’ N 2°07’01’’E), which is part of the Global Meteorological Network (GCOS, 2016); and (2) via a laser ceilometer (CL-31, Vaisala Inc., Finland) located at the same place with a measurement range up to 7.6 km, 10-m vertical resolution and a temporal resolution of 16 s. For the latter, the PBLH is estimated from the ceilometer data using the Vaisala Boundary-Layer View software (BL-VIEW) Enhanced Gradient method (VAISALA, 2020) – see details in Garcia-Dalmau et al. (2021) - followed by selection algorithms according to the methodology of Lotteraner et al. (2016).

To determine the PBLH based on radiosonde measurements, we followed a robust numerical procedure proposed by Liu and Liang (2010) using midday radiosonde (RSD) observations from the selected periods of study and considering 1100 UTC as the launching time. The PBLH was computed following the air parcel method for a convective dominated boundary layer (Holzworth, 1964; Seibert et al., 2000; Stull, 1988) as the height where air parcel evolution following a dry adiabatic evolution from surface intersects with the environment temperature profile. The calculated PBLH from RSD was visually corrected to solve the method errors and mostly related to the presence of several temperature inversion layers. A detailed explanation of the method and how we applied it to our case study is presented in the supplementary material (Appendix S3).

In this study, we also analyzed radon, which is a radioactive and noble gas known to be a good atmospheric tracer (Grossi et al., 2012), to better understand the evolution of the PBLH and to corroborate the PBLH calculated from the ceilometer observations using the method proposed by Griffits et al. (2013). Hourly atmospheric concentrations of Rn were measured during October 2020 using an Atmospheric Radon MONitor (ARMON) at the Barcelona School of Industrial Engineering station (41°23’03’’ N 2°07’01’’E, 10 m a.g.l) at the same site that radiosonde and ceilometer data were recorded and identified with the label Radiosonde/Radon in Fig. 1c. The monitoring was designed and built by the Universitat Politècnica de Catalunya as described by Grossi et al. (2012). Due to COVID-19 restrictions, no radon data were recorded for May 2020 because the equipment had to be shut down.

The estimations of PBLH using radiosonde and ceilometer were also compared with PBLH simulated using the Weather Research and Forecasting model (WRF). WRF simulations were performed to obtain information on the main transport processes and the vertical mixing conditions throughout the AMB as described in Section 2.6.

1.5. WRF simulations of the urban atmosphere

The WRF v4.3 model (Skamarock et al., 2021) coupled with the multilayer urban canopy scheme BEP-BEM (Salamanca et al., 2010) was used in this study to simulate the urban atmosphere over the AMB to better understand the influence of local weather conditions and PBL development on OCS concentrations. The WRF configuration used for this study consists of 3 two-way nested domains with horizontal resolutions of 9 km, 3 km, and 1 km covering the Iberian Peninsula, the Catalan territory, and the AMB, respectively, with 45 vertical layers up to 100 hPa (see Fig. S2 in Supporting information). The physics parameterization for the planetary boundary layer is the Boulac scheme, which has been shown to be the most suitable to resolve the turbulence intensity in convective situations for the AMB (Segura et al., 2021). We included 11 urban local climate zone (LCZ) classifications (Stewart and Oke, 2012) for the innermost domain and each had a specific value for thermal, radiative and geometric parameters of the buildings and ground, which are used by the BEP-BEM to compute the heat and momentum fluxes in urban areas (Gilabert et al., 2021; Ribeiro et al., 2021; Yu and Steinberger, 2011). We conducted simulations for May and October 2020 using meteorological initial and boundary conditions from ERA5 (Copernicus, 2023). Table S3 in the supporting information further describes the model characteristics and experimental configurations. The model simulations were validated using temperature, wind speed and wind direction observations from 14 meteorological stations of the Meteocat network (https://www.meteo.cat/observacions/xema).

1.6. FLEXPART back trajectories

FLEXPART back trajectories were calculated to determine the precedence of air sampled at the various sites to establish whether the air mass influence was local or regional. FLEXPART (FLEXible PARTicle dispersion model) is a Lagrangian transport and dispersion model that is used for calculating the long-range and mesoscale dispersion of air pollutants (Stohl et al., 2005). The FLEXPART version adapted to the WRF mesoscale model (Brioude et al., 2013) was used to calculate back trajectories of air tracers from each of the sampling sites at the sampling times. The back trajectories were computed from the output of the WRF model at the nested domain of 1 km with 16 vertical levels from 0 to 2000 m a.g.l. Each back trajectory was calculated for 24 h after the sampling time. The number of particles released to the atmosphere in the simulation was 2000. From the 3D back trajectories, only the layers from 0 to 100 meters above ground level were used for the study of footprints, as it is where the exchange among the land/ocean - atmosphere takes place.

2. Results

3.1. OCS sample repeatability and accuracy in urban environments

We performed a precision analysis of the GC measurements of flask-air samples according to the methods developed by Belviso et al. (2022) to assess the repeatability and accuracy of the OCS measurements in an urban environment. Eight pairs of flasks in total were selected randomly from the May and October campaigns, and each flask was analyzed twice consecutively for OCS. The average difference between duplicated measurements, i.e., the intraflask difference, was 9.8 ± 8.7 ppt (median = 8.2 ppt, interquartile range (IQR) = 3.6–12.7 ppt, n = 16, 90^{th} percentile = 16.5 ppt, 6.3% of outliers), as shown in Fig. 2a. It was slightly higher than that reported by Belviso for samples collected in a rural area over wheat and rapeseed crops (Belviso et al. (2022), i.e., 9.3 ± 7.2 ppt (median = 7.5 ppt, interquartile range (IQR) = 4.5–12.5 ppt, n = 58, 5.2% of outliers, but in that case, the 90^{th} percentile was 19.5 ppt). Fig. 2c shows that among the 54 flasks (each analyzed twice consecutively), four displayed mixing ratios higher than the 90^{th} percentile (i.e., 22.9 ppt), while the median and IQR of the intraflask difference (7.7 ppt and 3.3-12.1 ppt, respectively) appear to be highly consistent with the data displayed in Fig. 2a. Consistency is also found in terms of the proportion of aberrant determinations of OCS mixing ratios (i.e., 6.3% (Fig. 2a) and 7.4% (Fig. 2c)). It was concluded that the precision for GC measurements of flask-air samples remained unchanged over the two campaigns and was consistent with that reported by Belviso et al. (2022).

The average difference between flasks of the same pair (i.e., the interflask difference) was also analyzed in a duplicate manner and was 10.1 ± 14.0 ppt (median = 4.8 ppt, IQR = 0.05–18.6 ppt, n = 8, no outlier, Fig. 2b). Hence, the interflask difference during the AMB study displayed higher variability than that of Belviso et al. (2022), i.e., 5.5 ± 4.5 ppt (median = 4.9 ppt, IQR = 2.2–8.0 ppt, n = 29, a 6.9% proportion of outliers was reported in that study). The interflask difference was also assessed from a single analysis of the content of each flask. The median, IQR and 90^{th} percentile were 12.1 ppt, 4.3-22.5 ppt and 45.0 ppt, respectively, with n= 95 (Fig. 2d). We reported the existence of six outliers (i.e., a proportion of 6.3%) exhibiting interflask differences higher than 45.0 ppt and up to 360 ppt. The interflask difference calculated from pairs of flasks each analyzed only once for OCS (Fig. 2d) displays higher variability than that from pairs of flasks analyzed twice consecutively (Fig. 2b).

Consequently, although the four outliers displayed in Fig. 2c should have been discarded, we arbitrarily reincorporated those exhibiting intraflask differences in the range of 22.9 ppt (i.e., the 90th percentile) and 36.8 ppt. According to Belviso et al. (2022), data from pairs of flasks exhibiting interflask differences higher than 14 ppt should be discarded. Note that this threshold is approximately twice that set by Montzka et al. (2007). Although the interflask difference calculated from pairs of flasks each analyzed only once for OCS could originate from aberrant data (Fig. 2d), nobody ever documented the high frequency distribution of OCS mixing ratios next to potential urban sources of that gas. In other words, although flasks are supposed to be simultaneously filled in pairs, the process of pressurization of two flasks connected in series could generate concentration gradients reflecting the heterogeneous distribution of OCS next to potential urban sources of that gas. In light of this possibility, we decided to arbitrarily validate the six outliers reported in Fig. 2d and investigate whether interflask differences higher than 45 ppt would be site dependent or would result from aberrant data.

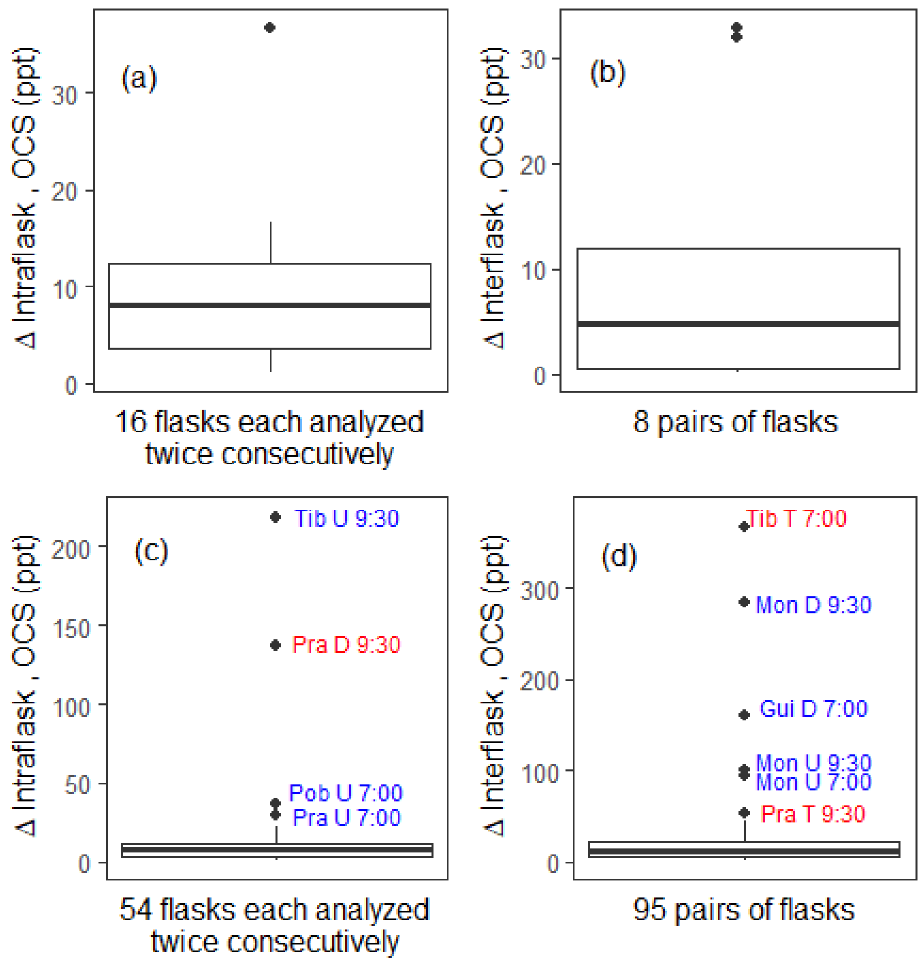

Fig. 2. Analysis precision for OCS measurements from flask-air samples collected in the AMB showing the 10th, 25th, median, 75th and 90th percentiles. (a, c) show Δ interflask differences in OCS concentration between two consecutive analyses of the content of each flask (median of flask 1 minus that of flask 2), whereas (b, d) show the Δ interflask differences in OCS concentration between flasks of the same pair. The diamonds correspond to the outliers (> 90th percentile), which are over 23 ppt in Fig. 2c and over 45 ppt in Fig. 2d. Outliers are labeled according to the location and time of sample collection. The codes of each sampling site are site, location and time UTC (sites: Tib: Tibidabo, Pra: Prat, Pob: Poble Nou, Mon: Montjuic, Gui: Guinardó; location: U: Upwind, D: Donwind, T: Target). Note that historical wind data was used for that purpose. The label colors represent the campaigns and correspond to red for May and blue for October.

3.2. Evaluation of WRF simulations

We ran WRF BEP-BEM simulations in May 2020 and October 2020 to obtain high-resolution meteorological data, atmospheric stability, and PBLH during the sampling periods. Statistical analyses of the root-mean-square error (RMSE), mean bias (MB) and correlation factor (R) were used to evaluate performances of the model compared with ground-based meteorological observations from Meteocat (see Section 2.6). The near-surface relative humidity (RH), temperature (T) and wind speed (WS) statistical analyses are displayed in Figs. S3 and S4 for campaigns in May and October, respectively. There is an overall good performance for the modeled RH, T and WS in comparison with the observations with an average error of ±14% for RH, ±1.7 to 1.9 °C for T and ±1.65 ms-1 for WS. This statistical analysis is available in the supporting information in Table S4.

During the May campaign, there were predominant northerly winds from the north from the 18^{th} until the 21^{st}, and the circulation weather types were hybrid-cyclonic to cyclonic regimes, while the second half (25^{th} through the 28^{th}) was characterized by winds from the east with a Mediterranean Sea air mass influence and adventive regimes, with the exception of the 28^{th}, which was anticyclonic with a southeast synoptic wind component and local maritime air mass influence. During the October campaign, westerly and southerly winds characterized by adventive circulation weather types prevailed for most of the period with a cyclonic north influence and regional continental air mass in the first two days switching to a maritime influence for the rest of the campaign. Table 1 summarizes these weather patterns for each day of the two campaigns.

Table 1. Circulation weather type (CWT), synoptic wind component (SWC) and PBLH extracted from WRF simulations expressed in meters above ground level (a.g.l), averaged OCS concentrations of all measurements taken each day during the May and October campaigns, and expressed in ppt (mean values from the 3 sites, mean values ± standard deviations). An unabridged version of this table with upwind and downwind OCS including a detailed data for background measurements concentrations (see figure 4) is available in S1 of the supporting information.

Campaign	**Site (elevation)**	**Land use type**	**Date**	**CWTs***	**SWC****	**PBLH range (m)**	**OCS 7:00 UTC (ppt)**	**OCS 9:30 UTC (ppt)**
May 2020	Tibidabo (175-442 m)	Forest	19/05	C	N	19-441	478±20	494±9
	Gavà (0-2 m)	Agricultural	21/05	U	N	11-249	482.1±NA	495.5±10.7
	Poble Nou (0-4 m)	Urban	21/05	U	N	44-2217	461±20	NA
	Montjuic (42-98 m)	Urban green	20/05	C	N	327-883	485±14	490±5
	Prat (0-2 m)	Agricultural	25/05	E	E	737-1182	502±NA	508±2
	Sagrada (37-55 m)	Urban	26/05	E	E	771-1900	460±6	NA
	Collserola (107-442 m)	Forest	27/05	E	E	395-1079	441±39	497±3
	Guinardó (115-169 m)	Urban green	28/05	A	SE	590-1524	505±8	612±17
October 2020	Gavà (0-2 m)	Agricultural	23/10	U	NW	21-5019	401±9	403±3
	Poble Nou (0-4 m)	Urban	15/10	CN	N	287-571	405±23	426±45
	Guinardó (115-169 m)	Urban green	19/10	ASW	SW	69-934	389±20	392±16
	Sagrada (37-55 m)	Urban	20/10	SW	SW	29-1085	444±19	460±93
	Montjuic (42-98 m)	Urban green	21/10	CSW	SW	92-734	425±NA	485±87
	Prat (0-2 m)	Agricultural	22/10	SW	SW	103-495	468±24	490±37

***CWT:** Circulation weather type. The different types of CWTs are cyclonic (C), anticyclonic (A), pure advective (N, S, E, W, NE, SE, NW, SW), hybrid cyclone-advective (CN, CNE, CE, CSE, CS, CSW, CW, CNW), hybrid anticyclone-advective (AN, ANE, AE, ASE, AS, ASW, AW, ANW), and undefined (U). ****SWC:** Synoptic wind component summarizing the pressure pattern, fronts, wind direction and speed.

3.3 Planetary boundary layer height calculations and evaluation

The PBLH from the WRF BEP-BEM simulations was compared against ceilometer estimations and radiosonde observations at 11:00 UTC for each day of the campaigns (see Fig. 3). All data time series follow the expected PBLH diurnal pattern with a rapid growth of the PBLH during the morning, a maximum that was reached at midday, and a decrease during the afternoon. The PBLH calculated by the WRF model is generally higher than that estimated by the ceilometer and radiosonde. During the first period of May and first days of October when there are continental regional air masses with prevailing large-scale northern winds, we noticed an important difference between the ceilometer, radiosonde, and WRF values in some cases up to 150 m difference at 11 UTC. In this situation, the large-scale winds dominate the boundary-layer scales, which limit the capacity of the WRF model to estimate the PBLH and leads to high uncertainty in the radiosonde observations (Stull, 1988).The inverse correlation between atmospheric radon concentrations and the ceilometer-based PBLH is uniformly maintained during the entire October campaign as you can see in Fig. S5 how PBLH are at is maximum at 00:00 UTC while atmospheric radon concentration are at its lowest, and the opposite behavior is seen around 12:UTC (see Fig. S5and Fig. S6 of the supporting information), which further indicates an overestimation of the PBLH by WRF during strong wind events in early October. The highest radon activity concentrations (between 0.01 Bq m^{-3} and 0.05 Bq m^{-3}) are observed during nighttime (21 h-2 h) when the PBLH reaches its minimum, whereas the lowest values (between 1 Bq m^{-3} and 2 Bqm^{-3}) are observed during diurnal hours (11 h-16 h) when ^{222}Rn is diluted due to a well-developed PBL.

The overestimated PBLH modeled values in May are consistent with an overprediction of the 2 m temperature seen for a station located 1.2 km from the radiosonde launching location. In contrast, better agreement between the modeled and observed PBLH (both radiosonde and ceilometer) is seen during the second half of the May campaign from the 25th to 28th of May (Fig. 3a), when the easterly winds lead to a more stable atmosphere. October showed better agreement overall among the PBLH values obtained from the ceilometer, RSD and WRF model due to higher atmospheric stability. The south-easterly weak winds generally lead to stable conditions and local scale dominance where the PBLH can be well estimated.

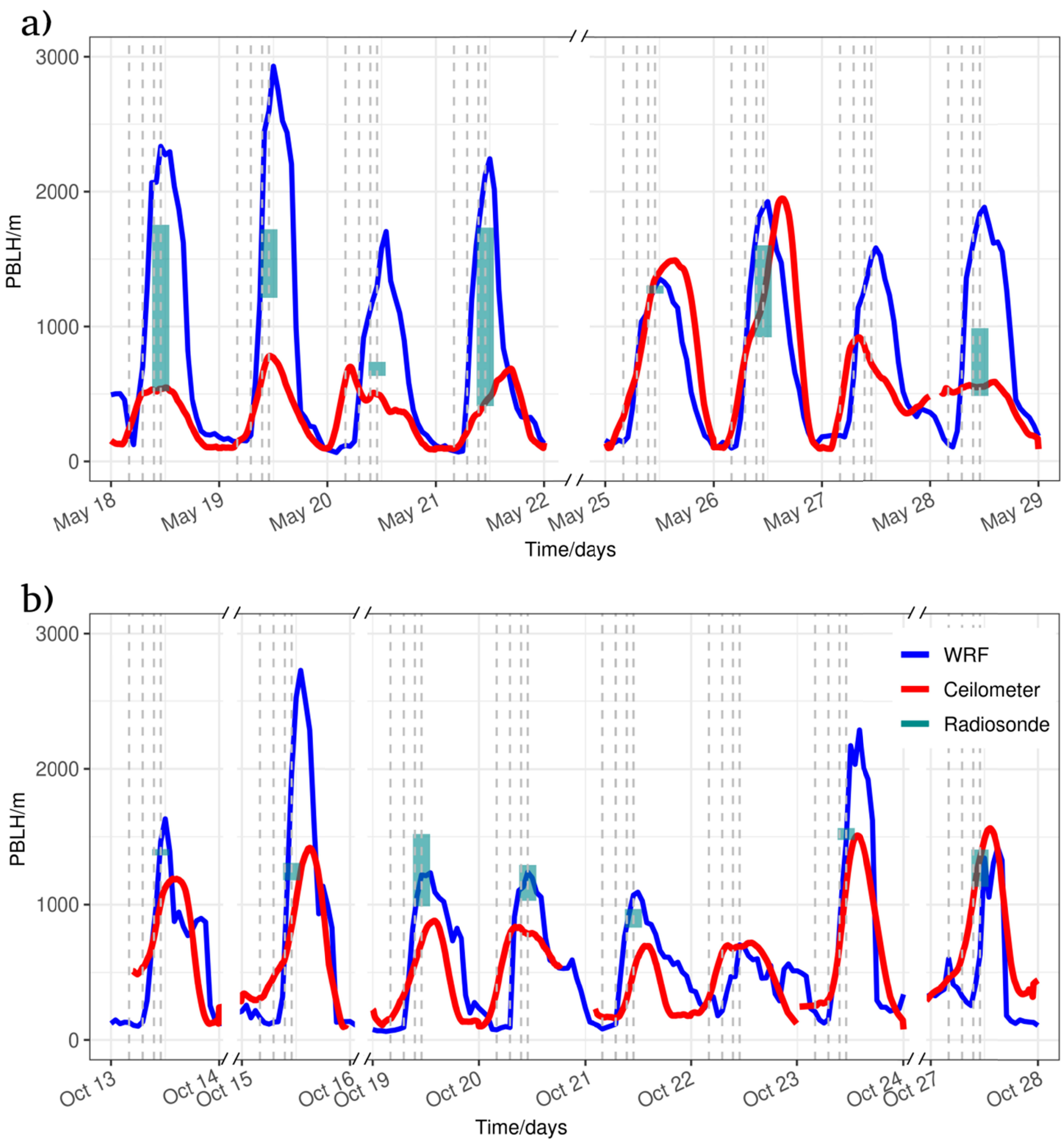

Fig. 3 The time series of modeled PBLH (blue line) together with the Ceilometer (red line) and the Radiosonde (blue shade) for a) May and b) October campaigns. Shaded blue areas indicate the PBLH using two different definitions for its calculation. Vertical lines correspond to the 4 am, 7 am, 9:30 am and 11 am UTC sampling times on a daily basis.

3.4 WRF-FLEXPART footprints

FLEXPART simulations showed that the sampling campaign covered different synoptic situations and different air mass origins. Appendix S4 of the supporting information shows that during the May campaign, two main directions were observed as follows: one coming from the northwest following the Llobregat River basin (days 18, 19, and 21 of May) and another from the northeast with more sea influence (days 20 and 25 of May) and some others with more land influence (such as days 26, 27, and 28 of May). Generally, the simulation at 09:30 UTC shows more sea origin of the air masses arriving at sampling points than the simulations at 07:00 UTC in accordance with the sea–land breeze regimes.

During the October campaign, the air masses mainly came from the northwest following the Llobregat River basin (days 15, 19, and 27 of October), although a situation with strong winds coming from the south was observed between the 20th and 21st of October. A stronger breeze regime is observed during this month with general changes in the origin of air masses between the simulations at 07:00 and 09:30 UTC.

3.5. Background OCS measurement validation

There were three potential background measurement locations (upwind sites of Gavà, Poble Nou and Tibidabo shown in Fig. 1), but only Tibidabo at 442 m a.sl showed stability in OCS concentrations regardless of the diurnal convection patterns (Fig. 4a), which ranged from 443 to 507 ppt during May and 392 to 416 ppt during October, as shown in Fig. 4b. The coastal sites showed less stable values with Gavà showing the highest variability ranging from 407 to 600 ppt during May and 393 to 489 ppt in October, which are values well above the global background level. For example, on May 18th, a great variability in OCS mixing ratios was observed, and FLEXPART back trajectories simulated for Gavà showed significant changes in air mass precedence (see Appendix S4a: Gavà, May 18, 2020, at 7:00, 9:00, and 11:00 UTC). At 7:00 UTC, we obtained the lowest OCS concentration value of the campaign (407 ppt) when air masses came from the inland north and collected air from forested areas; a few hours later at 9:30 UTC, the concentration rose to 600 ppt because air transport switched to an influence from the northeast where the densest part of the AMB is located. Earlier and later that day, at 4:00 and 11:00 UTC, OCS measurements were closer to typical background values, which indicated the marine influence of sea breezes during those hours, which decreased residential times over the urban area. Thus, we established Tibidabo mean values as a background measurement with a mean value for OCS of 484 ppt in May and 407 ppt during October. Our Tibidabo background values show congruence with those of the National Oceanic and Atmospheric Administration (NOAA), which ranged from 478 to 498 ppt in May and 399 to 408 ppt in October (https://gml.noaa.gov/hats/gases/OCS.html).

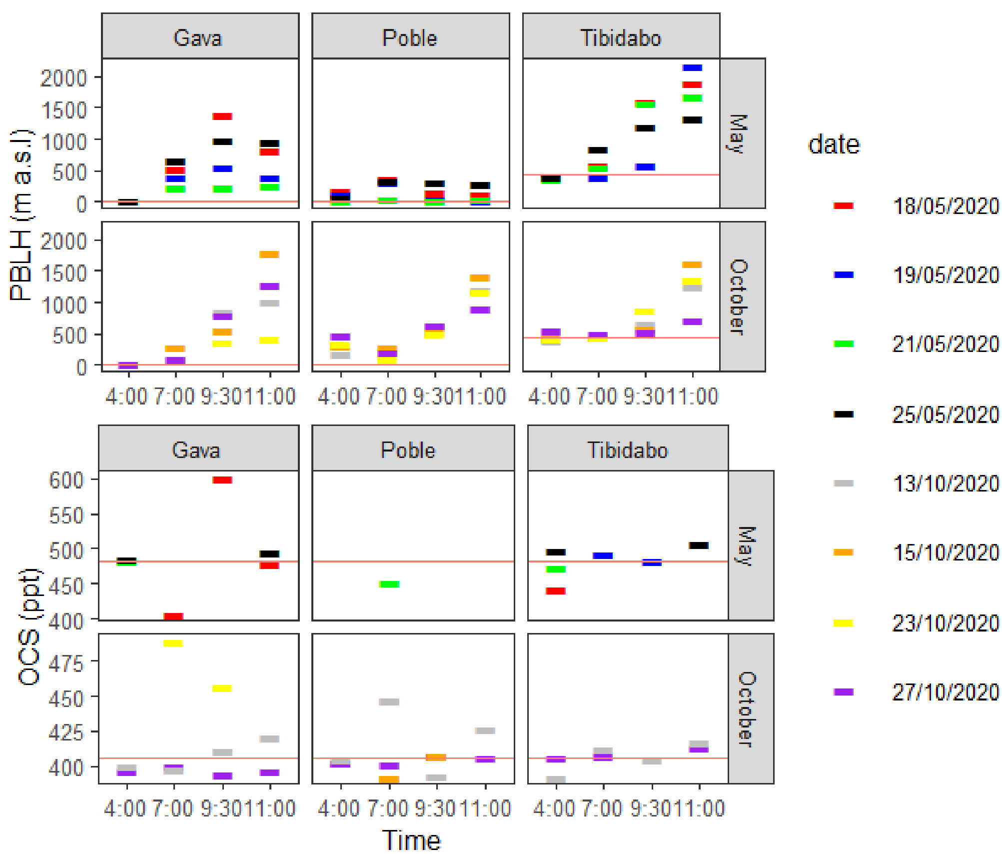

Fig. 4. (a) PBLH from the WRF model of three potential background site measurements for the AMB. The red line represents the current altitude for each site. (b) OCS concentrations of three potential background measurements for the AMB. The red line represents the background value chosen, which corresponds to the Tibidabo site with mixing ratios of 484 and 407 ppt for the May and October campaigns, respectively. Detailed data for background measurements concentrations is available in S1 of the supporting information.

Generally, OCS background concentrations were higher in May (484 ppt) than in October (407 ppt), which reflects the global annual oscillation of maximum values in spring (mean north hemisphere 510 ppt for May) and lowest values in the fall (mean north hemisphere 440 ppt for October) reported by Montzka et al. (2007) for northern hemisphere Atlantic locations.

3.6. OCS concentrations over the metropolitan landscape

The OCS concentrations at each site for both campaigns are given in Table 1, which also provides the circulation weather type (CWT), the synoptic wind component (SW) and PBLH from the WRF model simulations. The full data set is available at the Zenodo repository (URBAG, 2023) as well as the supporting information table S1. The highest concentrations were recorded in May at the sampling sites of Guinardó and El Prat (612±17 ppt and 508±2 ppt) when winds were coming from the east, independently if mass air influence was local or regional, and well above ocean background values of 478 to 498 ppt estimated at the North Atlantic locations by NOAA (Fig. S7, https://gml.noaa.gov/hats/gases/OCS.html). High-pressure, anticyclonic conditions during that time suggest that the high OCS concentration values might be due to the accumulation of local OCS emissions.

The lowest OCS concentrations were recorded at Gavà and Collserola in May (407.1±8.5 and 412.6±13.8 ppt, respectively) and at Gavà, Guinardó, Sagrada Familia and Poble Nou in October (398.3±6.1, 374.1±8.6, 397.3±5.2, and 390.4±15.7, respectively). There seems to be no clear pattern relating circulation weather typologies to OCS measurements. For example, the highest OCS mixing ratio during the October campaign was recorded in Montjuic at 7:00 UTC (485±87 ppt) with hybrid cyclone-advective conditions that influenced the day and regional air mass with wind blowing from the southwest (Table 1). In October, we had a similar weather pattern, yet this location registered one of the lowest OCS concentrations (389±20 ppt). However, Sagrada Familia also recorded the second lowest value (392±16 ppt) in October with maritime stable conditions on both days. For May, the lower record corresponds to Gavà at 7:00 UTC (431±22 ppt), which was a day with local continental atmospheric conditions.

4. Discussion

4.1. Exploring the land-use influence on the OCS budget of the urban area.

We found more variability among the OCS mixing ratios within the metropolitan area than between the two campaigns, which ranged from 450 to 600 ppt for May and from 390 to 470 ppt for October. This indicates that local sources and sinks, the heterogeneity of the urban landscape, and local air transport in the AMB have a larger weight on the OCS urban budget than what other stations that monitor more homogenous areas, such as Gif-Sur-Yvette and Mace head, than within cities such as Utrecht (Fig. S7). We proceeded to analyze how each type of land use had an influence on OCS concentrations, considering other measured or modeled variables such as air transport regimes, PBLH development, and air mass influence.

Urban parks: Samples were measured from two urban parks located in very different urban environments in the AMB (see Fig. 1 for their locations and supporting information and Appendix S2 for pictures). Guinardó Park is located in the middle of Barcelona in one of the most densely populated areas, which is characterized by a high built fraction and surrounded by streets with heavy traffic. At 169 m a.s.l and a total area of 15.9 ha, Guinardó has dedicated spaces for recreational purposes and a wide number of ornamental trees including acacias, magnolias and other foreign species. However, Montjuic Park is close to the sea and overlooks the Port of Barcelona at 98 m a.s.l. with a total area of 227 ha. It is part of a highly vegetated recreational area on Montjuic Mountain with more than 690 species of identified plants including palm trees, acacias, pines, and a great variety of shrubby plants.

Guinardó was sampled on May 28TH at 7:00 and 9:30 UTC with little presence of local winds at that time. Fig. 5a shows the OCS enhancements (Δ OCS) calculated as the measured OCS concentration at each site minus the background concentration of 484 ppt established for the month of May (Table S1 in supporting information can be consulted for absolute values). Initially, at 7:00 UTC, OCS concentrations at downwind, target, and upwind, were +22, +28, and +11 ppt, respectively over the established background level of 484 for May showing little enhancement; however, at 9:30 UTC, we observed a significant ΔOCS of +110, +128, +144 ppt, respectively. FLEXPART backward trajectories for these times (embedded in Fig. 5a and b, while a larger Fig. is provided in Appendix S4) estimate that the forthcoming air masses were mostly local with breezes changing from land (north–east) at 7:00 to sea (southeast) at 09:30 UTC. This suggests local sources of OCS from both the sea and industrial activity of the port. Overall, it seems that the OCS capture capacity by the vegetation of Guinardó Park is offset by significant local sources that are perceptible when wind blows from SE (Locations abected by port, city and ship traffic), which increase OCS concentrations by +140 ppt despite a highly developed PBLH of 1,524 m at 9:30 UTC, which favors mixing and lower concentrations.

Samples taken on October 19^{th} showed the opposite behavior as follows: ΔOCS were -33, -4, and +113 ppt for the downwind, target, and upwind directions, respectively, at 7:00 and -15, -32, +2, ppt, respectively, at 9:30 UTC, as shown in the lower panel of Fig. 5a. This time, the FLEXPART backward trajectory indicates a regional air transport influence from the northwest at 7:00 UTC, which transports air masses from the agricultural Llobregat basin. At 9:30 UTC, winds switch to southwest collecting air with influences from croplands and the sea. Furthermore, local breezes were insignificant, and the PBLH did not develop very strongly between 7:00 and 9:30 am, going from 69 to 934 meters, which leads us to believe that the lower concentrations at both 7:00 and 9:30 are most likely attributable to vegetation uptake in the park and the influence of air mass transport from agricultural fields rather than mixing of air that is typical of a fully developed boundary layer.

a) Guinardó

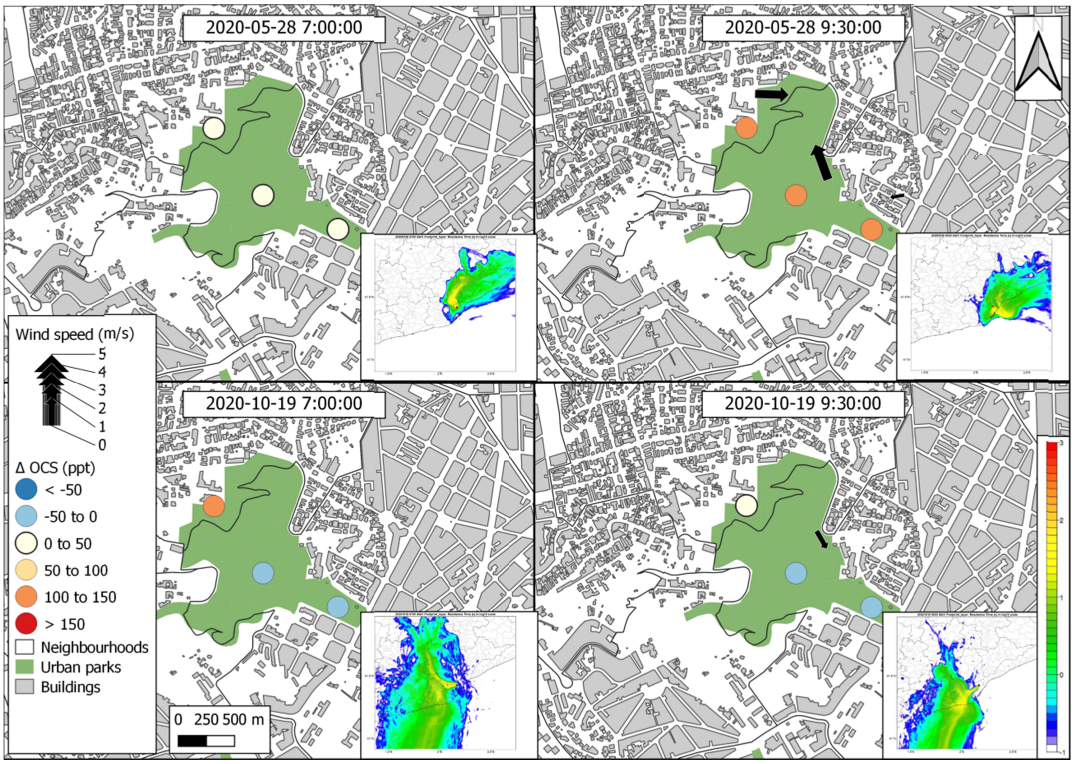

b) Montjuic

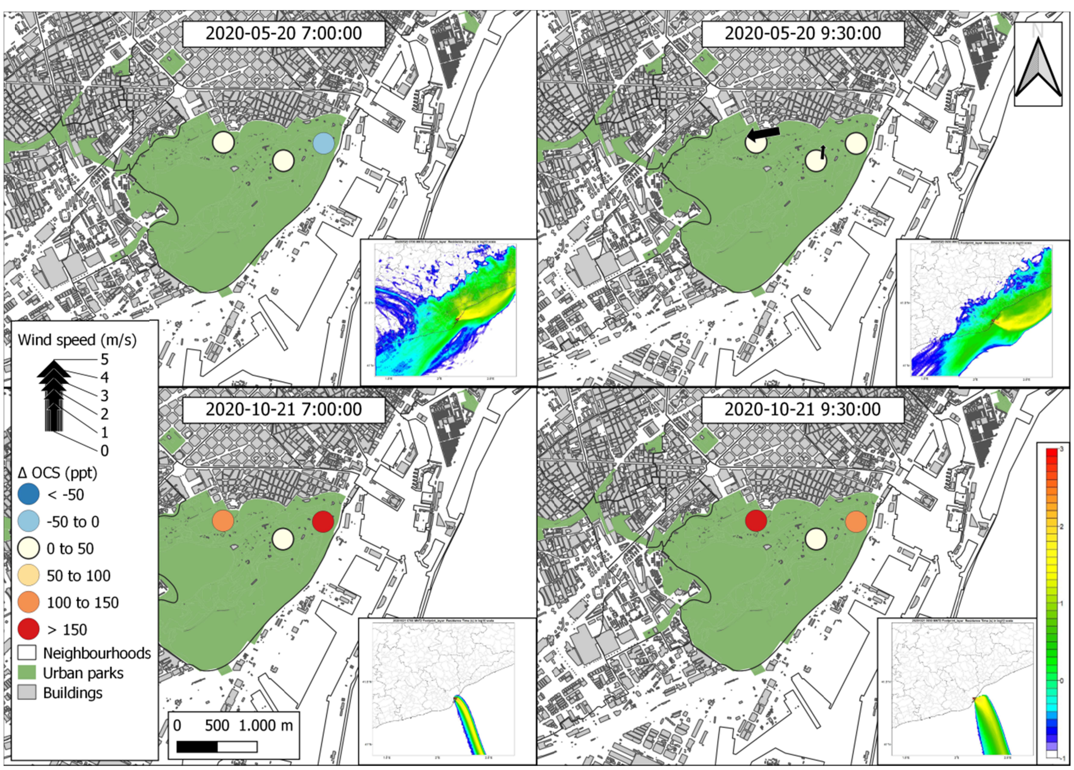

Fig. 5. OCS enhancement (Δ OCS) in ppt calculated as measured OCS minus background OCS (484 ppt for May and 407 ppt for October) for each campaign at the two urban parks as follows: a) Guinardó and b) Montjuic. The black arrow shows the wind direction and speed measured on site, and the absence of an arrow indicates that there was no wind blowing at the moment of measurement. A small map embedded in the lower right-hand corner of each panel shows the residence time on a logarithmic scale of the air masses arriving at the sampling site as determined with the FLEXPART model.

Montjuic Park offers more information in terms of the OCS drawdown capacity of the vegetation because of its key location next to the Port of Barcelona, which is expected to be a source of OCS due to its natural gas supply activity and ships. As illustrated in Fig. 5b, there was very little difference between the 7:00 and 9:30 UTC OCS enhancements during May, which ranged from -12 to +17 ppt. The FLEXPART simulation for that day indicates a regional sea influence from eastern winds at 7:00 and 9:30 UTC that explains why all sites have OCS concentrations very close to background values at both times. There seems to be no significant source of OCS over the Montjuic area since the easterly winds are not influenced by the Port of Barcelona, which lies further south.

In contrast, during the October campaign, there was a strong southern regional influence on air masses over Montjuic Park as described by the FLEXPART trajectory. The air arrived from due south with no land influence, which, in addition to a low PBLH at 9:30 UTC of 561 meters, constrains any changes in the OCS budget over Montjuic Park to very local processes. Thus, the high OCS values of 665 and 635 ppt we see at 7:00 and 9:30 UTC for the upwind site and downwind site and reaching more than +150 ppt above background, are most likely a result of the industrial activity of the Port of Barcelona. This enhancement was consistently seen in all upwind and downwind samples at 7:00 and 9:30. At the target site, samples were consistently near background values with enhancements of only +16 and +18 ppt at 7:00 and 9:30 UTC, respectively. It is more difficult to determine the reasons for this decrease compared to the other two points; it could not receive the emission plume that reached the other two places and combined with an effect of the vegetation signal. The fact that the target is at double the height of the upwind and downwind sites (98 m asl vs. 58 and 42 m asl) leads us to think that the signal from the plume with a high content of OCS did not arrive with the same intensity. The PBLH was 92 m at 7:00 UTC but 720 m at 9:30 UTC, which could only explain this difference in the early hours.

Urban forest. There were two sampling locations representing urban forests as follows: Tibidabo and Collserola. Both locations belong to the Collserolla range, which is a mountainous area with more than 8,000 ha located in the northern limit of the city with a maximum altitude of 512 m asl. The flora of the park is maritime Mediterranean and is dominated by white pine (*Pinus halepensis*) and low vegetation of maquis, scrub and meadows apart from cultivated fields. It has an estimated population of 10 billion trees and more than 1,000 species of plants. During the May campaign, OCS concentrations at 7:00 UTC ranged between 463 and 499 ppt and 412-498 ppt for Tibidao and Collserola, respectively, which are all within the range of the assigned background concentration. There was one exception at the Tibidabo Target site at 7:00, which had 620±260.2 ppt and was discarded as the outlier with the largest discrepancy between replicates (see Fig. 2). Enhancements were minimal with ΔOCS of -16, -72 and -33 ppt for collserola, +7 and -21 ppt for Tibidabo at 7:00 UTC, +9, +14 and +15 ppt for Collserola, and -2, +15 and +15 ppt for Tibidabo at 9:30 UTC. We had local and regional air mass influences and marine to continental winds for Collserola and Tibidabo (see Fig. S8 and Table 1). Local winds at/:00 UTC in Collserola suggested that the small OCS drawdown was due to the vegetation. The forest sites clearly showed a behavior from neutral to sink with respect to OCS exchange fluxes. Having established this tendency, we limited the sampling to the background location (Tibidabo upwind) during the October campaign.

Urban: OCS concentrations in May were surprisingly lower than our background estimate for both of our urban locations of Sagrada Familia and Poble Nou, which are characterized by 100% built environments of buildings, streets, constant traffic and little or no vegetation (see

Fig. 1 for their locations and supporting information and Appendix S2 for pictures). The OCS enhancements ranged between -17 to -29 ppt and 0 to -36 ppt for Sagrada Familia and Poble Nou, respectively, at 7:00 UTC, as shown in the upper panels of Fig. 6 (9:30 UTC samples were not possible because of complications with the logistics during the campaign). Given the low mixing potential of the relatively low PBLH for both the Poble Nou and Sagrada Familia (100 and 800 m, respectively), we can conclude that there were no local OCS sources. One likely reason for this is that there was little or no traffic during this time due to the COVID lockdown and mobility restrictions. The FLEXPART trajectory for Sagrada Familia shows an influence of easterly winds bringing air from the sea. However, we discarded the regional influence on OCS transport because the urban sampling locations were surrounded by buildings. Instead, we assume that local winds have a higher weight on OCS transport, and we were not able to measure any significant local winds.

a) Sagrada Familia

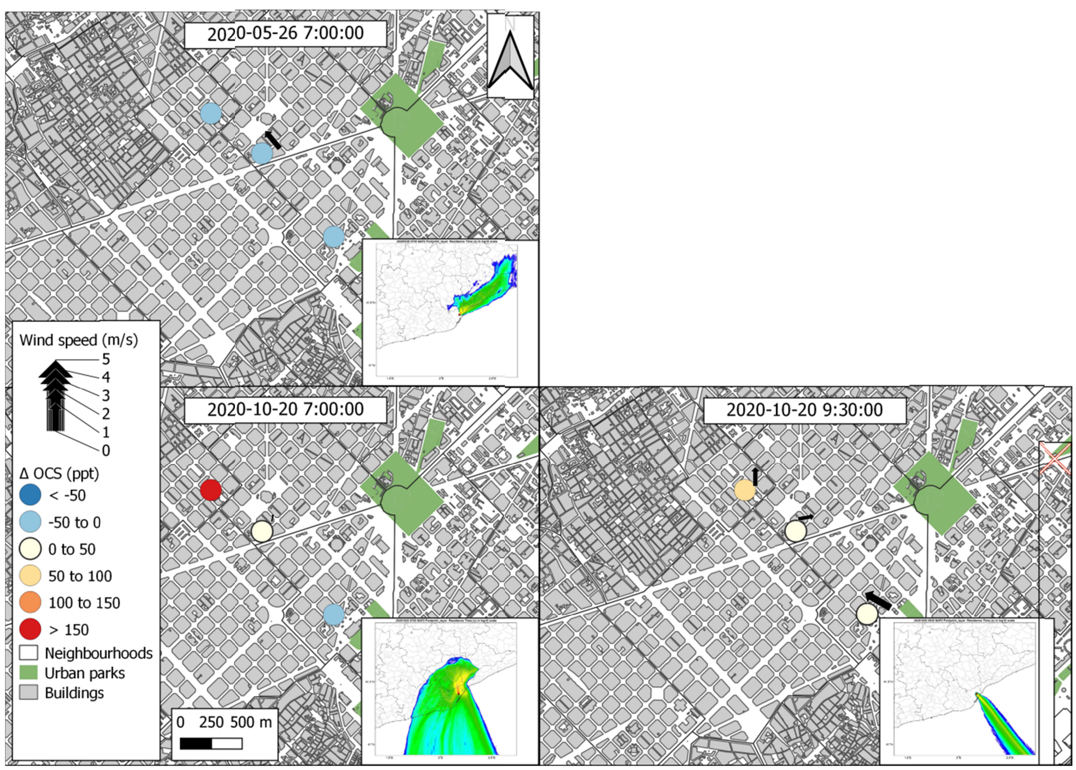

b)

c) B) Poble Nou

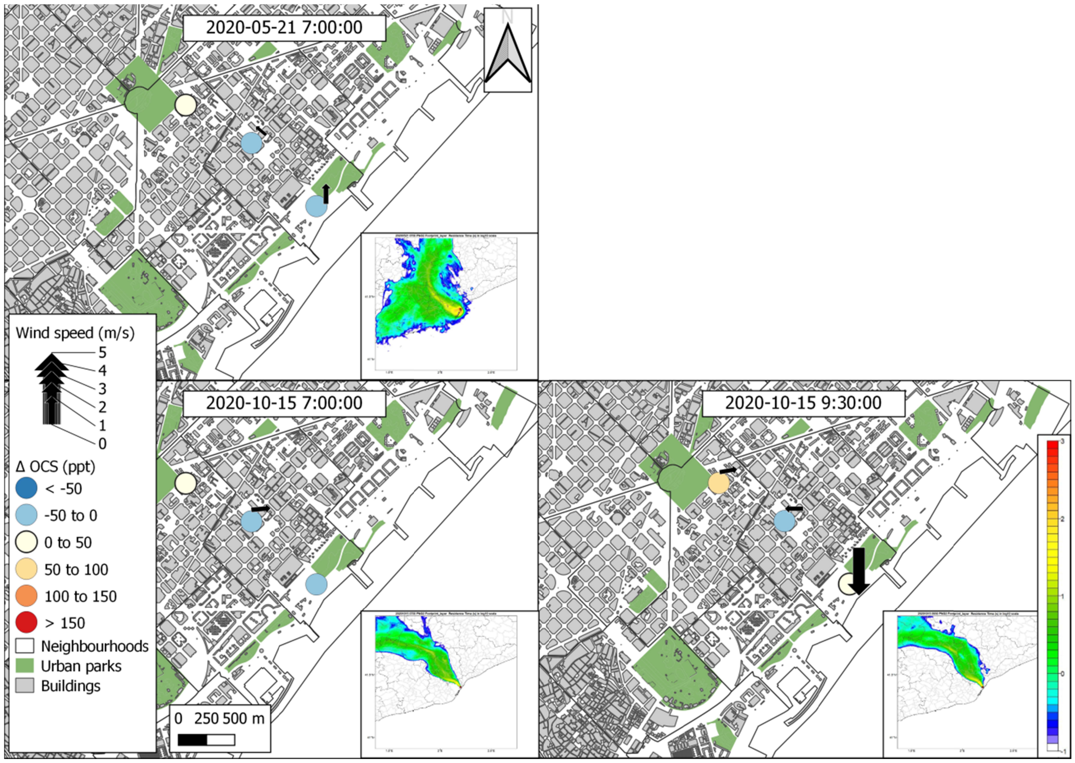

Fig. 6. OCS enhancement (Δ OCS) in ppt and calculated as measured OCS minus background OCS (484 ppt for May and 407 ppt for October) for each campaign at the two urban parks as follows: a) Sagrada Familia and b) Poblenou. The black arrow shows the wind direction and speed measured on site, and the absence of an arrow indicates that there was no wind blowing at the moment of measurement. A small map embedded in the lower right-hand corner of each panel shows the residence time on a logarithmic scale of the air masses arriving at the sampling site and determined with the FLEXPART model.

During the October campaign, there were no more mobility restrictions, and vehicle use was back to business as usual. OCS concentrations were higher than background values in both urban areas, as shown in the lower panels of Fig. 6. In the Sagrada Familia, the downwind location at 7:00 UTC had a record-high ΔOCS of +150 ppt, which was most likely capturing a local source of OCS since the close-by target and upwind sites registered + 7 and -7 ppt, respectively. The FLEXPART model indicates an influence of air mass with long residence coming from the city, which together with a low PBL (approximately 30 m) and the absence of local winds suggests that this peak of OCS is due to a nearby source of emission that was not present for the other two sampling sites. At 9:30 UTC, the air transport regime changes, and we observe a marine influence. The PBL development increases to 1085 m, and we also observe an increase in local winds (Fig. 6). Even in the midst of this increased air mixture and neutral OCS transport, ∆OCS increases up to 57 ppt, which points to local OCS sources in this urban area.

The other urban site, Poble Nou, did not exhibit such clear behavior of local OCS sources during October. ∆OCS were -17, -16 and +25 ppt at 7:00 UTC and 0, -16 and +70 ppt at 9:30 UTC for upwind, target, and downwind locations, respectively. The air masses were predicted to be influenced by regional sources, as FLEXPART suggests low residential periods in the urban area. There was moderate vertical air mixing (PBLH from 200 m at 7:00 UTC to 500 m at 9:30 UTC) and weak atmospheric stability (Table 1).

Agricultural: The Gavà and El Prat sampling sites are located in the Llobregat River basin, which is mostly dedicated to peri-urban agriculture. Of the 5,500 ha of urban agricultural land at the AMB, over 2,800 ha are in this basin, as shown in Fig. 1. The main agricultural products grown in this area are horticultural crops (such as lettuce, tomatoes, peppers, and artichokes), herbaceous crops, fruits, and some cereals (such as barley and alfalfa), and many short-cycle crops that are interannually rotated and well irrigated. Only the upwind site of Gavà is on the coast alongside the built infrastructure and urban forest and outside an agricultural field (sees supporting information Appendix S2 for pictures). The El Prat airport is nearby and between 3 and 5 km east to El Prat and Gavà, respectively. Gavà values were a clear example of how the wind component affected OCS mixing ratios since it is surrounded by the sea (south), agricultural and natural land (west to north) and is influenced by the port and the airport to the east.

Fig. 7a shows low OCS concentrations well below the background values with ∆OCS of -67, - +52, and -32 at 7:00 UTC in May during full photosynthetic activity of grown herbaceous fields, which indicates the drawdown of OCS by vegetation. The wind measured on site was mostly from the north, especially for the downwind site, as confirmed with the FLEXPART trajectory, which predicts a high residential time for air masses coming from the north where the agricultural fields are located. This indicates that the OCS drawdown might not be entirely a local effect of agriculture but could also be due to a more regional effect of COS taken up by soil and vegetation during the night all over Catalonia and then advected by the land breeze over the AMB. However, by 9:30 UTC, OCS concentrations increased (up to an ΔOCS of +116 for the downwind site) when air masses were coming from the urban and port areas and despite PBLH development, which reached 1380 m that morning. During the October campaign, southwesterly winds predominated both at 7:00 and 9:30 UTC, which brought in air masses from the port and Gavà urban area with high industrial activity resulting in ΔOCS between +82 and +40 ppt at 7:00 UTC. At 9:30 UTC, ΔOCS values decreased slightly and had less variability ranging from +49 to +55 ppt, and this indicated a more homogenous air mixture due to a more developed PBL, which increased from 21-84 to 380-519 m for that location. During October, air transport had much more influence on the OCS budget than the agricultural land use as it did during the May campaign when the fields were in full photosynthetic activity.

The opposite behavior was observed at the El Prat agricultural site, where a deep PBLH (1200 m) and regional air mass influence occurred in May, while a more stable situation and lower PBLH (691 m) dominated in October. In general, the values were similar to the background OCS for May with ΔOCS values of +25, +37, and +22 ppt at 7:00 UTC and even higher enhancements at 9:30 (+17, +44 and +173 ppt, Fig. 7b). FLEXPART back trajectories in May showed air masses coming from the east with longer residential times located in the sea but still received influence from the airport and the port of Barcelona. During the October campaign, El Prat had higher OCS enhancements at both sampling times (ΔOCS of +70, +33 and +80 ppt for 7:00 UTC; +7, +122 and +77 ppt for 9:30 UTC), which, given the low PBLH, suggests a local OCS source.

The FLEXPART showed that air masses came from the east indicating marine influence and/or from the port of Barcelona, where activities, such as air navigation and maritime traffic, had recovered 100% after the lockdown. The lower OCS concentrations in May compared to October highlight the significant sink of agriculture during the growing season as was seen for the Gavà location.

A) Gavà

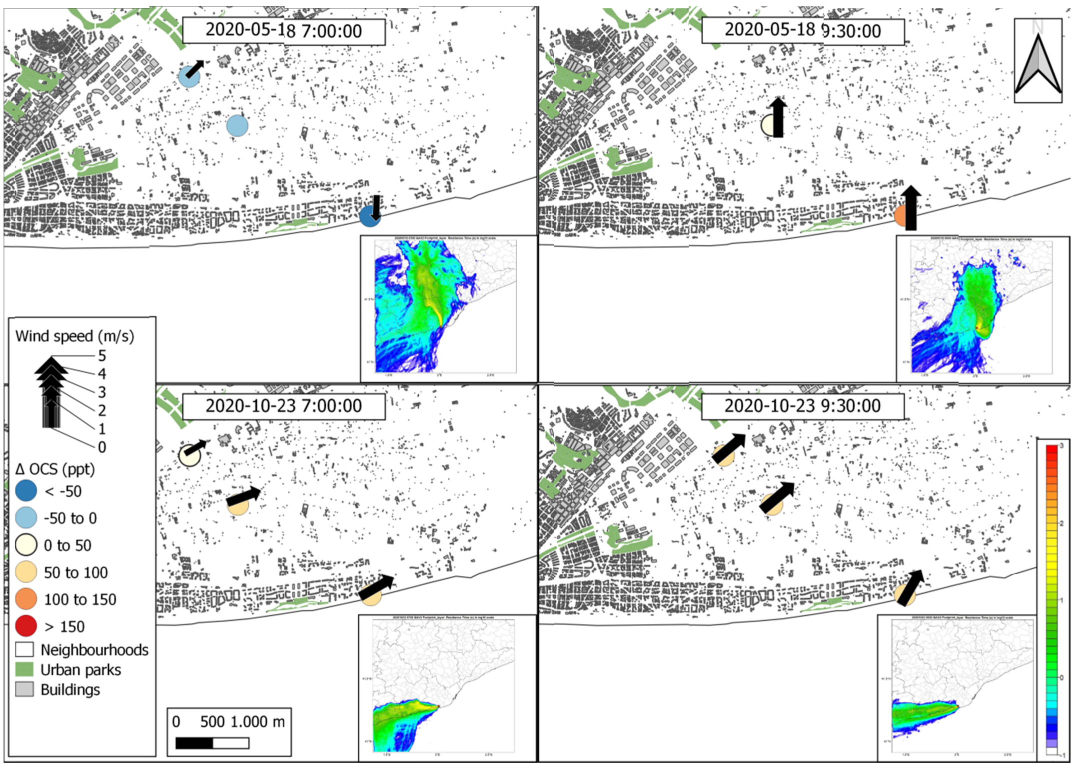

B) El Prat

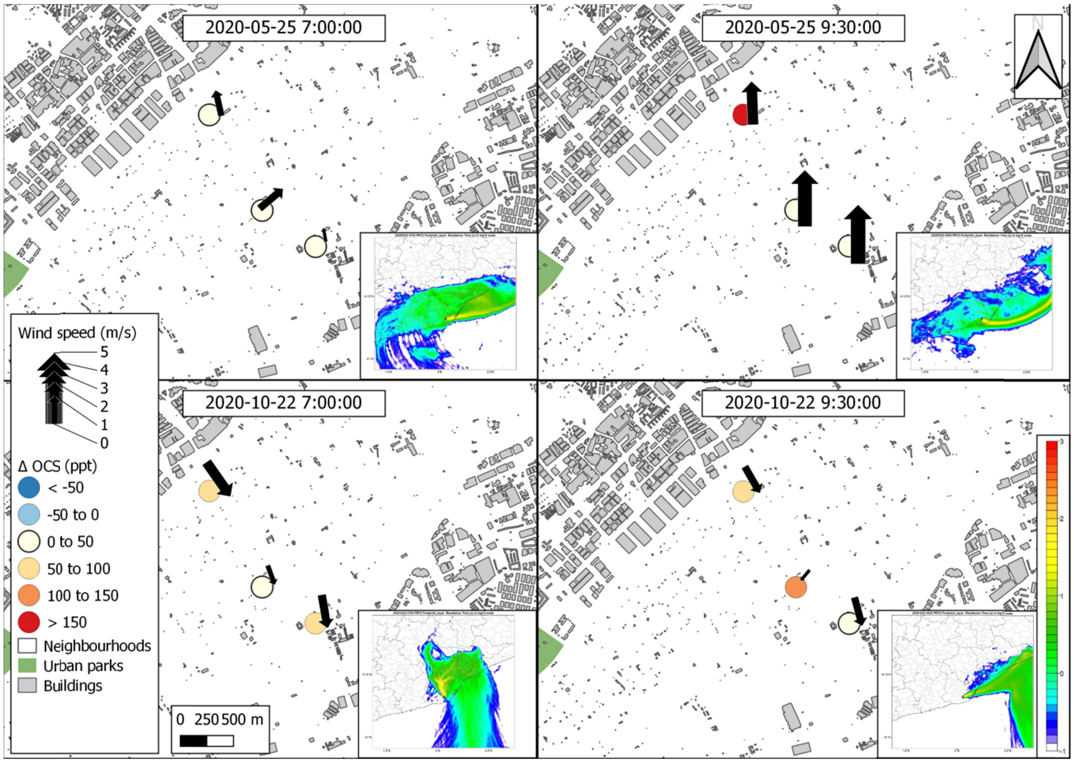

Fig. 7. OCS enhancement (Δ OCS) in ppt calculated as the measure of OCS minus background OCS (484 ppt for May and 407 ppt for October) for each campaign at the two urban parks as follows: a) Gavà and b) El Prat. The black arrow shows the wind direction and speed measured on site, and the absence of an arrow indicates that there was no wind blowing at the moment of measurement. A small map embedded in the lower right-hand corner of each panel shows the residence time on a logarithmic scale of the air masses arriving at the sampling site as determined with the FLEXPART model.

4.2. Considerations for OCS studies in urban ecosystems

Anthropogenic emissions are the primary source of OCS on a planetary scale, followed by oceanic flux (Remaud et al., 2023), they are significant at the local and urban scales. In our study, the peaks of OCS concentrations were mostly due to air masses coming from the port or the city, as was the case for Montjuic in October or Gavà during the May campaign, and reached values of 665 ppt for Montjuic and 600 ppt for Gavà (up to ΔOCS of +258 and +193 ppt, respectively).

There are various potential sources of OCS in urban areas, such as the erosion of automobile tires against asphalt, vehicle exhaust fumes, natural gas combustion and industrial processes including oil refineries and aluminum production (Yan et al., 2019). In fact, in their inventory, Yan et al. quantified the total emissions in 2015 for China alone as 174 Gg S yr^{-1} with the highest contributions coming from industrial OCS emission processes (120 Gg S yr^{-1}). In that same study, the total vehicle exhaust was responsible for 3 Gg S yr^{-1}, which is approximately half of the yearly global estimate of 6 Gg S $yr^{-}1$ given by Lee and Brimblecombe (2016). The latter study also indicated that the heavy fuel oil used in ships is a significant source of the OCS budget and produces 30 Gg S yr^{-1}. The AMB qualifies for all these potential sources and it has a heavily transited marine port that also has a combined cycle gas turbine power plant that runs on natural gas as well as an intense use of private vehicles within the city.

Additionally, a broad variety of sulfides are produced by wastewater where volatile organic compounds (VOC) such as MeSH, DMS, CS2, DMDS, DMTS and OCS are generated in anoxic environments of sewers (Lee and Brimblecombe, 2016), and it has been noted that the microbial activity in these anoxic sediments is closely linked to the production of OCS (Kitz et al., 2019). Sulfide emissions from urban wastewater networks are frequently detected due to their bad odor as is the case for Barcelona (Eijo-Río et al., 2015) and Thessaloniki (Besis et al., 2021). In our study, the sampling sites of Sagrada Familia in October (ΔOCS of +150 ppt) and Poble Nou (ΔOCS of +50 ppt) concur with locations of a combined sewer system previously reported to have high peaks of H_2S, which indicated a potential OCS source from wastewater. Unfortunately, constraining this signal from other potential urban sources was out of the scope of this study.

In terms of vegetated land uses, we found one case of a significant OCS drawdown in agricultural sites during the growing season of May. In addition to photosynthetic uptake (Campbell et al., 2017, 2008; Montzka et al., 2007), waterlogged soils have been reported to act as sinks of OCS when planted with crops (Yi et al., 2008). The agricultural fields of the Llobregat basin are mostly irrigated by inundation, which could further intensify the OCS uptake and explain the OCS drawdown at 7:00 UTC when photosynthetic activity was high. We also found values indicating uptake during the growing season in Collserola Forest, which is in agreement with other studies evaluating forest OCS uptake (Belviso et al., 2016; Campbell et al., 2017, 2008).

Finally, determining the influence of land use on the overall urban OCS budget requires a reliable background measurement. In general, background levels for OCS are associated with air masses coming from the sea because the stability provided by oceans results in constant OCS concentrations, at least at a seasonal scale (Montzka et al., 2007), as was the case for San Francisco (Villalba et al., 2021). However, this is not applicable for the AMB because the convection regime is quite peculiar. The AMB has a unique land–sea air mass exchange in which sea breezes under specific conditions do not bring new air masses but rather recycle air masses that originated over the urban area, however, a deeper research should be done in this regard, since marine contribution cannot be neglected. This type of process has been observed by Jaén et al. (2021), who described how ozone plumes stay over the shore due to advective processes during heat episodes such as heatwaves. The thermal component of convective processes creating episodes of air recirculation on the Spanish eastern coast has also been documented by Millán et al. (2000), where they outline how the sea breeze can favor the formation of layers of stratified air reservoirs in heights where compounds accumulate that can later return to the land. This particular sea breeze circulation constricts local ventilation and exacerbates the accumulation of anthropogenic gases emitted in the AMB.

5. Conclusions

We performed two measurement campaigns of OCS mixing ratios in the Metropolitan Area of Barcelona (AMB) to explore to what extent different urban land uses can have an impact on the OCS mixing ratios measured on flask samples regarding a particular urban climate, geography, and topography of AMB. Air samples were taken at locations representing four different land uses as follows: urban parks, forests, agricultural fields and impervious urban landscapes.

Based on the interflask comparison described in 2.3, we determined that the OCS measurement uncertainty can be as high as +53 ppt, which reflects that near-surface measurements in urban heterogeneous environments result in higher uncertainties than in homogenous rural environments. We also compared average OCS concentrations ±σ with values observed from ICOS- LSCE in Gif-sur-Yvete (GIF), which were taken at the same moment as our campaign (Fig. S3). We observed how mean OCS concentrations and σ in the AMB were systematically higher than in GIF, which suggests that anthropogenic emissions could affect the increase in uncertainty.

The ability to capture a photosynthetic signal appears weak in vegetated areas within the city, such as parks, and is relegated to forests and peri-urban agricultural areas. Urban parks showed values significantly higher than the established background value, both in May (i.e., up to +144 ppt) and in October (i.e., up to +150 ppt), which shows the influence of anthropogenic sources, possibly from the port and the city center, which masks the possibility of capturing the signal from the vegetation. The urban forest suggested OCS uptake values up to -33 ppt, which indicates a significant photosynthesis sink in denser vegetation masses even within city limits.

The urban area showed a variety of signals from almost neutral to above the background value, which suggests nearby emission sources. In our case, we found the explanation of some process values that may be aligned with urban traffic but above all with the industrial activity of the port and airport (for example, high OCS values in Montjuic when the wind came directly from the port). We can also think of other biogenic processes that produce OCS processes linked to human activity on urban land such as the waste system. These processes should be studied in more detail in future works. We have not been able to capture an effect of urban vegetation on OCS uptake; instead, the peri-urban area of agriculture and forests may have more important roles in the OCS dynamics in cities.

Last, agricultural areas showed a clear drawdown during the growing season for the location of Gavà, where we were able to discard regional influences and intense air mixing. OCS enhancements in October reflect the loss of photosynthetic uptake and the return to business as usual traffic and nearby airport and port activities.

Overall, the variability of OCS in the urban ecosystem was higher than we expected. The URBAG campaigns of OCS measurements showed evidence that the use of OCS as a trace gas to determine the contribution of the urban biosphere to the CO_2 budget is a complicated task and that the vegetation signal is difficult to detect because local anthropogenic activities have a significant influence. The urban ecosystem is complex in terms of land uptake, marine emissions, and anthropogenic emissions from the city port, and strongly impacts the spatial-temporal distribution of OCS in the AMB and impedes a clear constraint of the biosphere signal.

Acknowledgments

This work has been made possible thanks to the financial support of the European Research Council (ERC) Consolidator project: Integrated System Analysis of Urban Vegetation and Agriculture (818002-URBAG), the Spanish Ministry of Science, Innovation and Universities, through the “Maria de Maeztu” programme for Units of Excellence (CEX2019-000940-M), and the funding and recognition awarded to the research group Sostenipra (2021 SGR 00734) by the Department of Research and Universities of the Generalitat de Catalunya. This work also has been granted by the Spanish Ministry of Science and Innovation MCIN AEI/10.13039/501100011033 under contract PID2020-113614RB-C21, by the Spanish government under grant PRE2018-085425 and by the Catalan government under contract 2021 SGR 00574.

Open Research Section

The data acquired during the URBAG measurement campaigns used for the analysis of land influence in this study are available at ZENODO via https://doi.org/10.5281/zenodo.8072833 with Creative Commons Attribution 4.0 International license.

References:

Badia, A., Langemeyer, J., Codina, X., Gilabert, J., Guilera, N., Vidal, V., Segura, R., Vives, M., Villalba, G., 2021. A take-home message from COVID-19 on urban air pollution reduction through mobility limitations and teleworking. npj Urban Sustain. 1. https://doi.org/10.1038/s42949-021-00037-7

Belviso, S., Abadie, C., Montagne, D., Hadjar, D., Tropée, D., Vialettes, L., Kazan, V., Delmotte, M., Maignan, F., Remaud, M., Ramonet, M., Lopez, M., Yver-Kwok, C., Ciais, P., 2022. Carbonyl sulfide (COS) emissions in two agroecosystems in central France. PLoS One 17, 1–15. https://doi.org/10.1371/journal.pone.0278584

Belviso, S., Pison, I., Petit, J.E., Berchet, A., Remaud, M., Simon, L., Ramonet, M., Delmotte, M., Kazan, V., Yver-Kwok, C., Lopez, M., 2023. The Z-2018 emissions inventory of COS in Europe: A semiquantitative multi-data-streams evaluation. Atmos. Environ. 300, 119689. https://doi.org/10.1016/j.atmosenv.2023.119689

Belviso, S., Reiter, I.M., Loubet, B., Gros, V., Lathière, J., Montagne, D., Delmotte, M., Ramonet, M., Kalogridis, C., Lebegue, B., Bonnaire, N., Kazan, V., Gauquelin, T., Fernandez, C., Genty, B., 2016. A top-down approach of surface carbonyl sulfide exchange by a Mediterranean oak forest ecosystem in southern France. Atmos. Chem. Phys. 16, 14909–14923. https://doi.org/10.5194/acp-16-14909-2016

Besis, A., Georgiadou, E., Samara, C., 2021. Odor-active volatile organic compounds along the seafront of Thessaloniki, Greece. Implications for sources of nuisance odor. Sci. Total Environ. 799, 149388. https://doi.org/10.1016/j.scitotenv.2021.149388

Brioude, J., Arnold, D., Stohl, A., Cassiani, M., Morton, D., Seibert, P., Angevine, W., Evan, S., Dingwell, A., Fast, J.D., Easter, R.C., Pisso, I., Burkhart, J., Wotawa, G., 2013. The Lagrangian particle dispersion model FLEXPART-WRF version 3.1. Geosci. Model Dev. 6. https://doi.org/10.5194/gmd-6-1889-2013

Campbell, J.E., Carmichael, G.R., Chai, T., Mena-Carrasco, M., Tang, Y., Blake, D.R., Blake, N.J., Vay, S.A., Collatz, G.J., Baker, I., Berry, J.A., Montzka, S.A., Sweeney, C., Schnoor, J.L., Stanier, C.O., T. Chai, M., Mena-Carrasco, Y., Tang, D.R., Blake, N.J., Blake, S.A., Vay, G.J., Collatz, I., Baker, J.A., Berry, S.A., Montzka, C., Sweeney, J.L., And, S., Stanier, C.O., 2008. Photosynthetic Control of Atmospheric Carbonyl Sulfide During the Growing Season. Science (80-.). 1085–1088. https://doi.org/10.1126/science.1164015

Campbell, J.E., Whelan, M.E., Berry, J.A., Hilton, T.W., Zumkehr, A., Stinecipher, J., Lu, Y., Kornfeld, A., Seibt, U., Dawson, T.E., Montzka, S.A., Baker, I.T., Kulkarni, S., Wang, Y., Herndon, S.C., Zahniser, M.S., Commane, R., Loik, M.E., 2017. Plant Uptake of Atmospheric Carbonyl Sulfide in Coast Redwood Forests. J. Geophys. Res. Biogeosciences 122, 3391–3404. https://doi.org/10.1002/2016JG003703

Commane, R., Herndon, S.C., Zahniser, M.S., Lerner, B.M., McManus, J.B., Munger, J.W., Nelson, D.D., Wofsy, S.C., 2013. Carbonyl sulfide in the planetary boundary layer: Coastal and continental influences. J. Geophys. Res. Atmos. 118. https://doi.org/10.1002/jgrd.50581

Copernicus, 2023. ERA5 hourly data on single levels from 1940 to present [WWW Document]. URL https://cds.climate.copernicus.eu/cdsapp#!/dataset/reanalysis-era5-single-levels?tab=overview (accessed 5.21.23).

Eijo-Río, E., Petit-Boix, A., Villalba, G., Suárez-Ojeda, M.E., Marin, D., Amores, M.J., Aldea, X., Rieradevall, J., Gabarrell, X., 2015. Municipal sewer networks as sources of nitrous oxide, methane and hydrogen sulphide emissions: A review and case studies. J. Environ. Chem. Eng. https://doi.org/10.1016/j.jece.2015.07.006

Garcia-Dalmau, M., Udina, M., Bech, J., Sola, Y., Montolio, J., Jaén, C., 2021. Pollutant Concentration Changes During COVID-19 Lockdown in Barcelona and Surrounding Region: Modification of Diurnal Cycles and Limited Role of Meteorological Conditions In press.

GCOS, 2016. The Global Observing System For Climate Implementation Needs. World Meteorol. Organ. 200.

Gilabert, J., Ventura, S., Segura, R., Martilli, A., Badia, A., Llasat, C., Corbera, J., Villalba, G., 2021. Abating heat waves in a coastal Mediterranean city: What can cool roofs and vegetation contribute? Urban Clim. 37, 100863. https://doi.org/10.1016/J.UCLIM.2021.100863

Griffiths, A.D., Parkes, S.D., Chambers, S.D., McCabe, M.F., Williams, A.G., 2013. Improved mixing height monitoring through a combination of lidar and radon measurements. Atmos. Meas. Tech. 6. https://doi.org/10.5194/amt-6-207-2013

Grossi, C., Arnold, D., Adame, J.A., López-Coto, I., Bolívar, J.P., De La Morena, B.A., Vargas, A., 2012. Atmospheric 222Rn concentration and source term at El Arenosillo 100 m meteorological tower in southwest Spain. Radiat. Meas. 47. https://doi.org/10.1016/j.radmeas.2011.11.006

Guevara, M., Jorba, O., Soret, A., Petetin, H., Bowdalo, D., Serradell, K., Tena, C., Van Der Gon, H.D., Kuenen, J., Peuch, V.H., Pérez Garciá-Pando, C., 2021. Time-resolved emission reductions for atmospheric chemistry modelling in Europe during the COVID-19 lockdowns. Atmos. Chem. Phys. 21. https://doi.org/10.5194/acp-21-773-2021

Holzworth, G.C., 1964. Estimates of mean maximum mixing depths in the contiguous united states. Mon. Weather Rev. 92. https://doi.org/10.1175/1520-0493(1964)092<0235:eommmd>2.3.co;2

Institut d'Estadística de Catalunya, 2023. Idescat [WWW Document]. URL https://www.idescat.cat/ (accessed 5.21.23).

Jaén, C., Udina, M., Bech, J., 2021. Analysis of two heat wave driven ozone episodes in Barcelona and surrounding region: Meteorological and photochemical modeling. Atmos. Environ. 246. https://doi.org/10.1016/j.atmosenv.2020.118037

Kitz, F., Gómez-Brandón, M., Eder, B., Etemadi, M., Spielmann, F.M., Hammerle, A., Insam, H., Wohlfahrt, G., 2019. Soil carbonyl sulfide exchange in relation to microbial community composition: Insights from a managed grassland soil amendment experiment. Soil Biol. Biochem. 135, 28–37. https://doi.org/10.1016/j.soilbio.2019.04.005

Lee, C.L., Brimblecombe, P., 2016. Anthropogenic contributions to global carbonyl sulfide, carbon disulfide and organosulfides fluxes. Earth-Science Rev. 160, 1–18. https://doi.org/10.1016/J.EARSCIREV.2016.06.005

Leelőssy, Á., Mona, T., Mészáros, R., Lagzi, I., Havasi, Á., 2016. Eulerian and Lagrangian Approaches for Modelling of Air Quality. https://doi.org/10.1007/978-3-319-40157-7_5

Liu, S., Liang, X.-Z., 2010. Observed Diurnal Cycle Climatology of Planetary Boundary Layer Height. J. Clim. 23, 5790–5809. https://doi.org/10.1175/2010JCLI3552.1

Lotteraner, C., Piringer, M., 2016. Mixing-Height Time Series from Operational Ceilometer Aerosol-Layer Heights. Boundary-Layer Meteorol. 161. https://doi.org/10.1007/s10546-016-0169-2

Mallik, C., Chandra, N., Venkataramani, S., Lal, S., 2016. Variability of atmospheric carbonyl sulfide at a semi-arid urban site in western India. Sci. Total Environ. 551–552. https://doi.org/10.1016/j.scitotenv.2016.02.014

Millán, M.M., Mantilla, E., Salvador, R., Carratalá, A., Sanz, M.J., Alonso, L., Gangoiti, G., Navazo, M., 2000. Ozone cycles in the western Mediterranean basin: Interpretation of monitoring data in complex coastal terrain. J. Appl. Meteorol. 39. https://doi.org/10.1175/1520-0450(2000)039<0487:OCITWM>2.0.CO;2

Montzka, S.A., Calvert, P., Hall, B.D., Elkins, J.W., Conway, T.J., Tans, P.P., Sweeney, C.S., 2007. On the global distribution, seasonality, and budget of atmospheric carbonyl sulfide (COS) and some similarities to CO2. J. Geophys. Res. Atmos. 112, 1–15. https://doi.org/10.1029/2006JD007665

Protoschill-Krebs, G., Kesselmeier, J., 1992. Enzymatic Pathways for the Consumption of Carbonyl Sulphide (COS) by Higher Plants. Bot. Acta 105, 206–212. https://doi.org/10.1111/j.1438-8677.1992.tb00288.x

Querol, X., Alastuey, A., Ruiz, C.R., Artiñano, B., Hansson, H.C., Harrison, R.M., Buringh, E., Ten Brink, H.M., Lutz, M., Bruckmann, P., Straehl, P., Schneider, J., 2004. Speciation and origin of PM10 and PM2.5 in selected European cities. Atmos. Environ. 38, 6547–6555. https://doi.org/10.1016/j.atmosenv.2004.08.037

Remaud, M., Chevallier, F., Maignan, F., Belviso, S., Berchet, A., Parouffe, A., Abadie, C., Bacour, C., Lennartz, S., Peylin, P., 2022. Plant gross primary production, plant respiration and carbonyl sulfide emissions over the globe inferred by atmospheric inverse modelling. Atmos. Chem. Phys. 22. https://doi.org/10.5194/acp-22-2525-2022

Remaud, M., Ma, J., Krol, M., Abadie, C., Cartwright, M.P., 2023. Intercomparison of Atmospheric Carbonyl Sulfide (TransCom-COS ; Part One): Evaluating the Impact of Transport and Emissions on Tropospheric Variability Using Ground-Based and Aircraft

Data Journal of Geophysical Research : Atmospheres 1–23. https://doi.org/10.1029/2022JD037817

Ribeiro, I., Martilli, A., Falls, M., Zonato, A., Villalba, G., 2021. Highly resolved WRF-BEP/BEM simulations over Barcelona urban area with LCZ. Atmos. Res. 248, 105220. https://doi.org/10.1016/J.ATMOSRES.2020.105220

Salamanca, F., Krpo, A., Martilli, A., Clappier, A., 2010. A new building energy model coupled with an urban canopy parameterization for urban climate simulations-part I. formulation, verification, and sensitivity analysis of the model. Theor. Appl. Climatol. 99. https://doi.org/10.1007/s00704-009-0142-9

Segura, R., Badia, A., Ventura, S., Gilabert, J., Martilli, A., Villalba, G., 2021. Sensitivity study of PBL schemes and soil initialization using the WRF-BEP-BEM model over a Mediterranean coastal city. Urban Clim. 39. https://doi.org/10.1016/j.uclim.2021.100982

Seibert, P., Beyrich, F., Gryning, S.E., Joffre, S., Rasmussen, A., Tercier, P., 2000. Review and intercomparison of operational methods for the determination of the mixing height. Atmos. Environ. https://doi.org/10.1016/S1352-2310(99)00349-0

Servei Meteorològic de Catalunya, 2023. El temps a Catalunya [WWW Document]. URL https://www.meteo.cat/ (accessed 5.21.23).

Skamarock, W.C., Klemp, J.B., Dudhia, J., Gill, D.O., Liu, Z., Berner, J., Wang, W., Powers, J.G., Duda, M.G., Barker, D., Huang, X., 2021. A Description of the Advanced Research WRF Model Version 4.3. https://doi.org/10.5065/1dfh-6p97

Stewart, I.D., Oke, T.R., 2012. Local climate zones for urban temperature studies. Bull. Am. Meteorol. Soc. 93. https://doi.org/10.1175/BAMS-D-11-00019.1

Stohl, A., Forster, C., Frank, A., Seibert, P., Wotawa, G., 2005. Technical note: The Lagrangian particle dispersion model FLEXPART version 6.2. Atmos. Chem. Phys. 5. https://doi.org/10.5194/acp-5-2461-2005

Stull, R.., 1988. An Introduction to Boundary Layer Meteorology. Kluwer Academic Publishers.

Sturm, P., Leuenberger, M., Sirignano, C., Neubert, R.E.M., Meijer, H.A.J., Langenfelds, R., Brand, W.A., Tohjima, Y., 2004. Permeation of atmospheric gases through polymer O-rings used in flasks for air sampling. J. Geophys. Res. D Atmos. 109.

URBAG, 2023. Full dataset of carbonyl sulfide URBAG measurement campaign May and October 2020 [Data set]. Zenodo. https://doi.org/10.5281/zenodo.8072833

VAISALA, 2020. Investigation of Boundary Layer Structures with Ceilometer [WWW Document]. VAISALA. URL https://www.vaisala.com/en/products/software/bl-view

Villalba, G., Whelan, M., Montzka, S.A., Cameron-Smith, P.J., Fischer, M., Zumkehr, A., Hilton, T., Stinecipher, J., Baker, I., Bambha, R.P., Michelsen, H.A., LaFranchi, B.W., Estruch, C., Campbell, E., 2021. Exploring the Potential of Using Carbonyl Sulfide to Track the Urban Biosphere Signal. J. Geophys. Res. Atmos. 126. https://doi.org/10.1029/2020JD034106

Whelan, M.E., Lennartz, S.T., Gimeno, T.E., Wehr, R., Wohlfahrt, G., Wang, Y., Kooijmans, L.M.J., Hilton, T.W., Belviso, S., Peylin, P., Commane, R., Sun, W., Chen, H., Kuai, L., Mammarella, I., Maseyk, K., Berkelhammer, M., Li, K.F., Yakir, D., Zumkehr, A., Katayama, Y., Oge, J., Spielmann, F.M., Kitz, F., Rastogi, B., Kesselmeier, J., Marshall, J., Erkkila, K.M., Wingate, L., Meredith, L.K., He, W., Bunk, R., Launois, T., Vesala, T., Schmidt, J.A., Fichot, C.G., Seibt, U., Saleska, S., Saltzman, E.S., Montzka, S.A., Berry, J.A., Elliott Campbell, J., 2018. Reviews and syntheses: Carbonyl sulfide as a multi-scale tracer for carbon and water cycles, Biogeosciences. https://doi.org/10.5194/bg-15-3625-2018

Yan, Y., Li, R., Peng, L., Yang, C., Liu, C., Cao, J., Yang, F., Li, Y., Wu, J., 2019. Emission inventory of carbonyl sulfide (COS) from primary anthropogenic sources in China. Environ. Pollut. 247, 745–751. https://doi.org/10.1016/j.envpol.2019.01.096

Yang, F., Qubaja, R., Tatarinov, F., Rotenberg, E., Yakir, D., 2018. Assessing canopy performance using carbonyl sulfide measurements. Glob. Chang. Biol. 24, 3486–3498. https://doi.org/10.1111/gcb.14145

Yi, Z., Wang, X., Sheng, G., Fu, J., 2008. Exchange of carbonyl sulfide (OCS) and dimethyl sulfide (DMS) between rice paddy fields and the atmosphere in subtropical China. Agric. Ecosyst. Environ. 123, 116–124. https://doi.org/10.1016/j.agee.2007.05.011

Yu, J., Steinberger, Y., 2011. Vertical Distribution of Microbial Community Functionality under the Canopies of Zygophyllum dumosum and Hammada scoparia in the Negev Desert, Israel. Microb. Ecol. 62, 218–227.

Zumkehr, A., Hilton, T.W., Whelan, M., Smith, S., Campbell, J.E., 2017. Gridded anthropogenic emissions inventory and atmospheric transport of carbonyl sulfide in the U.S. J. Geophys. Res. 122, 2169–2178. https://doi.org/10.1002/2016JD025550

Zumkehr, A., Hilton, T.W., Whelan, M., Smith, S., Kuai, L., Worden, J., Campbell, J.E., 2018. Global gridded anthropogenic emissions inventory of carbonyl sulfide. Atmos. Environ. 183, 11–19. https://doi.org/10.1016/j.atmosenv.2018.03.063

Figure 1.

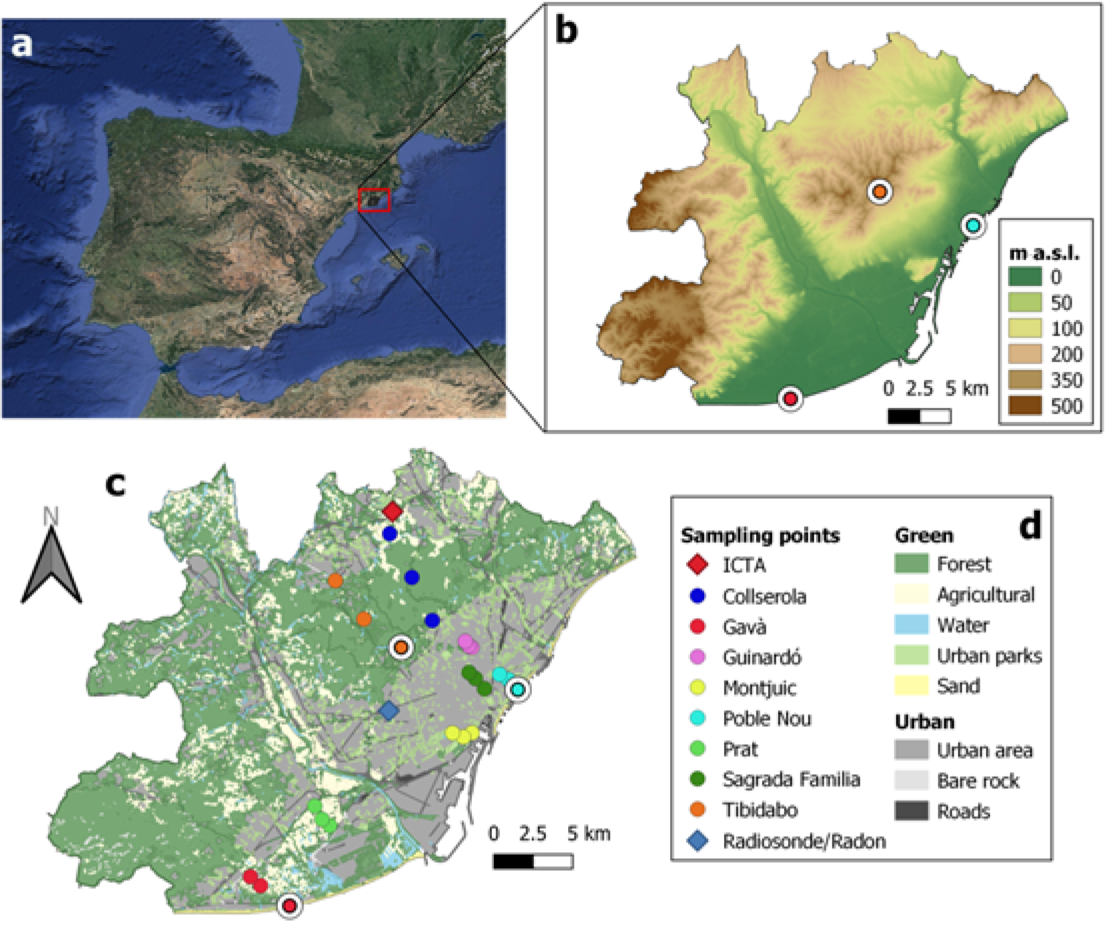

a
b
m a.s.l.
0
50
100
200
350
500
0 2.5 5 km
c
N
0 2.5 5 km
d
Sampling points
ICTA
Collserola
Gavà
Guinardó
Montjuic
Poble Nou
Prat
Sagrada Familia
Tibidabo
Radiosonde/Radon
Green
Forest
Agricultural
Water
Urban parks
Sand
Urban
Urban area
Bare rock
Roads

Figure 2.

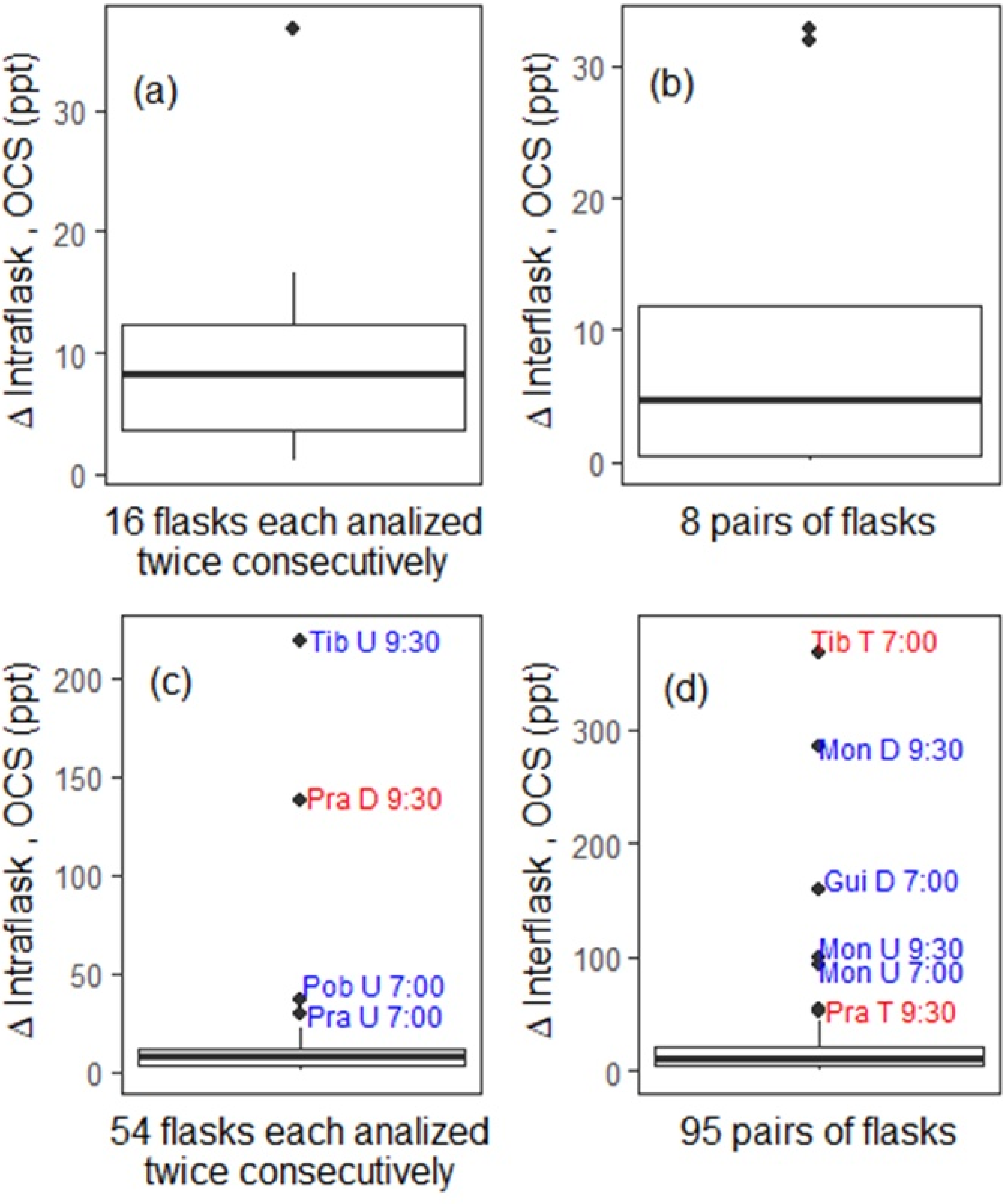

(a)
Δ Intraflask , OCS (ppt)
16 flasks each analized twice consecutively
(b)
Δ Interflask , OCS (ppt)
8 pairs of flasks
(c)
Δ Intraflask , OCS (ppt)
Tib U 9:30
Pra D 9:30
Pob U 7:00
Pra U 7:00
54 flasks each analized twice consecutively
(d)
Δ Interflask , OCS (ppt)
Tib T 7:00
Mon D 9:30
Gui D 7:00
Mon U 9:30
Mon U 7:00
Pra T 9:30
95 pairs of flasks

Figure 3.

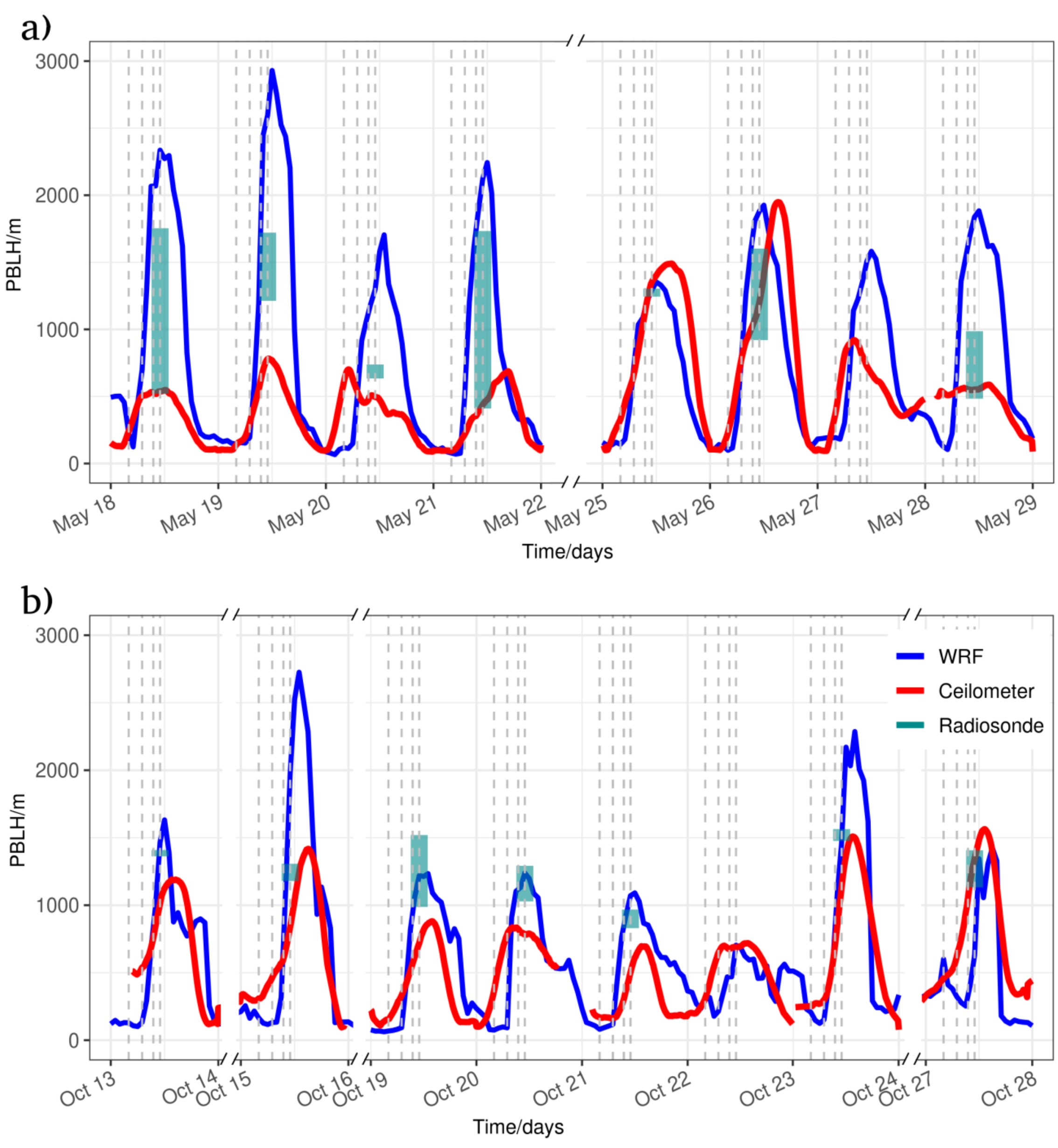

a)
3000
2000
1000
0
PBLH/m
May 18
May 19
May 20
May 21
May 22
May 25
May 26
May 27
May 28
May 29
Time/days
b)
Oct 13
Oct 14
Oct 15
Oct 16
Oct 19
Oct 20
Oct 21
Oct 22
Oct 23
Oct 24
Oct 27
Oct 28
WRF
Ceilometer
Radiosonde

Figure 4.

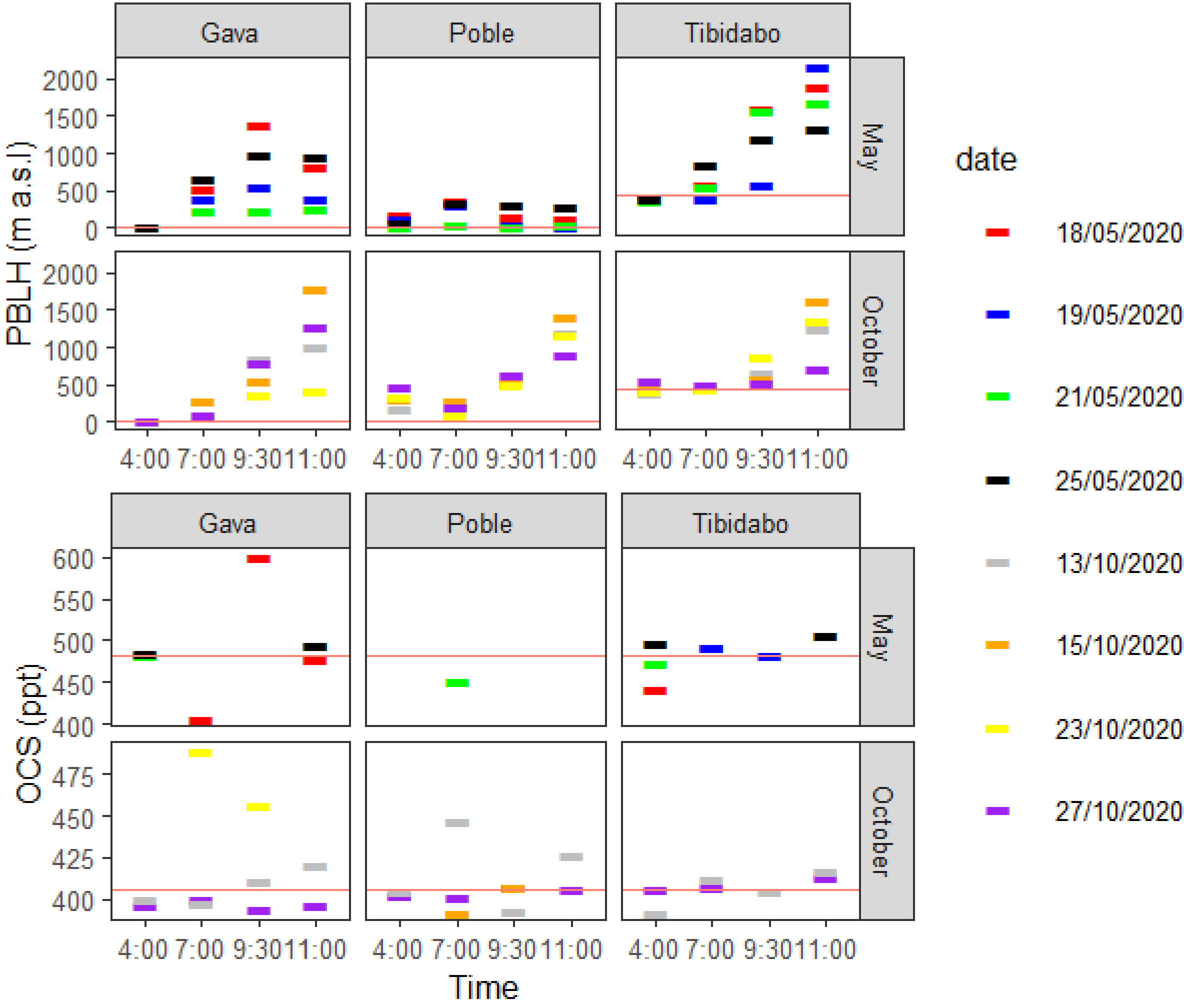
Gava
Poble
Tibidabo
May
October
PBLH (m a.s.l.)
2000
1500
1000
500
0
4:00 7:00 9:30 11:00
OCS (ppt)
600
550
500
450
400
475
425
Time
date
18/05/2020
19/05/2020
21/05/2020
25/05/2020
13/10/2020
15/10/2020
23/10/2020
27/10/2020

Figure 5a.

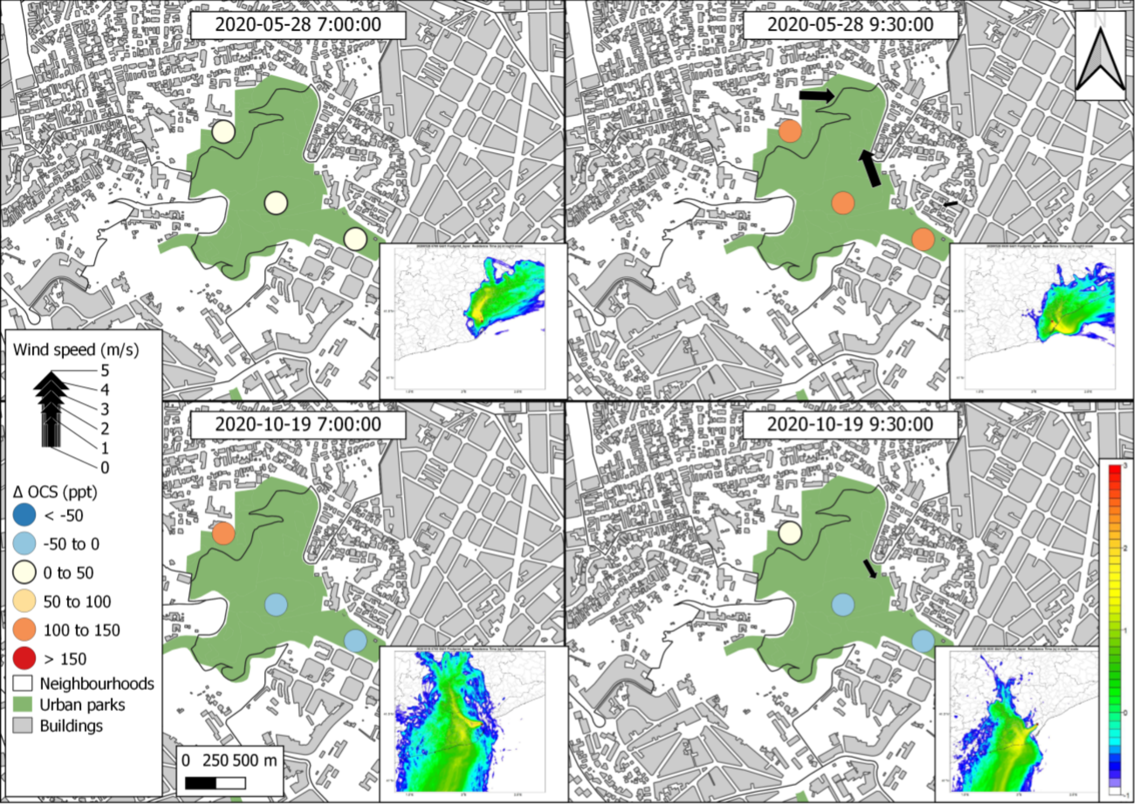
2020-05-28 7:00:00
2020-05-28 9:30:00
2020-10-19 7:00:00
2020-10-19 9:30:00
N
Wind speed (m/s)
5
4
3
2
1
0
Δ OCS (ppt)
< -50
-50 to 0
0 to 50
50 to 100
100 to 150
> 150
Neighbourhoods
Urban parks
Buildings
0 250 500 m

Figure 5b.

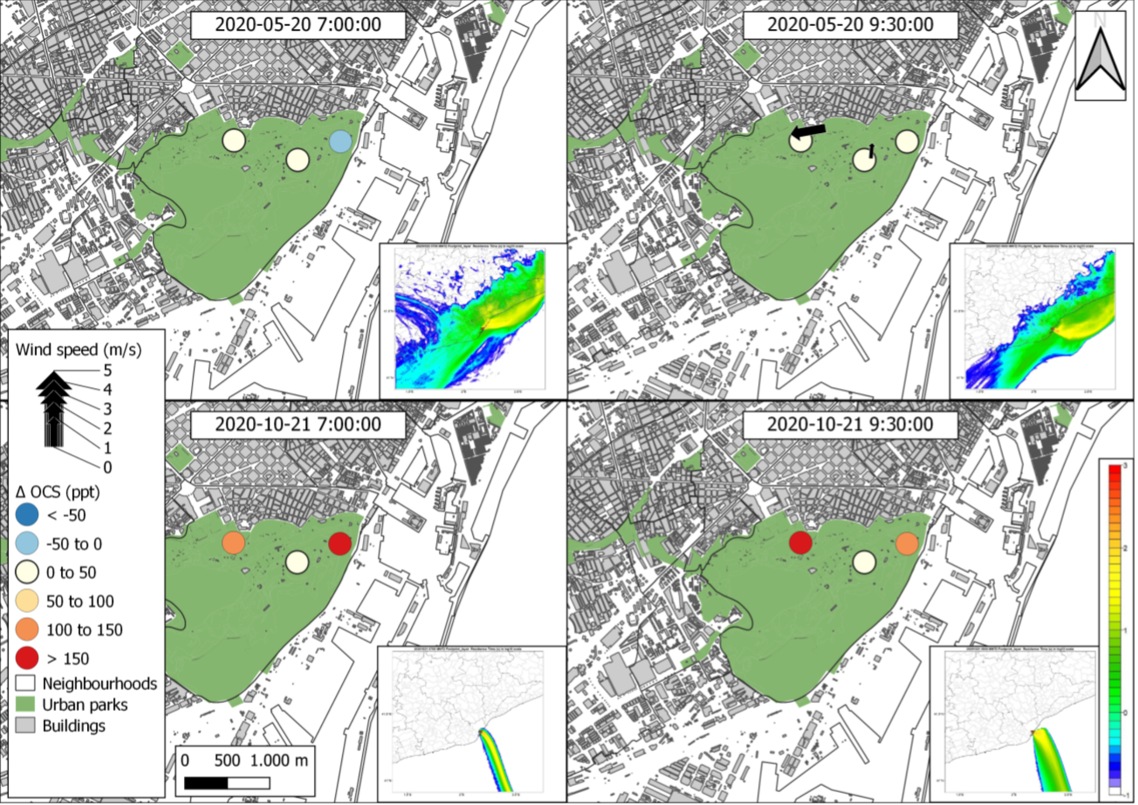
2020-05-20 7:00:00
2020-05-20 9:30:00
2020-10-21 7:00:00
2020-10-21 9:30:00
N
Wind speed (m/s)
5
4
3
2
1
0
Δ OCS (ppt)
< -50
-50 to 0
0 to 50
50 to 100
100 to 150
> 150
Neighbourhoods
Urban parks
Buildings
0 500 1.000 m
3
2
1
0
-1

Figure 6a.

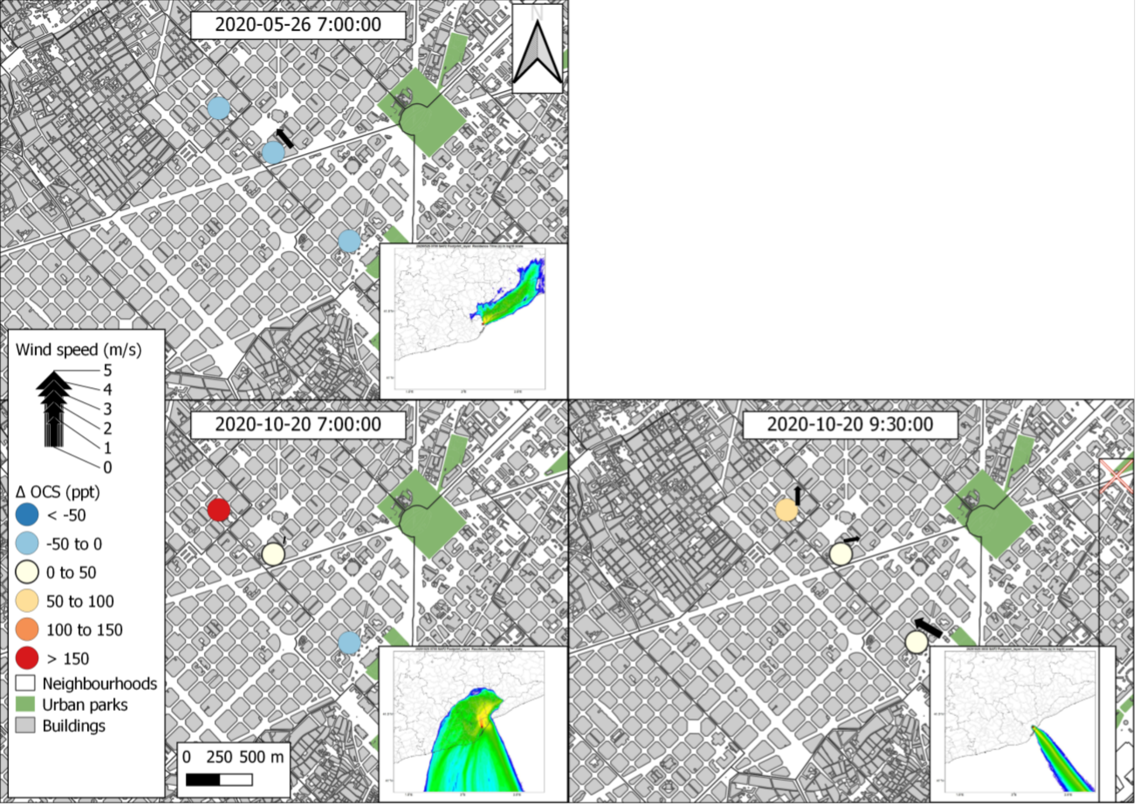
2020-05-26 7:00:00
2020-10-20 7:00:00
2020-10-20 9:30:00
N
Wind speed (m/s)
5
4
3
2
1
0
Δ OCS (ppt)
< -50
-50 to 0
0 to 50
50 to 100
100 to 150
> 150
Neighbourhoods
Urban parks
Buildings
0 250 500 m

Figure 6b.

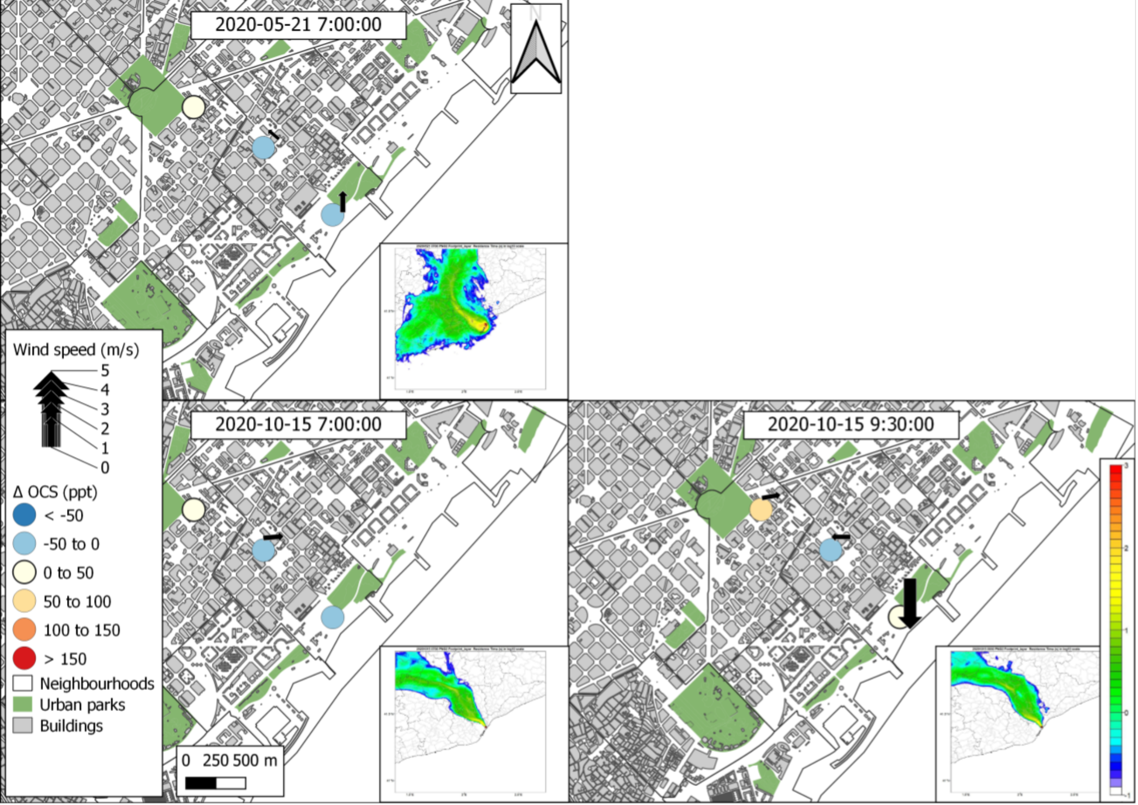

2020-05-21 7:00:00
N
2020-10-15 7:00:00
2020-10-15 9:30:00
Wind speed (m/s)
5
4
3
2
1
0
Δ OCS (ppt)
< -50
-50 to 0
0 to 50
50 to 100
100 to 150
> 150
Neighbourhoods
Urban parks
Buildings
0 250 500 m
3
2
1
0
-1

Figure 7a.

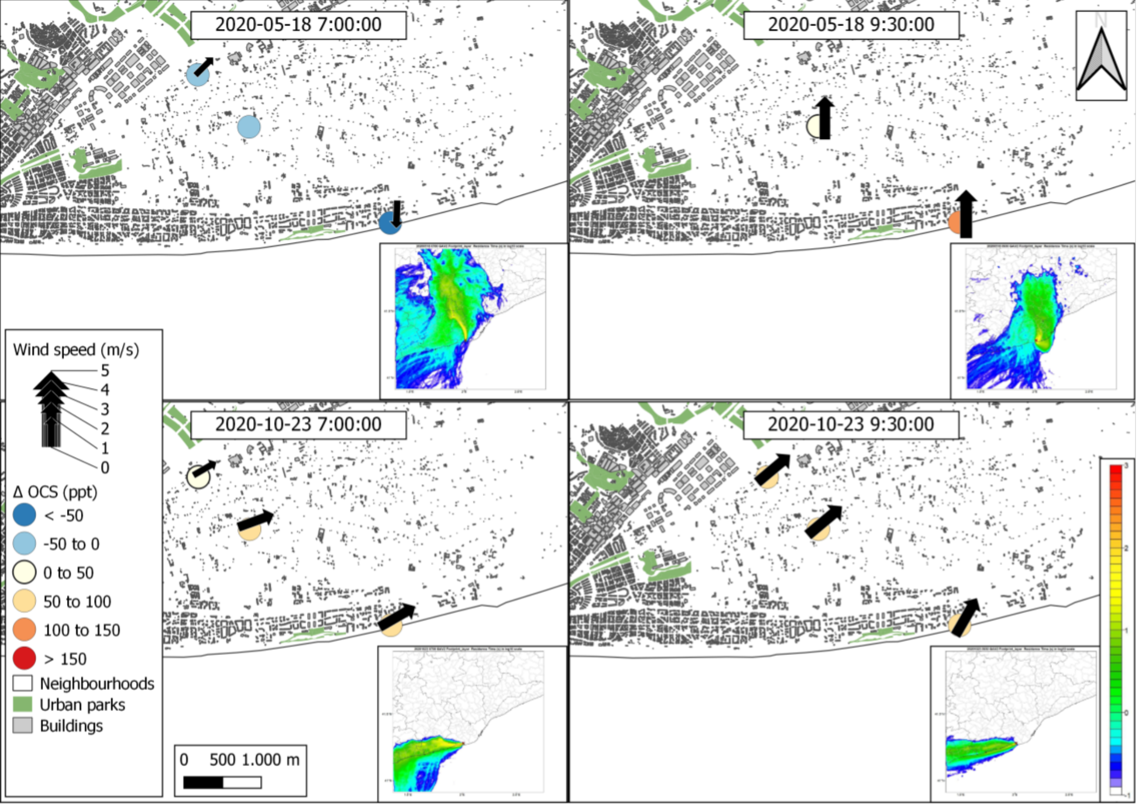
2020-05-18 7:00:00
2020-05-18 9:30:00
N
2020-10-23 7:00:00
2020-10-23 9:30:00
Wind speed (m/s)
5
4
3
2
1
0
Δ OCS (ppt)
< -50
-50 to 0
0 to 50
50 to 100
100 to 150
> 150
Neighbourhoods
Urban parks
Buildings
0 500 1.000 m

Figure 7b.

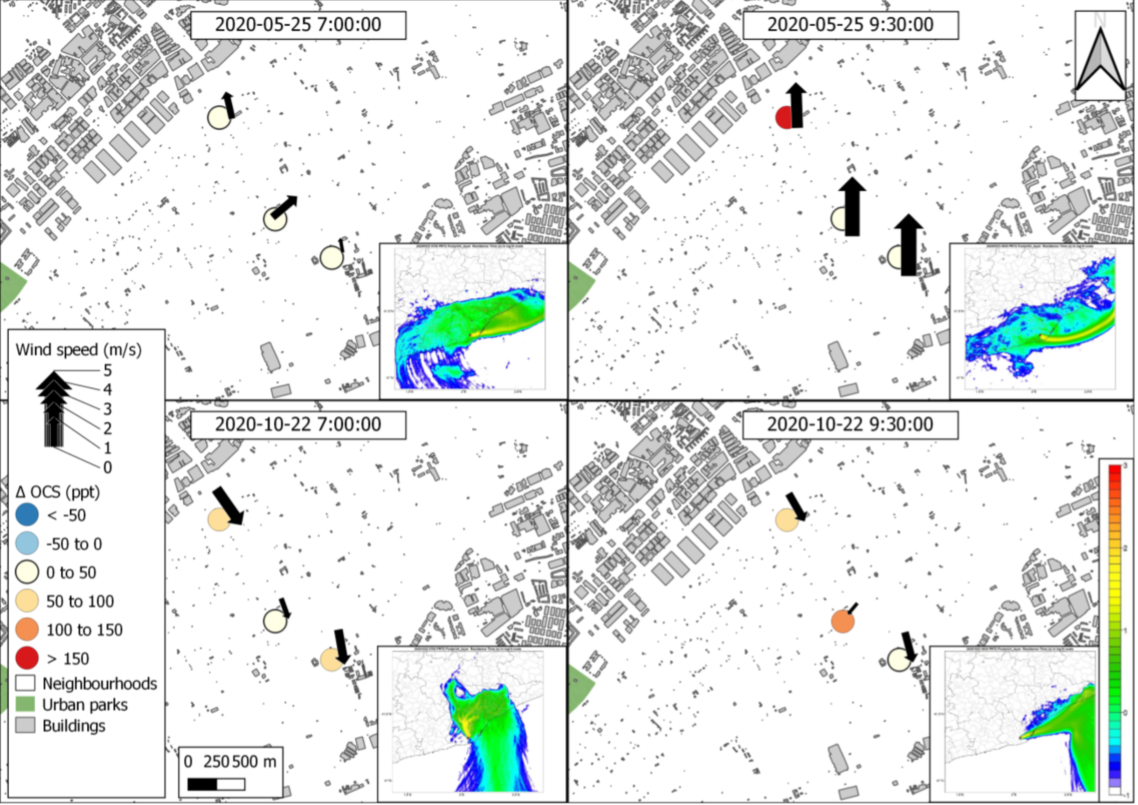
2020-05-25 7:00:00
2020-05-25 9:30:00
N
2020-10-22 7:00:00
2020-10-22 9:30:00
Wind speed (m/s)
5
4
3
2
1
0
Δ OCS (ppt)
< -50
-50 to 0
0 to 50
50 to 100
100 to 150
> 150
Neighbourhoods
Urban parks
Buildings
0 250 500 m

Supporting Information of:

Exploring the influence of land use on the urban carbonyl sulfide budget: a case study of the Metropolitan Area of Barcelona

Carme Estruch[1,2], Sauveur Belviso[3], Alba Badia[1], Veronica Vidal[1,4], Roger Curcoll[1,5], Mireia Udina[6], Claudia Grossi[5], Josep-Anton Morguí[1,7], Ricard Segura[1], Sergi Ventura[1], Yolanda Sola[6], Gara Villalba[1,8]*.

[1]Institut de Ciència i Tecnologia Ambientals (ICTA), Universitat Autònoma de Barcelona, 08193 Cerdanyola del Vallès, Barcelona, Spain.

[2] Eurecat, Centre Tecnològic de Catalunya, Climate Change Research Department, Amposta, Spain.

[3]Laboratoire des Sciences du Climat et de l'Environnement, LSCE, Paris-Saclay, France.

[4]Department of Computer Architecture and Operative Systems, Universitat Autònoma de Barcelona (UAB), Spain.

[5]INTE, Universitat Politècnica de Catalunya, Av. Diagonal 647, 08028, Barcelona, Spain.

[6]Departament de Física Aplicada–Meteorologia, Universitat de Barcelona, Barcelona, Spain.

[7]Departament de Biologia Evolutiva, Ecologia i Ciències Ambientals, Universitat de Barcelona, Barcelona, Spain.

[8]Department of Chemical, Biological and Environmental Engineering, Universitat Autònoma de Barcelona (UAB), Spain.

Table S1. Table with values of OCS (ppt) at every date, location and group in campaign May and October 2020: Wind direction in degrees; Wind speed m/s; temperature in ºC, and Pressure is QFE in hPa; relative humidity (RH) is in %; PBLH is extracted from WRF model and is in m.

Date m-d	Location	Group (Altitude)	Lat,lon	Hour UTC	OCS ppt	WRF PBLH	WRF temp	Wind direction	Wind Speed	Air temperature	Air pressure	RH
05-18	Gavà	Downwind (2)	41.268, 2.032	7:00	407.1±8.5	534	19.45	2	0.87	23.4	1019	-
				9:30	600.9±30.3	1380	23.10	180	2.29	22.8	1019	-
				11:00	477.5±17.9	816	21.64	140	1.15	26.2	1019	-
		Target (1)	41.279, 2.010	7:00	432.7±13.3	577	19.69	-	0.00	21.2	1018	-
				9:30	522.9±15.7	1498	23.49	180	1.88	23.8	1019	-
		southern (-2)	41.285, 2.002	7:00	452.9±9.3	592	19.81	225	0.73	23.1	1018	-
				9:30	NA	1578	23.66	215	2.43	27.4	1018	-
	Tibidabo	Downwind (442)	41.418, 2.116	4:00	443.3±4.4	18	13.59	-	0.00	13.7	966	-
05-19	Tibidabo	southern (442)	41.418, 2.116	7:00	491.9±12.8	19	17.39	340	2.34	18.9	964	-
				9:30	482.0±30.3	224	20.84	12	1.17	23.9	964	-
		Target (320)	41.435, 2.087	7:00	620.2±260.2	193	17.74	270	0.92	17.3	978	-
				9:30	499.4±16.1	406	21.59	280	0.04	24.5	977	-
		Downwind (175)	41.457, 2.065	7:00	463.4±1.3	210	18.19	275	1.43	19.9	994	-
				9:30	499.8±NA	441	21.98	270	1.52	29.6	994	-
05-20	Montjuic	southern (58)	41.369, 2.171	7:00	471.1±12.6	327	21.93	-	0.00	22.02	1007	-
				9:30	496.1±0.9	567	23.20	-	0.00	22.5	1007	-
		Target (98)	41.367, 2.165	7:00	483.9±2.3	327	21.93	-	0.00	19.7	1001	-
				9:30	484.3±0.4	567	23.20	185	0.32	25.5	1001	-
		Downwind (42)	41.369, 2.156	7:00	500.1±5.5	430	22.51	-	0.00	22.6	1008	-
				9:30	489.7±1.1	883	24.96	80	1.34	29.9	1008	-
05-21	Poble Nou	southern (4)	41.395, 2.206	7:00	451.8±0.3	44	21.65	180	0.56	26.4	1016	-
		Target (0)	41.400, 2.199	7:00	448.1±7.9	142	23.27	130	0.28	23.1	1016	-

		Downwind (4)	41.403, 2.192	7:00	484.6±22.6	234	24.17	-	0.00	27.2	1016	-
	Gavà	southern (2)	41.268, 2.032	4:00	482.1±NA	11	18.43	347	1.05	16.2	1016	-
				11:00	495.5±10.7	249	23.97	240	3.40	31.1	1017	-
	Tibidabo	southern (442)	41.418, 2.116	4:00	472.7±2.6	9	19.42	347	0.94	19.9	965	-
05-25	Prat	southern (0)	41.315, 2.063	7:00	509.2±16.8	737	21.70	170	0.30	26.7	1025	-
				9:30	501.7±12.4	1084	23.23	180	3.57	25.1	1025	-
		Target (0)	41.318, 2.057	7:00	521.9±30.2	736	21.62	230	1.14	26.9	1024	-
				9:30	528.9±37.9	1085	23.27	180	3.29	26.5	1024	-
		Downwind (2)	41.326, 2.051	7:00	506.4±2.5	827	21.87	167	0.88	27.6	1024	-
				9:30	657.6±57.3	1182	24.35	178	2.07	32.6	1024	-
	Gavà	southern (2)	41.268, 2.032	4:00	486.0±31.8	9	16.91	20	0.00	19.8	1024	-
				11:00	495.8±4.4	960	22.76	240	3.50	28	1025	-
	Tibidabo	southern (442)	41.418, 2.116	4:00	496.4±7.9	27	16.73	-	0.00	21.5	972	-
				11:00	507.9±2.2	958	21.47	252	1.20	29.6	973	-
05-26	Sagrada Familia	southern (37)	41.395, 2.181	7:00	462.4±1.0	771	23.21	240	0.00	22.5	1023	-
		Target (54)	41.401, 2.174	7:00	452.3±7.6	806	23.21	140	0.69	24.2	1020	-
		Downwind (55)	41.404, 2.169	7:00	464.9±20.6	806	23.21	-	0.00	24.2	1018	-
05-27	Collserola	southern (155)	41.434, 2.140	7:00	468.9±22.8	441	20.96	80	0.00	24.4	1003	-
				9:30	493.1±NA	1079	22.96	-	0.00	23.4	1004	-
		Target (107)	41.459, 2.2.12	7:00	412.6±13.8	395	20.28	-	0.72	19.4	1006	-
				9:30	498.3±12.6	1133	23.24	355	1.94	24	1006	-
		Downwind (442)	41.435, 2.087	7:00	451.0±37.4	289	19.82	-	0.00	23.7	1011	-
				9:30	499.5±4.2	1076	23.06	120	3.62	29.7	1012	-
05-28	Guinardó	southern (115)	41.419, 2.171	7:00	495.0±8.7	590	21.30	180	0.00	21	1011	-
				9:30	594.3±5.6	1524	24.52	80	0.31	25.8	1010	-

		Target	41.420,	7:00	512.2±8.2	590	21.30	140	0.00	21.3	1003	-
		(169)	2.168	9:30	612.8±13.7	1524	24.52	160	1.60	22.6	1002	-
		Downwind	41.422,	7:00	506.7±2.6	590	21.30	-	0.00	24.5	1008	-
		(127)	2.166	9:30	628.8±20.5	1524	24.52	272	1.36	26.1	1007	-
10-13	Gavà	southern	41.268,	4:00	400.5±3.0	31	14.31	5	0.83	12.9	1011	75
		(2)	2.032	7:00	398.3±6.1	62	14.12	5	1.88	13	1011	60
				9:30	410.8±6.0	846	18.35	25	2.00	17.8	1011	49
				11:00	420.1±5.8	1004	19.84	10	0.77	22.6	1010	41
	Poble Nou	southern	41.395,	4:00	405.3±5.8	181	17.36	310	2.00	15.4	1011	49
		(4)	2.206	7:00	447.6±3.1	210	17.45	340	1.31	17.1	1011	50
				9:30	392.9±8.8	639	18.46	340	2.35	19.3	1011	42
				11:00	426.1±19.8	1202	19.97	60	1.70	21.5	1011	52
	Tibidabo	southern	41.418,	4:00	392.1±5.5	23	10.36	355	1.40	8.4	959	70
		(442)	2.116	7:00	412.2±10.2	69	11.07	350	2.44	11.3	954	57
				9:30	404.5±5.8	302	13.56	340	0.04	17.9	960	40
				11:00	416.9±12.9	879	17.30	298	0.70	22.3	959	39
10-15	Poble Nou	southern	41.395,	7:00	390.4±15.7	287	15.61	310	0.00	11.8	1010	59
		(4)	2.206	9:30	407.9±2.4	525	16.82	360	2.48	17.5	1011	-
		Target	41.400,	7:00	391.6±3.1	226	12.42	265	0.51	11	1012	55
		(0)	2.199	9:30	391.1±2.9	530	14.96	90	0.46	18.8	1010	37
		Downwind	41.403,	7:00	432.1±3.9	199	12.50	56	0.00	13.1	1010	63
		(4)	2.192	9:30	477.6±19.5	571	15.08	260	0.45	19.4	1010	50
10-19	Guinardó	southern	41.419,	7:00	374.1±8.6	69	14.82	340	0.00	14.8	1007	82
		(115)	2.171	9:30	392.4±9.8	934	18.23	340	0.00	17.7	1008	66
		Target	41.420,	7:00	403.4±7.2	69	14.82	-	0.00	15	999	75
		(169)	2.168	9:30	375.6±NA	934	18.23	330	0.56	17.6	1000	66
		Downwind	41.422,	7:00	520.8±112.8	69	14.82	-	0.00	13	1003	75
		(127)	2.166	9:30	409.1±7.5	934	18.23	-	0.00	17.6	1004	66
10-20	Sagrada	southern	41.395,	7:00	397.3±5.2	29	17.60	-	0.00	16.7	1017	77
		(37)	2.181	9:30	442.5±6.3	1084	19.91	120	1.08	20.5	1017	69
		Target	41.401,	7:00	414.3±19.9	32	17.03	190	0.11	17	1014	78

		(54)	2.174	9:30	426.0±3.0	1085	19.66	260	0.38	21.6	1014	64
		Downwind	41.404,	7:00	567.5±1.5	32	17.03	-	0.00	17.6	1012	77
		(55)	2.169	9:30	464.9±22.7	1085	19.66	180	0.50	20.9	1014	66
10-21	Montjuic	southern	41.369,	7:00	665.1±54.5	92	20.87	-	0.00	19.7	1004	85
		(58)	2.171	9:30	550.3±71.1	561	22.10	350	0.00	21.1	1004	77
		Target	41.367,	7:00	423.1±10.9	92	20.87	-	0.00	18.9	998	91
		(98)	2.165	9:30	425.0±10.7	561	22.10	260	0.00	23.3	998	70
		Downwind	41.369,	7:00	546.4±12.3	90	20.82	-	0.00	19.3	1005	91
		(42)	2.156	9:30	635.3±164.6	734	22.45	-	0.00	23.5	1005	72
10-22	Prat	southern	41.315,	7:00	477.4±20.7	108	19.76	350	1.34	18.5	1014	87
		(0)	2.063	9:30	454.0±2.8	435	21.52	345	1.07	21.6	1014	70
		Target	41.318,	7:00	440.6±5.6	98	19.74	340	0.58	18.4	1012	86
		(0)	2.057	9:30	529.3±8.5	458	21.59	40	0.30	20.8	1013	71
		Downwind	41.326,	7:00	487.3±8.5	103	19.66	325	1.95	18.8	1013	82
		(2)	2.051	9:30	486.5±9.2	495	21.69	330	1.12	21	1013	70
10-23	Gavà	southern	41.268,	7:00	489.3±24.9	84	18.79	240	1.74	18.9	1016	87
		(2)	2.032	9:30	456.2±0.5	380	20.27	210	1.85	20.8	1016	84
		Target	41.279,	7:00	460.1±9.7	21	18.38	250	1.51	17.9	1015	92
		(0)	2.010	9:30	462.8±6.1	427	20.54	230	2.00	22.3	1015	77
		Downwind	41.285,	7:00	447.0±15.6	38	18.53	240	0.81	20.1	1015	78
		(-2)	2.002	9:30	461.7±8.5	519	20.96	230	1.86	21.4	1016	66
10-27	Gavà	southern	41.268,	4:00	396.6±6.8	13	14.03	0.5	0.45	9.8	1012	64
		(2)	2.032	7:00	399.8±4.1	89	12.21	0	0.14	10.9	1014	64
				9:30	393.9±11.8	805	15.62	120	0.80	16.2	1014	50
				11:00	396.3±7.7	1291	18.44	120	1.55	21.6	1015	45
	Poble	southern	41.395,	4:00	402.8±NA	472	16.04	320	0.00	10.7	1013	60
		(4)	2.206	7:00	400.9±8.8	216	15.05	270	0.10	13	1015	52
				9:30	407.5±9.8	633	16.57	320	1.71	17.3	1016	42
				11:00	406.1±7.4	908	17.94	270	0.72	21.6	1015	43
	Tibidabo	southern	41.418,	4:00	406.3±3.7	180	10.02	0	5.11	7.9	960	63
		(442)	2.116	7:00	407.1±1.7	139	9.423	100	1.32	8.9	961	63

9:30	NA	172	11.03	20	1.19	11.3	963	57
11:00	413.3±0.3	343	13.21	255	1.26	18.7	963	38

Table S2. Summary of climatic conditions during the days of both campaigns. Psfc, T(ºC) and Accumulated Precipitation (mm) obtained from the Meteorological Service of Catalonia.

May 2020 Campaign

Dates (2020)	**Psfc (hPa)**	**T (ºC)**	**Precipitation accumulated (mm)**	**CWTs**	**Synoptic Wind component**
05-18	1019.2	19.75	0.0	CNE	NE
05-19	1015.73	21.43	0.0	C	N
05-20	1015.17	21.45	0.0	C	N
05-21	1018.27	23.63	0.0	U	N
05-25	1025.6	20.93	0.0	E	E
05-26	1024.97	22.23	0.0	E	E
05-27	1026.1	21.08	0.0	E	E
05-28	1023.7	20.5	0.0	A	SE
06-01	1015.5	20.56	2.6	U	SE
06-15	1019.03	20.98	0.0	U	NW

October 2020 Campaign

Dates (2020)	**Psfc (hPa)**	**T (ºC)**	**Precipitation accumulated (mm)**	**CWTs**	**Synoptic Wind component**
10-13	1012.7	16.3	0.0	C	NW
10-15	1013.0	13.5	0.0	CN	N
10-19	1021.2	16.1	0.0	ASW	SW
10-20	1017.1	18.5	0.0	SW	SW
10-21	1012.4	20.2	0.0	CSW	SW
10-22	1015.2	19.2	1.3	SW	SW
10-23	1017.7	18.9	0.3	U	W
10-27	1016.2	14.3	0.0	ANW	NW

Method description

Objective and automatic classifications are based on the application of algorithms that use ratios derived from atmospheric pressure fields and allow objective comparisons to be made. Jenkinson and Collison (JC) classification (Jenkinson and Collison, 1977), which was adapted from the Lamb catalogue and uses surface pressure data. This classification has been adapted to many regions and is one of the most commonly used (e.g. Jones et al., 1993; Trigo and DaCamara, 2000; Cortesi et al., 2014). JC classification has the advantage of being a universal and standardized method that allows comparison between different regions. JC method was included in the framework of COST7333 Action, which involved researchers from 23 countries working to find the most suitable automatic classifications in Europe (Huth et al., 2008). The JC classification is an objective scheme based on 9 daily grid-point mean sea-level pressure data. It is an extension of the Lamb classification from 10 to 27 circulation weather types (CWTs). The method was adapted to the Iberian Peninsula in accordance with the proposal by Spellman (2000) and moved 5º to the east (Gilabert and Llasat, 2017). The CWTs are calculated using the surface pressure of the NCEP/NCAR reanalysis dataset.

CWTs: Cyclonic (C), Anticyclonic (A), pure advectives (N, S, E, W, NE, SE, NW, SW), hybrid cyclone- advectives (CN, CNE, CE, CSE, CS, CSW, CW, CNW), hybrid anticyclone-advectives (AN, ANE, AE, ASE, AS, ASW, AW, ANW).

References:

Jenkinson AF, Collison FP. 1977. An initial climatology of gales over the North Sea. Technical Report, Synoptic climatology Branch Memorandum No. 62, Meteorological Office, Bracknell, UK, 18 pp.

Jones PD, HulmeM, Briffa KR. 1993.A comparison of Lamb circulation types with an objective classification scheme. Int. J. Climatol. 13(6): 655–663.

Trigo RM, DaCamara CC. 2000. Circulation weather types and their influence on the precipitation regime in Portugal. Int. J. Climatol. 20(13): 1559–1581.

Cortesi N, Gonzalez-Hidalgo JC, Trigo RM, Ramos AM. 2014.Weather types and spatial variability of precipitation in the Iberian Peninsula. Int. J. Climatol. 34(8): 2661–2677.

Huth R, Beck C, Philipp A, Demuzere M, Ustrnul Z, Cahynová M, Kyselý J, Tveito OE. 2008. Classifications of atmospheric circulation patterns. Ann. N. Y. Acad. Sci. 1146: 105–152.

Spellman G. 2000. The use of an index-based regression model for precipitation analysis on the Iberian Peninsula. Theor. Appl. Climatol. 66(3–4): 229–239.

Gilabert, J., Llasat, M. C. (2018). Circulation weather types associated with extreme flood events in Northwestern Mediterranean. *International Journal of Climatology*, *38*(4), 1864-1876.

Table S3. Model characteristics and experiment configurations.

Resolution and initial conditions	
Horizontal resolution	9 km x 9 km; 3 km x 3 km; 1 km x 1 km
Domain dimensions	150 x 145; 118 x 118; 121 x 121
Vertical layers	57 (16 between the surface and 100 m)
Top of the atmosphere	50 hPa
Initial conditions	ERA5 (C3S 2017) with 31 km horizontal resolution, 137 vertical levels and 6-hour separation
Physics parameterizations	
Microphysics	WRF Single-Moment 6-class scheme (Hong and Lim 2006)
Shortwave and longwave radiation	RRTMG scheme (Iacono et al. 2008)
Cumulus	Kain-Fritsch scheme (Kain and Kain 2004) (only the outermost domain)
PBL Scheme	Boulac (Bougeault and Lacarrere 1989)
Surface / UCP	Noah Land Surface Model (pervious areas) (Chen and Dudhia 2001) / BEP+BEM (impervious areas) (Salamanca and Martilli 2010)
Surface layer	Monin-Obukhov Eta similarity scheme with Zilitinkevich thermal roughness length

Hong, S.-Y., Kim, J.-H., Lim, J., & Dudhia, J. (2006). The WRF single moment microphysics scheme (WSM). Journal of the Korean Meteorological Society. 42. 129-151.

Iacono, M. J., Delamere, J. S., Mlawer, E. J., Shephard, M. W., Clough, S. A., & Collins, W. D. (2008). Radiative forcing by long-lived greenhouse gases: Calculations with the AER radiative transfer models. Journal of Geophysical Research Atmospheres, 113(13). https://doi.org/10.1029/2008JD009944

Bougeault, P., & Lacarrere, P. (1989). Parameterization of orography-induced turbulence in a mesobeta-scale model. Monthly Weather Review, 117(8), 1872–1890. https://doi.org/10.1175/1520-0493(1989)117<1872:POOITI>2.0.CO;2

Kain, J. S., & Kain, J. (2004). The Kain - Fritsch convective parameterization: An update. Journal of Applied Meteorology, 43(1), 170–181. https://doi.org/10.1175/1520-0450(2004)043<0170:TKCPAU>2.0.CO;2

Chen, F., & Dudhia, J. (2001). Coupling and advanced land surface-hydrology model with the Penn State-NCAR MM5 modeling system. Part I: Model implementation and sensitivity. Monthly Weather Review, 129(4), 569–585. https://doi.org/10.1175/1520-0493(2001)129<0569:CAALSH>2.0.CO;2

Salamanca, F., & Martilli, A. (2010). A new Building Energy Model coupled with an Urban Canopy Parameterization for urban climate simulations-part II. Validation with one dimension off-line simulations. Theoretical and Applied Climatology. https://doi.org/10.1007/s00704-009-0143-8

Table S4. Validation and statistical analyses of the root-mean-square error (RMSE), mean bias (MB) and correlation factor (R).

Campaign	Parameter	root-mean-square error (RMSE)	mean bias (MB)	r
May	RH	13.17%	-6.19%	0.74
May	T	1.74°C	0.44°C	0.91
May	WS	1.35ms-1	0.13ms-1	0.59
October	RH r	14.13%	7.72%	0.80
October	T	1.94°C	1.16°C	0.94
October	WS	1.65 ms-1	0.45 ms-1	0.52

$$RMSE = \left(\frac{1}{N}\sum_{i=1}^{N}(M_i - O_i)^2\right)^{1/2}$$

$$MB = \frac{1}{N}\sum_{i=1}^{N}(M_i - O_i)$$

$$R = \frac{\sum_{i=1}^{N}\left(M_i - \acute{M}\right)\left(O_i - \acute{O}\right)}{\left(\sum_{i=1}^{N}\left(M_i - \acute{M}\right)^2\right)^{1/2}\left(\sum_{i=1}^{N}\left(O_i - \acute{O}\right)^2\right)^{1/2}}$$

Where M_i represents the modelled value and O_i the observed value at each time step. The overbar represents the mean between all the available time steps (N) for all meteorological station.

Figure S1. Plot of the Zumkehr et al. (2018) gridded anthropogenic emissions inventory of OCS in Catalonia (left panel) and Barcelona metropolitan area (right panel). Below are the histograms with the emission values of the different sources for Barcelona and the rest of Europe according to Zumkehr et al. (2018).

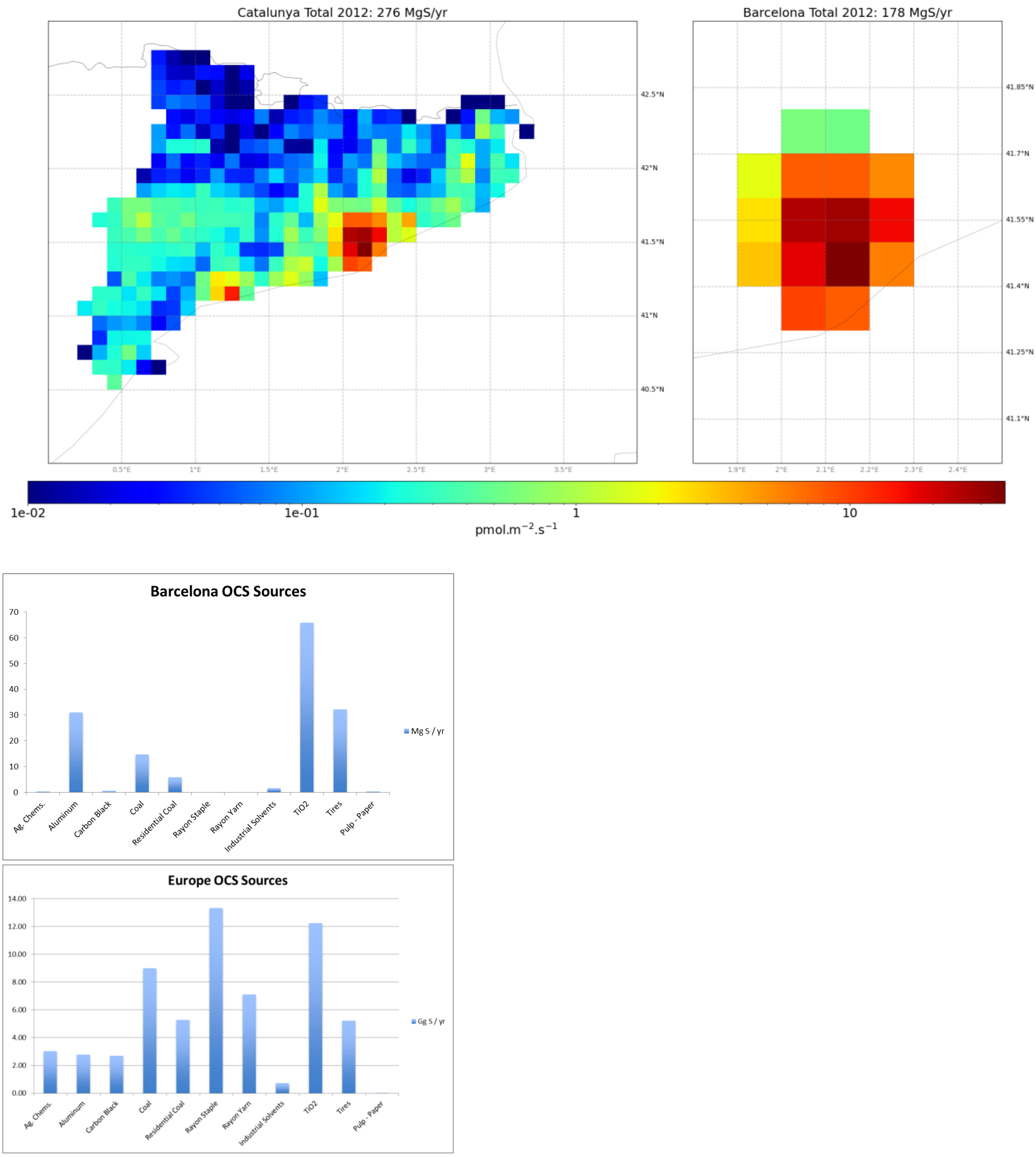

Figure S2. Domains of the WRF model for this study with 9, 3 and 1km grid size for d01, d02 and d03, respectively.

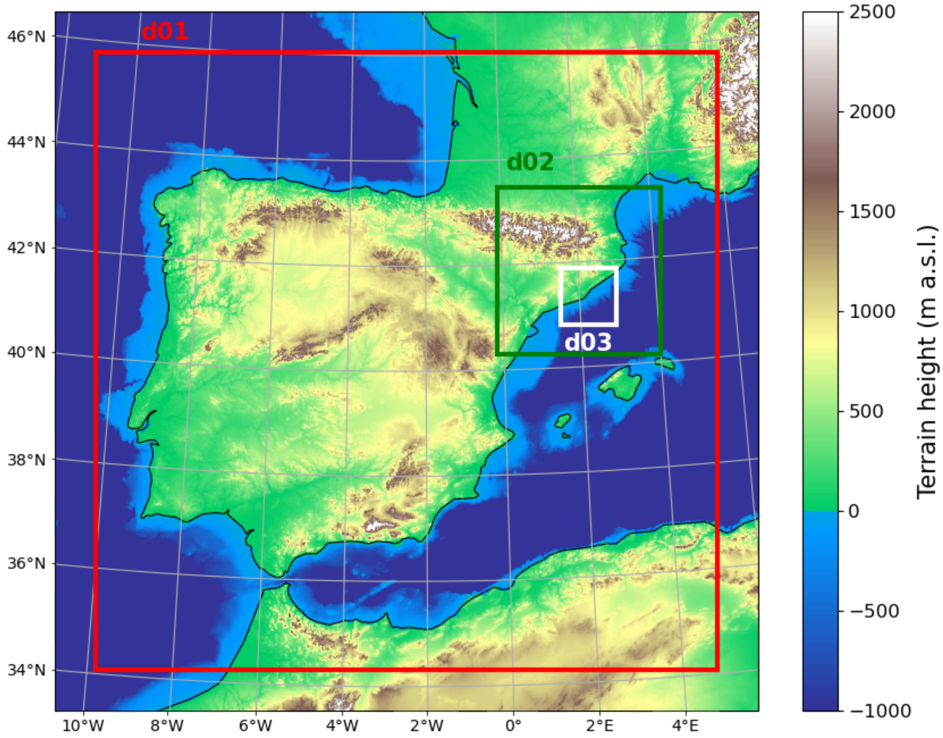

Figure S3 Relative humidity (RH), temperature (T) and wind speed (WD) analysis for the validation of WRF simulations. Root mean square error (RMSE), Mean bias and correlation are shown for each station during the campaign in May.

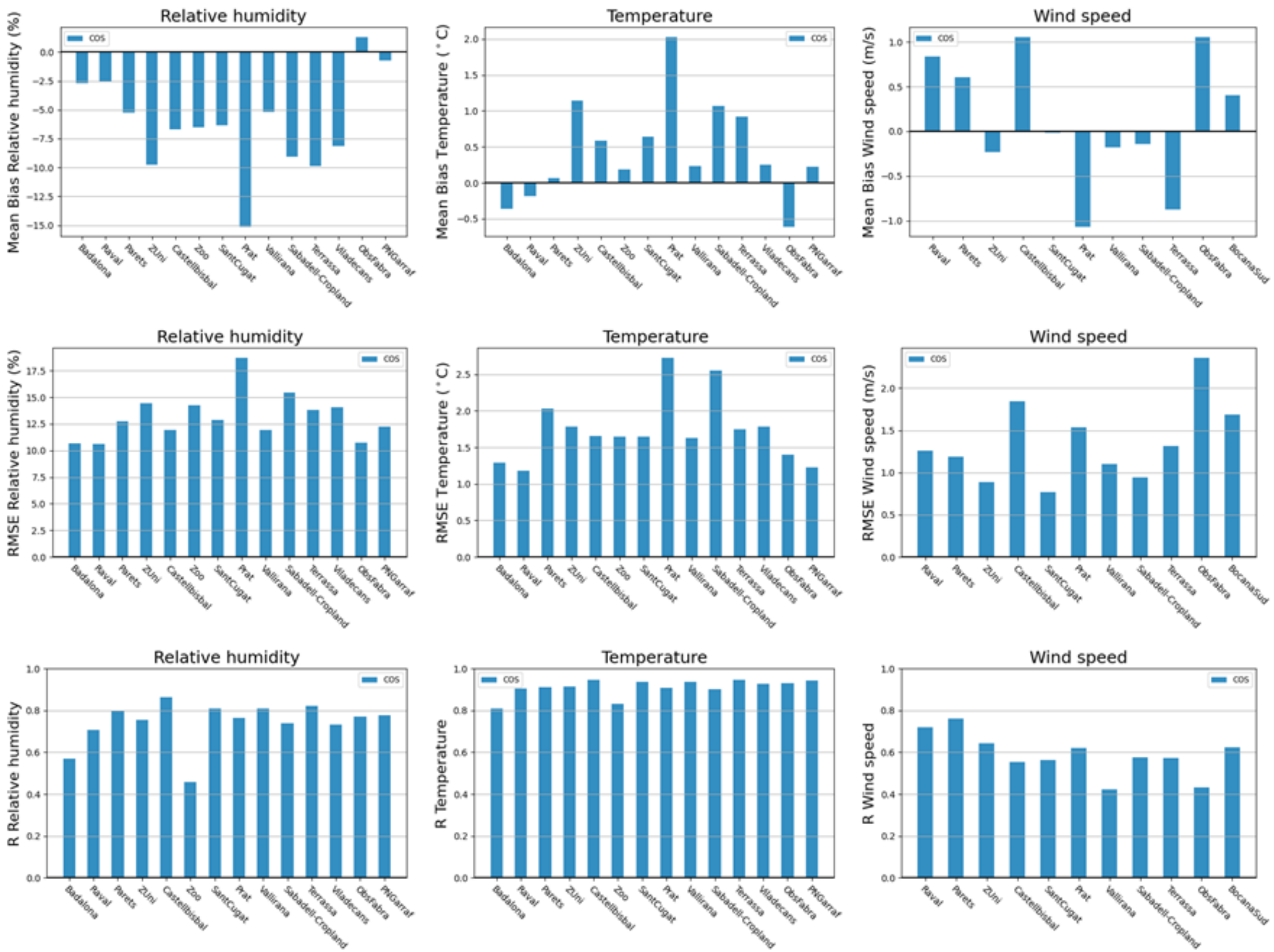

Figure S4 Relative humidity (RH), temperature (T) and wind speed (WD) analysis for the validation of WRF simulations. Root mean square error (RMSE), Mean bias and correlation are shown for each station during the campaign in October**.**

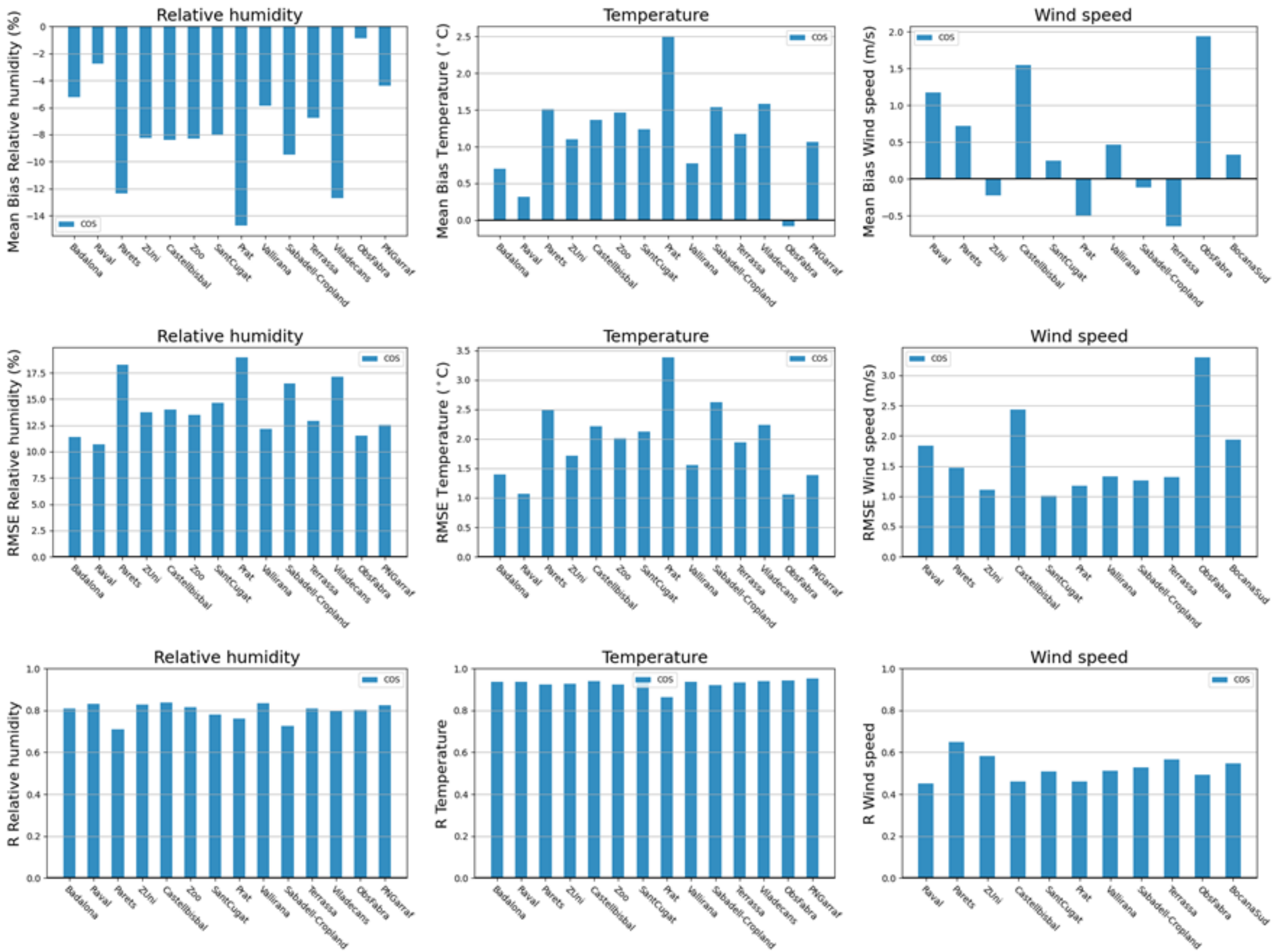

Figure S5 Upper panel: Hourly atmospheric radon concentrations (black dots) and PBLH estimations based on ceilometer (red dots) where dotted vertical lines represent 00:00 and solid lines 12:00 UTC; Bottom panel: Hourly ratio between radon concentration and PBLH estimates labeled per hour of the day.

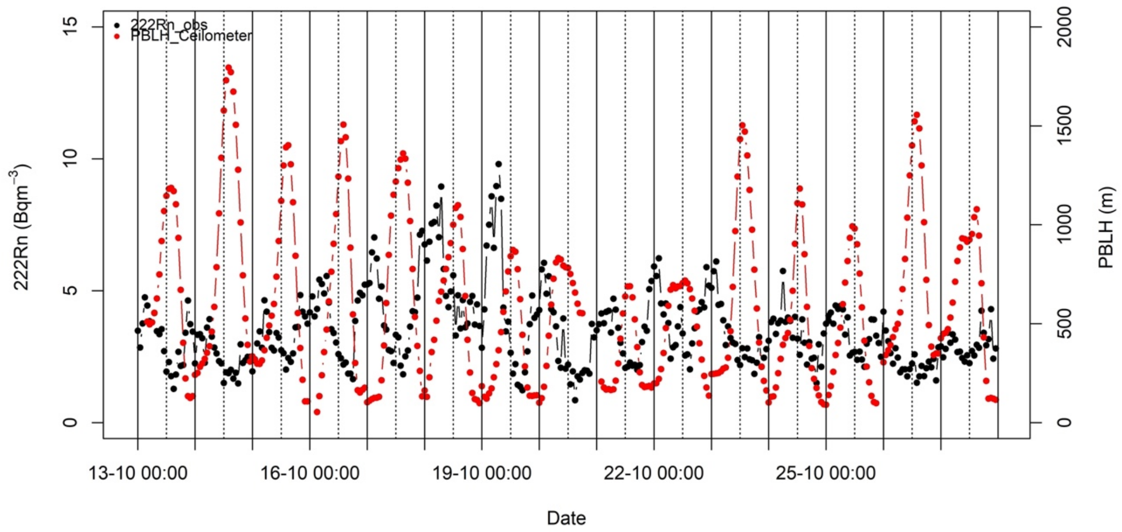

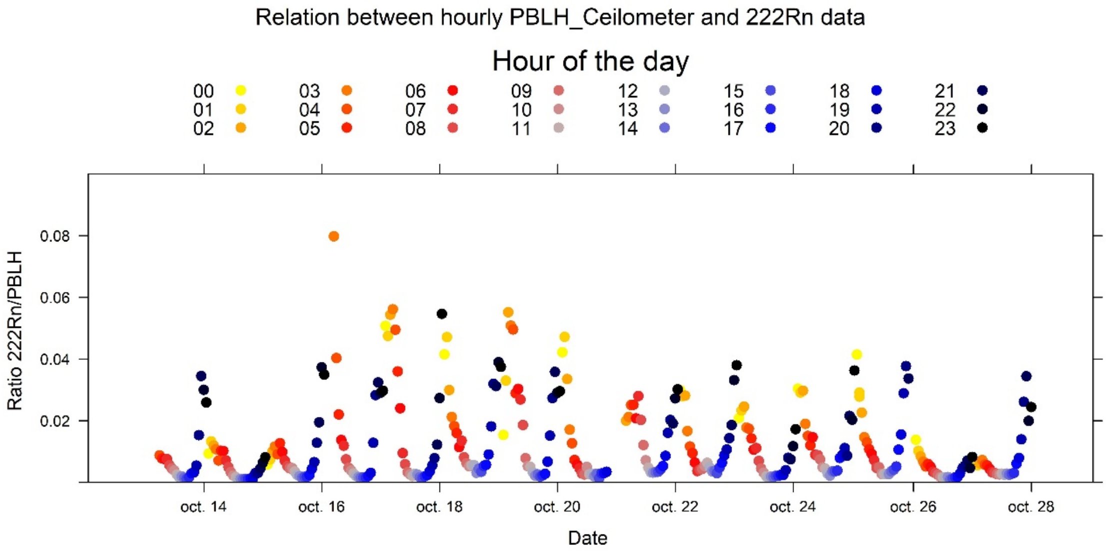

Figure S6. Pseudo gradient of radon (black line) and the wind speed (blue line) time series obtained at the same Target during October 2020. Lines indicating the values of the quartile 1, 2 and 3 used for the stability index analysis are also presented in red, violet and brown colors respectively.

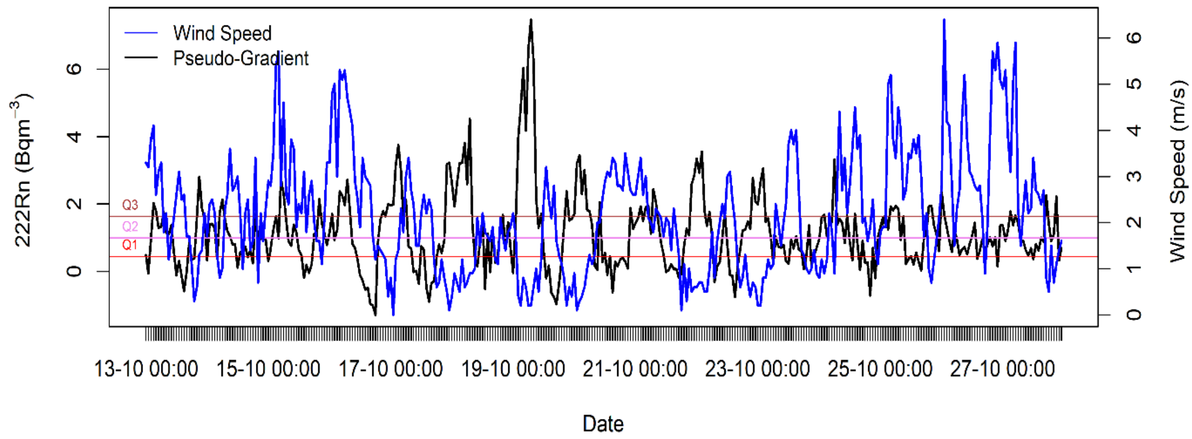

Figure S7. **Maps (a,b) with** mean (±σ) OCS Values from NOAA stations, GIF station, Utrecht station and our background value calculated from Tibidabo upwind site, in the northern hemisphere calculated using data from the periods in which the campaigns were done. Plots (c,d) show mean (±σ) from OCS values obtained during both campaigns in Barcelona area (BCN), and at the European Integrated Carbon Observation System (ICOS) station located in Gif-Sur-Yvette (Gif) and run by LSCE, and NOAA station Mace Head, Ireland (MHD) during the same period in a) May and b) October 2020.

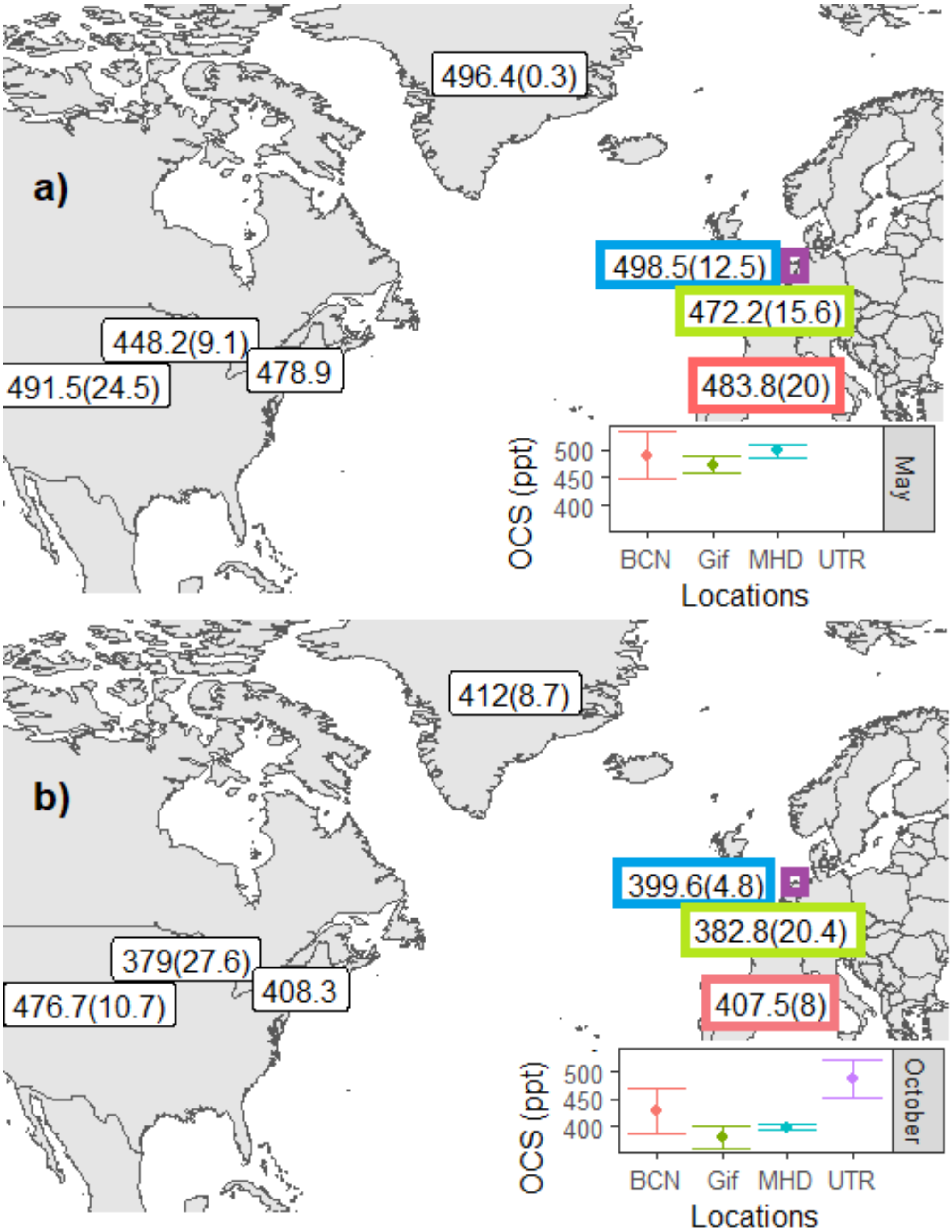

Figure S8. Maps showing the increase or decrease in OCS referred to background values (Delta OCS) for May at Forest: a) Collserola and b) Tibidabo. Delta OCS is in ppt. background values were 487 ppt. Black arrow shows the wind direction and speed measured on site, the absence of an arrow means that there was not wind blowing at the moment of measurement. Small map on the left is showing the residence time in logarithmic scale of the air masses arriving at the sampling site, determined with the FLEXPART model.

a) Collserola

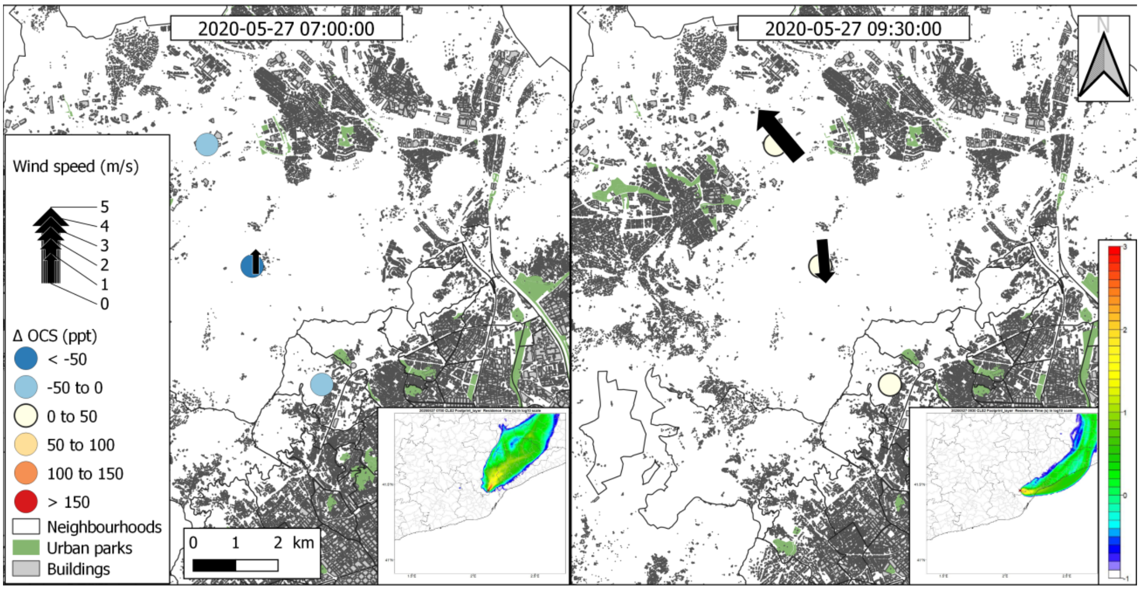

b) Tibidabo

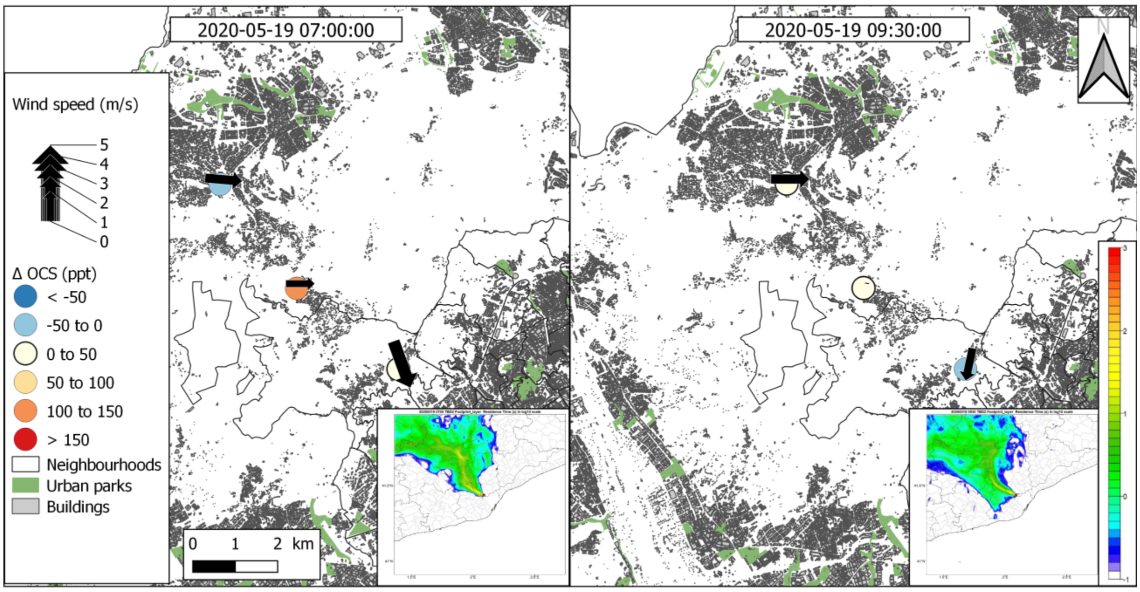
2020-05-19 07:00:00
2020-05-19 09:30:00
N
Wind speed (m/s)
5
4
3
2
1
0
Δ OCS (ppt)
< -50
-50 to 0
0 to 50
50 to 100
100 to 150
> 150
Neighbourhoods
Urban parks
Buildings
0 1 2 km

Appendix S1

Wind rose showing typical winds direction and speed for our sampling period in Barcelona Metropolitan area. Data from May and June 2019, data provided from Meteocat (https://www.meteo.cat/). Each panel shows time in UTC at the upper part. Colour palete represent the wind velocity in m s^{-1}.

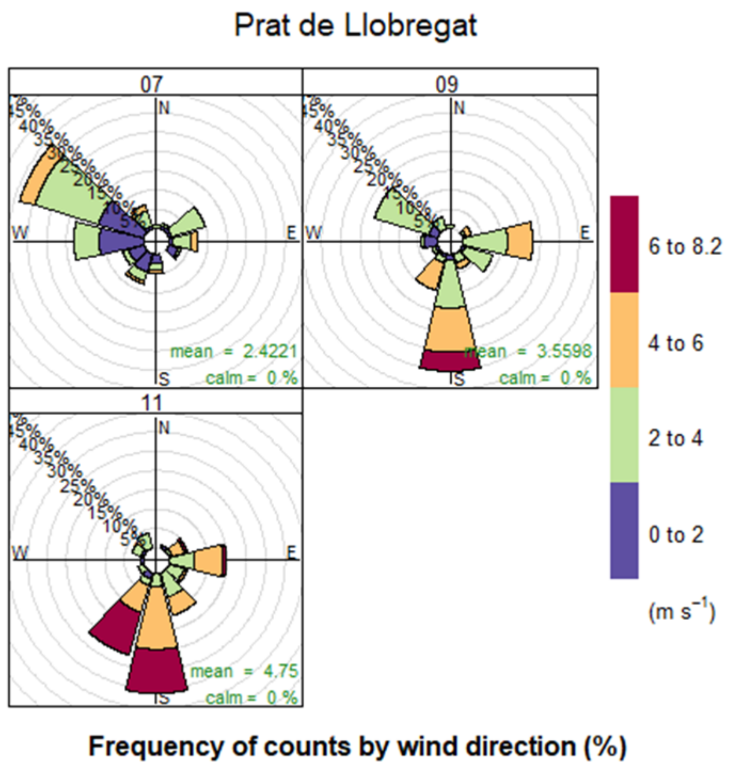

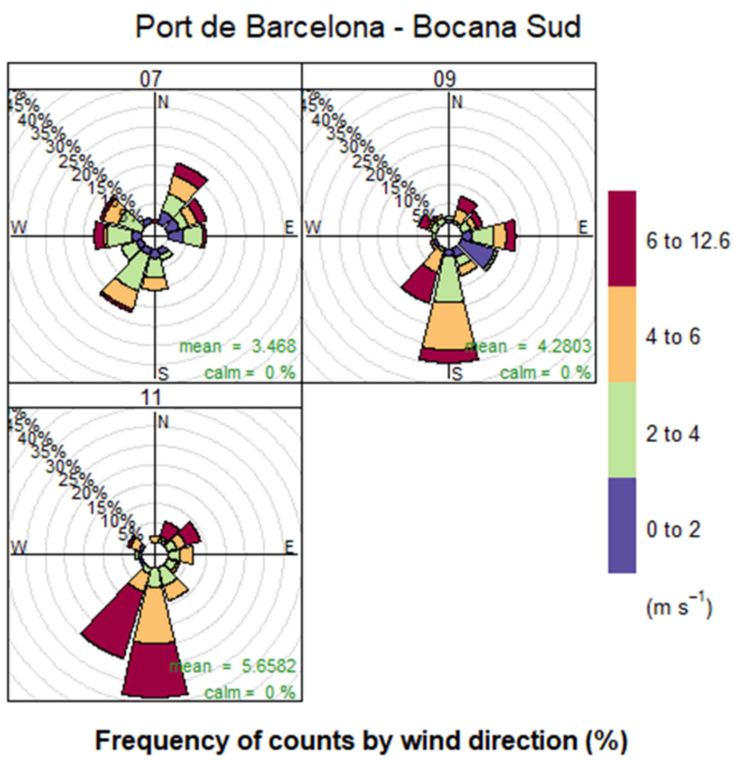

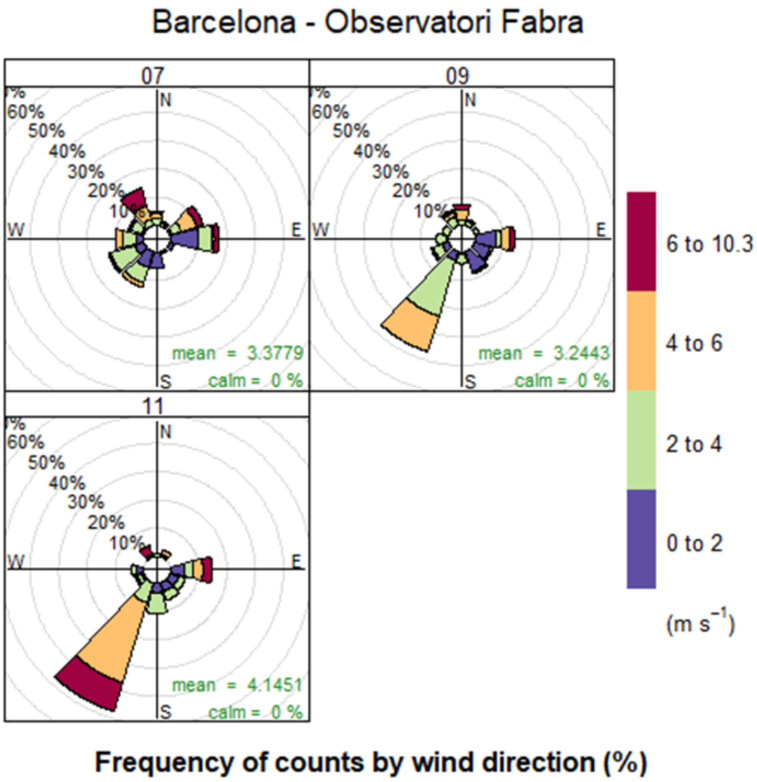

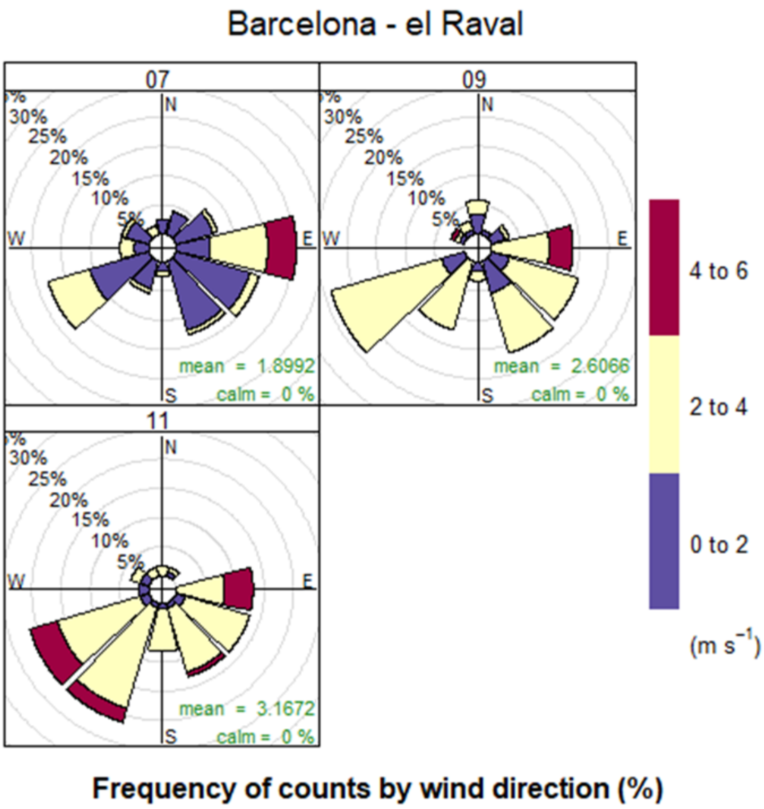

Meteocat stations locations: Prat de Llobregat is located near Prat and Gava Targets. Por the Barcelona is located near Montjuic, Observatori Fabra is located near Tibidabo background sampling Target nd elRaval is located in the vicinities of Sagrada and Poble Nou.

Appendix S2

Pictures and brief description showing the Targets measured during the campaigns:

- Agricultural (Gavà and Prat)



The two pictures on the left correspond to Gavà and two pictures on the right show Prat, both are similar agricultural Targets with Gava having one of the locations next to the sea and Prat was a couple km inland.

- forest (Tibidabo and Collserola)


Tibidabo and collserola have in common being forested areas and being topographically elevated.

- urban green (Montjuic and Guinardó)

Guinardo (Left) and Montjuic (Right) are both extensive urban parcs within the city of Barcelona, but wile guinardó is surrounded by intensive antropogenic conructions (buildings and roads, Montjuic is located next to the sea, however, Montjuic ints near the Port of Barcelona, were an intensive activity is performed.

- Urban (Sagrada Familia and Poble Nou).

Those locations are representatives of Barcelona streets; they are characterized by high intensive traffic and commercial activities. The only difference between both Targets is that, Poble Nou area is next to the sea and has marine influence while Sagrada is located at the heart of the city.

Appendix S3

The structure of the PBL, part of the troposphere that is directly influenced by the presence of the earth's surface, can be complicated and variable (Stull, 1988). The PBL height is commonly used to characterize the vertical extension of the mixed layer and the level at which exchange with the free atmosphere occurs (Seibert et al., 2000). PBL height estimation methods can differ among them by several hundred meters. For these reasons, some studies compare methods and their uncertainties (Seidel, 2000; Seibert et al., 2000) or develop numerical procedures (Liu and Liang, 2010) to determine PBLH from available soundings.

PBL height on the campaign days was extracted from daily observations (at 0000 UTC and 1200 UTC) from the Barcelona radiosonde station (on the roof of the Physics Faculty, close to Palau Reial), part of the Global Meteorological Network. The sounding data includes the observed temperature, dew point, humidity, wind speed, and wind direction at different pressure levels. To determine the PBLH, we followed a robust numerical procedure proposed by Liu and Liang. (2010). this procedure begins by identifying for each sounding observation in which of the three major regimes of the PBL structure we are (Stull, 1988): unstable, stable, or neutral regime. To do so, we calculate the potential temperature between 5th and 2nd levels (chosen to remove raw data noises):

$$\theta_s - \theta_2 = \begin{cases} < -\delta_s \; for\; CBL \rightarrow an\; unstable\; regime \\ > +\delta_s \; for\; SBL \rightarrow a\; stable\; regime \\ else\; for\; NRL \rightarrow a\; neutral\; regime \end{cases}$$

Where:

- θ = potential temperature (Kelvin) and its sub-index is the corresponding to the sounding data level (l=1 is on the surface)
- $\delta_s = \theta$ increment for the minimum strength of the stable (inversion) layer, above the CBL top or below the SBL top
  ($\delta_s = \theta$ for idealized cases but in practice is a small positive)

Unstable and neutral regime

Following the method from Liu and Liang (2010), for unstable and neutral regime, we scan upward twice: First, to find the lowest level l=k that meets the condition $\theta_k - \theta_a \geq \delta_u$; where δ_u is the θ increment for the minimum strength of the unstable layer. And then, a second scan to search the occurrence of

$$\dot{\theta}_k \equiv \frac{\partial \theta_k}{\partial z} \geq \dot{\theta}_r$$

Where:

- θ= vertical thermal gradient per height z
- θ_r= minimum strength for the overlying inversion layer and can be considered as the overshooting threshold of the rising parcel.

Stable regime

For the stable regime, the PBLH is more difficult to quantify and there is no unique algorithm to determine it accurately without actual observations of the turbulence kinetic energy profile in the boundary layer (Stull, 1988; Seibert et al., 2000). SBL turbulence can result from two dominant mechanisms: buoyancy forced and/or shear driven. When the SBL is buoyancy forced, Liu and Liang (2010) propose to scan upward to find the lowest level at which $\dot{\theta}_k$ reaches a minimum and then determine the PBLH at that level if either of the following conditions is met:

$$\begin{cases} \dot{\theta}_k - \dot{\theta}_{k-1} < -\dot{\delta} \\ \dot{\theta}_{k+1} < \dot{\theta}_r, \dot{\theta}_{k+2} < \dot{\theta}_r \end{cases}$$

Where:

- 1st condition ensures that $\theta_r$is a local peak with a curvature parameterθ_r of 40 K·km^{-1}
- 2nd condition constrains that an inversion layer is not evident in the upper two layers.

PBLH is defined at either the top of the bulk stable layer or at the level of the low-level jet (LLJ) nose if present, whichever is lower.

References:

Liu, S. and Liang X., 2010. Observed diurnal Cycle Climatology of Planetary Boundary Layer Height. Journal of Climate, 23, 5790-5809.

Seibert, P. et al., 2000. Review and intercomparison of operational methods for the determination of the mixing height. Atmos. Environ., 34, 1001-1027

Seidel, D. J., C.O. Ao, and K. Li, 2010. Estimating climatological planetary boundary layer heights from radiosonde observations: Comparison of methods and uncertainty analysis, J. Geophys. Res., 115, D16113, doi: 10.1029/2009JD013680.

Stull, R.B., 1988. An Introduction to Boundary Layer Meteorology. Kluwer Academic, 666 pp.

Appendix S4 Maps showing the results from FLEXPART models.

MEASUREMENTS AT 7 AND 9:30:

Campaign	Date	7 UTC	930 UTC
May	2020-05-18 Gavà	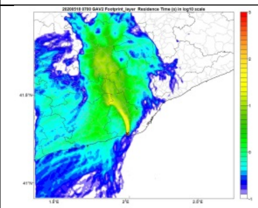	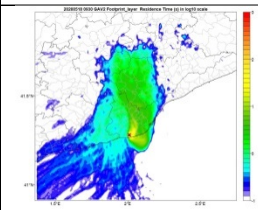
	2020-05-19 Tibidabo	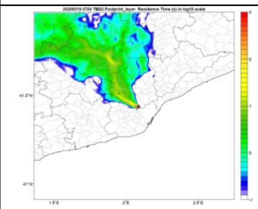	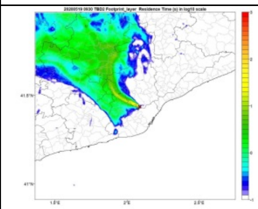
	2020-05-20 Montjuic	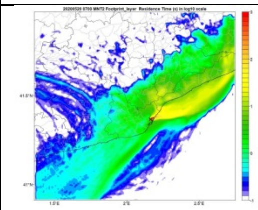	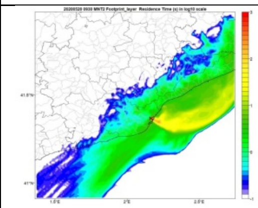
	2020-05-21 Poble Nou	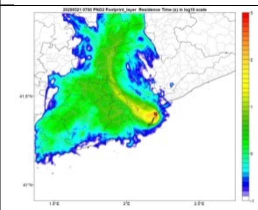	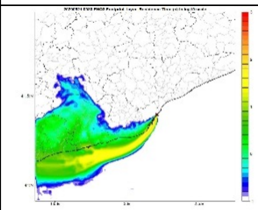
	2020-05-25 Prat	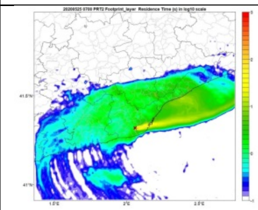	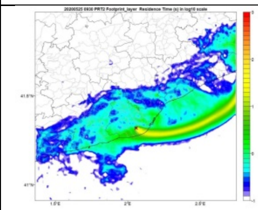
	2020-05-26 Sagrada Familia	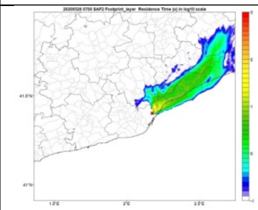	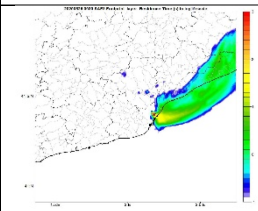
	2020-05-27 Collserola	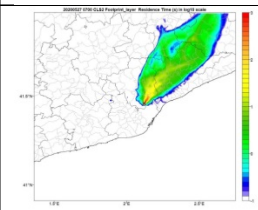	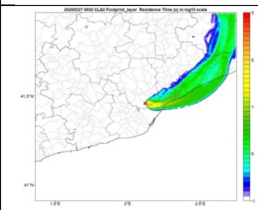
	2020-05-28 Guinardó	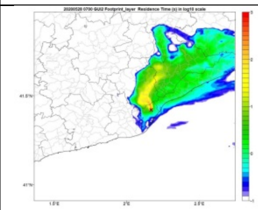	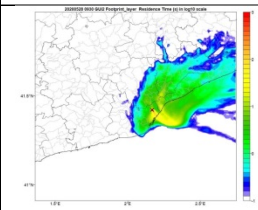

October	2020-10-15 Poble Nou	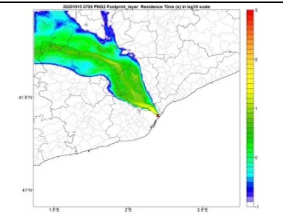	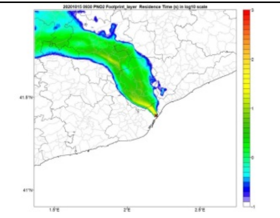
	2020-10-19 Guinardó	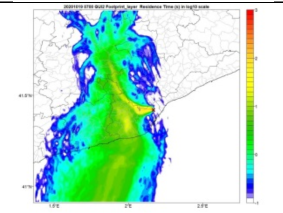	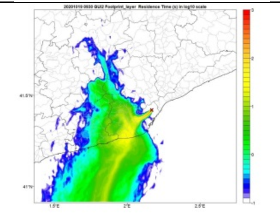
	2020-10-20 Sagrada	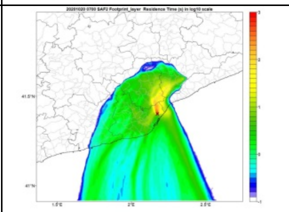	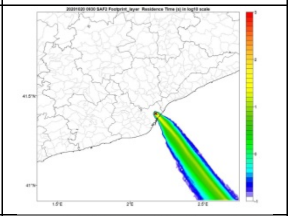
	2020-10-21 Montjuic	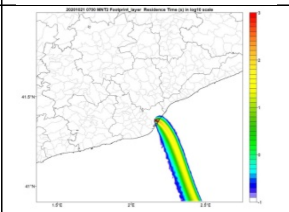	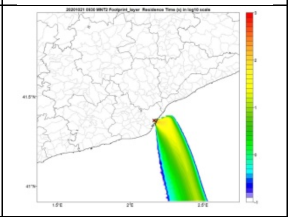
	2020-10-22 Prat	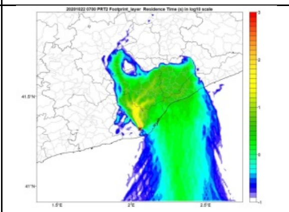	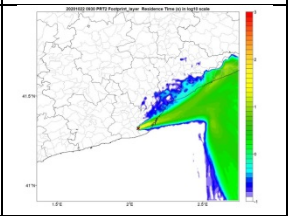
	2020-10-23 Gavà	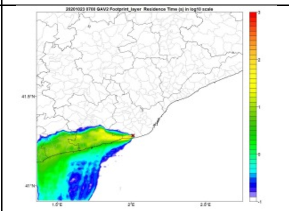	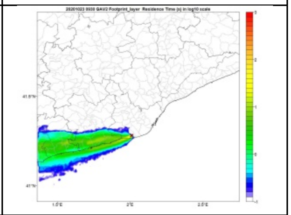

MEASURES AT 4 AND 11:

	Date hour	Gavà	Tibidabo	Poble Nou
May	**2020-05-18** 4:00 UTC	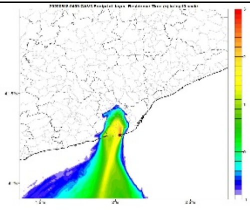	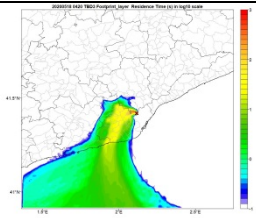	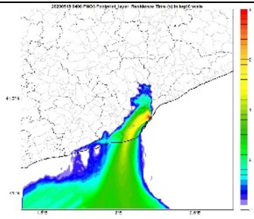
	11:00 UTC	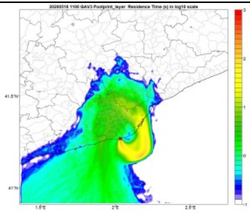	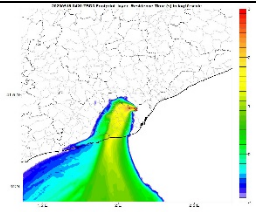	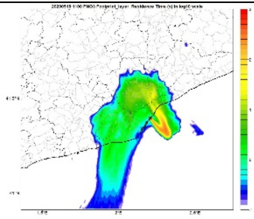
	2020-05-21 4:00 UTC	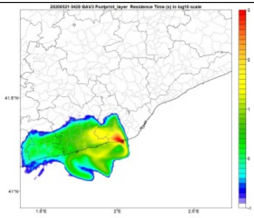	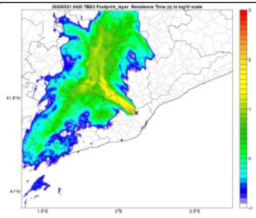	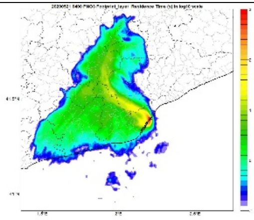
	11:00 UTC	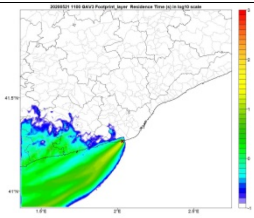	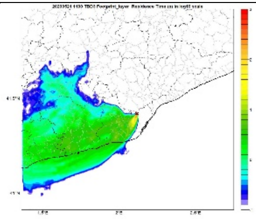	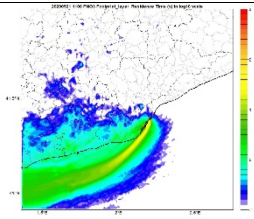
	2020-05-25 4:00 UTC	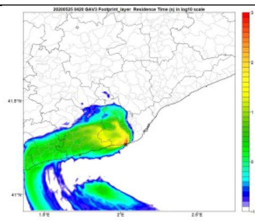	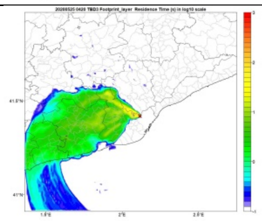	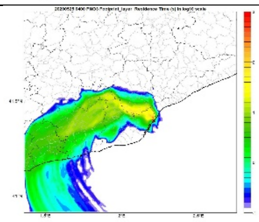
	11:00 UTC	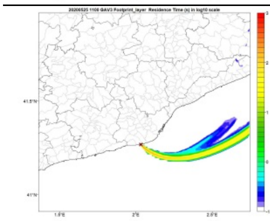	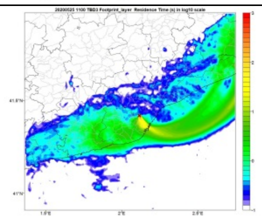	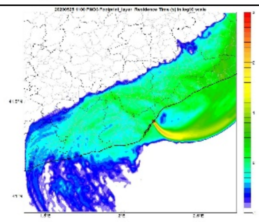
Oct.	**2020-10-13** 4:00 UTC	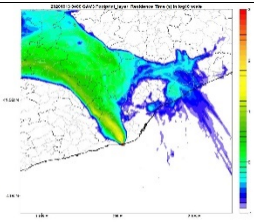	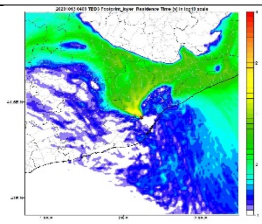	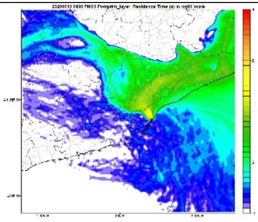
	07:00 UTC	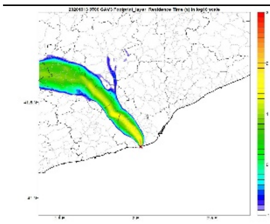	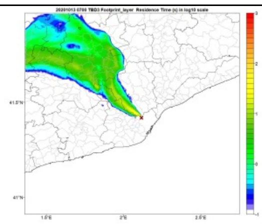	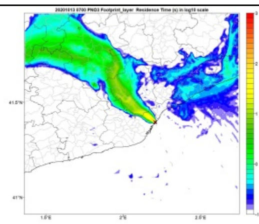

	09:30 UTC	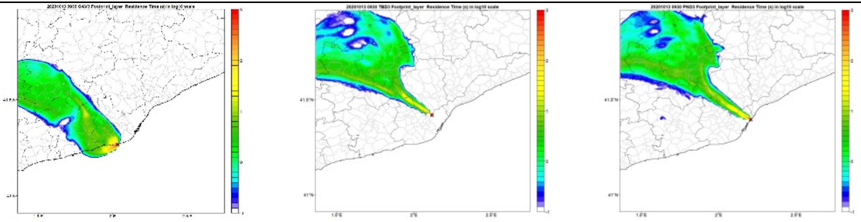
	11:00 UTC	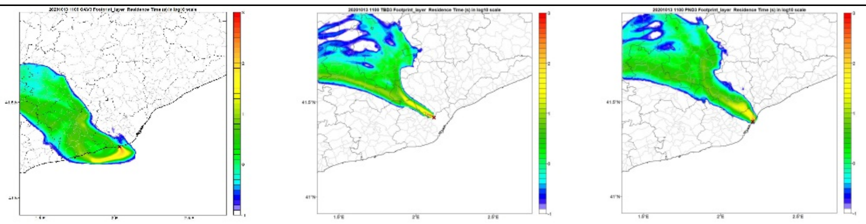
	2020-10-27 4:00 UTC	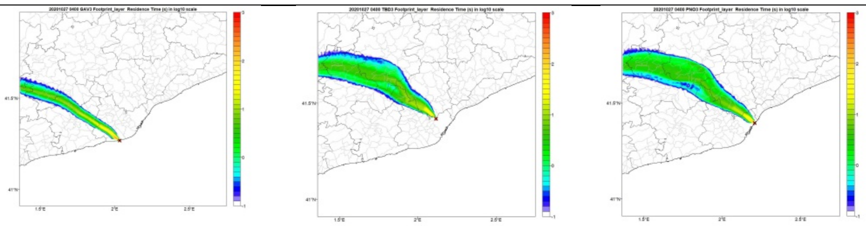
	07:00 UTC	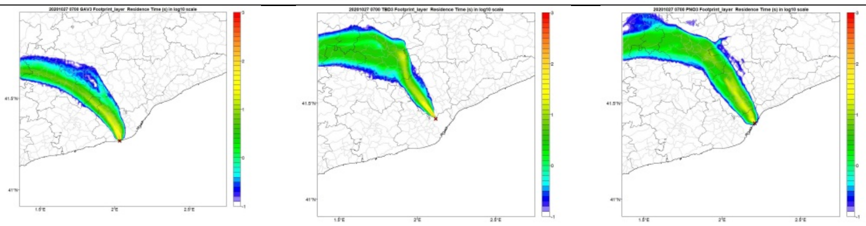
	09:30 UTC	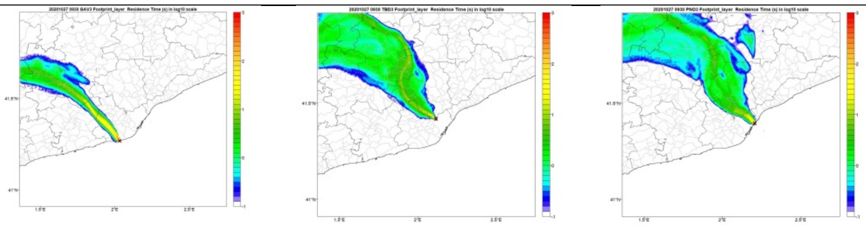
	11:00 UTC